Faculteit Wetenschappen

Departement Fysica

Alternative scan strategies for high resolution STEM imaging

Alternatieve scan strategieën voor hoge resolutie raster elektronen microscopie

Proefschrift voorgelegd tot het behalen van de graad van
Doctor in de Wetenschappen, Fysica
aan de Universiteit Antwerpen, te verdedigen door

Abner Velazco Torrejón

Promotor:
Prof. Dr. Johan Verbeeck

Antwerpen, 2021

Chairman
Prof. Dr. Jan Sijbers, University of Antwerp, Belgium

Supervisor
Prof. Dr. Johan Verbeeck, University of Antwerp, Belgium

Members
Prof. Dr. Joris Dirckx, University of Antwerp, Belgium
Dr. Colin Ophus, Lawrence Berkeley National Laboratory, United States
Dr. Wouter Van den Broek, Thermo Fisher Scientific, The Netherlands

Contact information
Abner Velazco Torrejón
University of Antwerp
Faculty of Science
Department of Physics
Groenenborgerlaan 171
2020 Antwerp
Belgium
Abner.VelazcoTorrejon@uantwerpen.be

Contents

Preface 1

Samenvatting 3

List of abbreviations 5

1 Transmission electron microscopy 7
- 1.1 Description of the instrument . . . 7
- 1.2 Scanning transmission electron microscopy . . . 14
  - 1.2.1 Conventional raster acquisition . . . 15
  - 1.2.2 STEM imaging . . . 18

2 Distortions in STEM images 21
- 2.1 Sources of distortions in STEM images . . . 21
  - 2.1.1 Sample drift distortions . . . 22
  - 2.1.2 Scanning distortions . . . 22
  - 2.1.3 Imaging acquisition system distortions . . . 24
- 2.2 Conventional methods to address scanning distortions, post-processing techniques . . . 27
- 2.3 Approach to non-conventional methods to address scanning distortions . . . 28

3 Electron beam damage 31
- 3.1 Knock-on damage . . . 31
- 3.2 Radiolysis . . . 32
- 3.3 Beam damage as a diffusion process . . . 34
  - 3.3.1 Possible time dependent damage mechanisms . . . 34
- 3.4 Methods to address beam damage-radiolysis . . . 37
  - 3.4.1 Conventional low dose techniques in STEM imaging . . . 38
  - 3.4.2 Non-conventional low dose techniques in STEM imaging-compressed sensing . . . 41
  - 3.4.3 Dose fractionation technique in STEM imaging . . . 42

4 Scan strategy to address drift and scanning distortions in STEM **45**
4.1 Hardware to control the scan engine of the microscope 45
4.2 Continuous scan strategies without flyback compensation for STEM 46
4.2.1 Snake scanning 46
4.2.2 Hilbert scanning 46
4.3 Experimental evaluation on a single crystal test sample 47
4.3.1 Scanning distortions correction 50
4.3.2 High frequency content evaluation 53
4.3.3 Lattice parameter evaluation 55
4.4 Discussion 59
4.5 Conclusions 60

5 Scan strategy to address electron beam damage in STEM **61**
5.1 Interleaving pattern 62
5.2 Experimental findings on electron beam sensitive samples 64
5.3 Comparison and quantification of beam damage 82
5.4 Discussion 96
5.5 Conclusions 97

6 Diffusion model for the observed beam damage behaviour **99**
6.1 Definition of the model 99
6.2 Estimation of a diffusion constant 103
6.3 Simulation model to reproduce experimental findings 107
6.4 Estimation of parameters to further outperform beam damage 109
6.5 Conclusions 111

7 Future perspectives and general conclusions **113**
7.1 Application of the current techniques in different beam sensitive materials . . 113
7.2 Further experiments to determine the diffusion mechanism(s) 114
7.2.1 Working at lower beam currents 114
7.2.2 Applying the method to samples with known electrostatic charging effects 115

List of scientific contributions **117**

Bibliography **119**

Acknowledgements **131**

Preface

Currently, a large variety of materials are studied by transmission electron microscopy (TEM) as it offers the possibility to perform structural and elemental analysis at a local scale. Relatively recent advances in aberration correctors and electron sources allow the instrument to achieve atomic resolution. Along with these advances, a state-of-the-art technology has been reached in TEM. However, the instrument is far from being perfect and imperfections or external sources can make the interpretation of information troublesome. Environmental factors such as acoustic and mechanical vibrations, temperature fluctuations, etc., can induce sample drift and create image distortions. These distortions are enhanced in scanning operation because of the serial acquisition of the information, which are more apparent at atomic resolution as small field of views are imaged. In addition, scanning distortions are induced due to the finite time response of the scan coils. These types of distortions would reduce precision in atomic-scale strain analysis, for instance, in semiconductors. Most of the efforts to correct these distortions are focused on data processing techniques post-acquisition. Another limitation in TEM is beam damage effects. Beam damage arises because of the energy transferred to the sample in electron-sample interactions. In scanning TEM, at atomic resolution, the increased electron charge density (electron dose) carried on a sub-Å size electron probe may aggravate beam damage effects. Soft materials such as zeolites, organic, biological materials, etc., can be destroyed under irradiation limiting the amount of information that can be acquired. Current efforts to circumvent beam damage are mostly based on low electron dose acquisitions and data processing methods to maximize the signal at low dose conditions.

In this thesis, a different approach is given to address drift and scanning distortions, as well as beam damage effects. Novel scan strategies are proposed for that purpose, which are shown to substantially overcome these issues compared to the standard scan method in TEM. In the following the content of this thesis is summarized:

- The first chapter gives an overview of modern TEMs and describes the principal components that allow for atomic resolution. The chapter is focused on the scanning operation mode of these instruments.
- The second chapter describes imperfections of the instruments and external sources that induce image artefacts during the serial acquisition in scanning mode.

- The third chapter discusses the main mechanisms of electron beam damage and gives a diffusion process approach to describe some of these mechanisms. The first results of this work are given in this chapter.
- New scan methodologies are proposed in the fourth chapter with the aim to overcome image artefacts described in chapter 2. These methodologies are compared with the current standard acquisition mode in terms of image distortions.
- An alternative scan method to reduce diffusion-like damage processes is presented in the fifth chapter. Experimental results showing a benefit on damage reduction compared to the standard acquisition mode are given in this chapter.
- The sixth chapter describes a diffusion model that is able to reproduce the experimental results.
- The last chapter proposes further steps to explore additional applicability's of the scan methods described here.

Samenvatting

Tegenwoordig worden vele materialen onderzocht met transmissie elektronenmicroscopie (TEM) vanwege het voordeel dat het zowel structurele als chemische analyse toelaat op lokale schaal. Relatief recente ontwikkelingen in aberratie correctoren en elektronenbronnen laten toe om vlot atomaire resolutie te bereiken. Dit maakt TEM tot een speerpunttechnologie in het onderzoek van materialen. Nochtans is dit instrument verre van perfect aangezien zowel interne als externe stoorbronnen de interpretatie van de verkregen informatie sterk kunnen bemoeilijken. Omgevingsfactoren zoals akoestische en mechanische trillingen, temperatuur fluctuaties kunnen drift veroorzaken in de sample positie wat leidt tot distorsies in de beeldvorming. Deze distorsies zijn meer uitgesproken in gescande opstellingen waar de informatie sequentieel wordt opgenomen in het bijzonder als het gaat om heel hoge vergrotingen waarbij atomaire resolutie wordt beoogd. Bovendien ontstaan er door de eindige tijdsrespons van de scan spoelen nog bijkomende distorsies in het beeld. Deze distorsies beperken de precisie waarmee bijvoorbeeld de rek kan gemeten worden in halfgeleidermaterialen aan de hand van atomaire resolutie beelden. De meeste inspanningen om deze distorsie tegen te gaan richting zich op post-acquisitie data bewerking. Een andere belangrijke beperking in het gebruik van TEM is het optreden van bundelschade. Bundelschade treedt op wanneer energie uit de elektronenbundel overgedragen wordt naar het preparaat door middel van inelastische interactie. In scanning TEM hebben we typisch te maken met een hoge elektronenflux en dosis die interageert met het preparaat door middel van een bundel met sub-Å afmetingen wat het probleem van lokale bundelschade flink kan verergeren. Zogenaamde 'zachte materialen' zoals bv. zeolieten, organische en biologische materialen kunnen beschadigd worden tijdens deze irradiatie wat de hoeveelheid en betrouwbaarheid van de gegevens sterk kan beïnvloeden. Huidige pogingen om dit effect onder controle te houden spitsen zich vooral toe op het verminderen van de benodigde elektronendosis met behoud van een acceptabele signaal ruis verhouding.

In deze thesis zal ik nieuwe methoden aanreiken en evalueren om zowel het effect van scan distorsies als bundelschade in scanning TEM tegen te gaan of te verminderen. Nieuwe scan strategieën worden voorgesteld en er zal worden aangetoond dat deze beide belangrijke obstakels in moderne TEM beeldvorming significant kunnen verminderen. In wat volgt vat ik kort de verschillende hoofdstukken samen die aan bod komen in deze thesis.

- Het eerste hoofdstuk geeft een overzicht van een moderne TEM en beschrijft de basiscomponenten die nodig zijn om atomaire resolutie te kunnen bereiken. Dit hoofdstuk richt zich vooral op scanning TEM methoden aangezien die verder in de thesis gebruikt en verbeterd zullen worden.
- Het tweede hoofdstuk beschrijft de imperfecties in de huidige instrumenten alsook de externe stoorbronnen die beeldvervorming veroorzaken tijdens sequentiële beeldvormingsmethoden.
- Het derde hoofdstuk bespreekt de belangrijkste mechanismen van elektronen bundelschade en stelt een beschrijving voor op basis van een diffusievergelijking. Dit hoofdstuk bevat de eerste concrete resultaten die werden behaald.
- Nieuwe scan strategieën worden voorgesteld in het 4de hoofdstuk met als doel de beeldvervorming die in hoofdstuk 2 besproken werd te verminderen. Deze nieuwe methode wordt vergeleken met de bestaande scan methoden.
- In het vijfde hoofdstuk stel ik een alternatieve scan methode voor die als doel heeft om het diffusieproces dat aanleiding geeft tot bundelschade te verminderen. Experimenten tonen aan dat er inderdaad een belangrijke reductie in bundelschade mogelijk is in vergelijking met de standaard scan methode bij gelijke dosis en belichtingstijd.
- Het zesde hoofdstuk beschrijft het diffusiemodel dat in staat is om kwalitatief de bundelschade experimenten te beschrijven.
- Het laatste hoofdstuk vat de resultaten samen en bespreekt het toekomstperspectief voor de methoden die in deze thesis werden geïntroduceerd.

List of abbreviations

2D	two-dimensional
4D	four-dimensional
AC	alternating current
ADC	analog to digital converter
ADF	annular dark field
BF	bright field
CCD	charge coupled device
CS	compressed sensing
CTEM	conventional tranmission electron microscopy
DAC	digital to analog converter
DF	dark field
EDX	energy dispersive X-ray
EELS	electron energy-loss spectroscopy
EM	electron microscopy
FEG	field emission gun
FPGA	field programmable gate array
FT	Fourier transform
FWHM	full width at half maximum
GPA	geometric phase analysis
HAADF	high angle annular dark field
HR	high resolution
HRSTEM	high resolution scanning tranmission electron microscopy
iDPC	integrated differential phase contrast
IUPAC	International Union of Pure and Applied Chemistry
LVEBL	low-voltage electron beam lithography
NCC	normalized cross-correlation
PC	personal computer
PMT	photomultiplier tube
RMS	root mean square
SEM	scanning electron microscopy
SNR	signal to noise ratio
SPM	scanning probe microscopy
STEM	scanning transmission electron microscopy
TEM	transmission electron microscope(y)
YAP	yttrium aluminum perovskite

Chapter 1

Transmission electron microscopy

1.1 Description of the instrument

The transmission electron microscope (TEM) has been developed to outperform the diffraction limit encountered in light-optical microscopy. The wave behaviour of moving particles such as electrons, and the current level achieved in the development of magnetic lenses and aberration correctors allow for atomic resolution; or commonly known as high resolution (HR) in electron microscopy (EM)[1].

The notions of spatial resolution limited by diffraction were given by Ernst Abbe back in 1874 [1], and due to the wave behaviour of the electrons, this notions also apply to EM. The resolution is conceptually limited by the wavelength of the illumination source and the lens aperture limiting the entrance angle of the incoming waves.

The de Broglie wavelength of the electrons rely on their kinetic energy, and it is given by the equation

$$\lambda = \frac{h}{m_0 v} \tag{1.1}$$

where h is Plancks's constant, and m_0 and v represent the rest mass and the speed of the electrons, respectively. Standard acceleration voltages in modern TEMs are between 60 - 300 kV. A relativistic effect needs to be taken into account for accelerating voltages $>\sim$100 kV as the speed of the electrons approaches the speed of light [2]. At these values, the associated de Broglie wavelength is in the order of a few pm with a theoretical resolution in the same order of magnitude. However, in EM field, Abbe's notion only sets a theoretical limit while aberrations and even environmental fluctuations place a practical limiting factor.

The high energy acquired by the electrons is also needed so that the electrons can travel through a thin sample, while only a small fraction of this energy is actually transferred to the sample. Although analytical information can be extracted from the signal(s) generated

[1]Although the term high resolution in conventional tranmission electron microscopy (CTEM) alone imply the use of phase contrast, commonly the term is used with a broader meaning referring to the smallest spatial feature that can be resolve in images obtained with this method as well as with scanning tranmission electron microscopy (STEM), even if the process of image formation are fundamentally different.

from the absorbed energy, this small amount of energy can be sufficient to deteriorate the specimen (as we will see later in this thesis).

In analogy to the refraction of light, an electron beam can be deflected by the Coulomb or Lorentz forces when applying an electric or a magnetic field. Fundamentally, einzel lenses [3] and wire coils are employed as electrostatic and magnetic lenses, respectively. With a focusing effect for electrons passing through these devices, similar to a light beam focused by a convex glass lens. In a simplified manner and considering a paraxial approximation, the radial component of the fields inside and their cylindrical symmetry with respect to the axis of the lenses, helps to interpret their focusing characteristic in a similar way geometric optics do for glass lenses[2]. The analogy to geometric optics is usually sufficient to understand the path of the electron beam inside the column of the microscope. In modern TEMs the majority of the lenses encountered inside the column are magnetic lenses. These lenses consist of coils with ferromagnetic polepieces to obtain localized fields in a few mm. Because of their cylindrical symmetry these lenses are call round magnetic lenses.

Even though magnetic lenses are carefully designed and made with high precision, strong aberrations are always present. In an optical system with aberrations, the image of a point object is enlarged with respect to its diffraction limit, resulting in blurred images. As we mentioned before, magnetic lenses are analogue to optical lenses, and their aberrations can also be described by considering non-paraxial approximations of thick lenses [4].

Magnetic lenses with non-cylindrical symmetry suffer from astigmatism. The focusing power differs for rays of electrons arriving at different planes of incidence (the plane formed between the ray of electrons and the optical axis).

However, the most critical aberration that prevents to achieve HR in tranmission electron microscopy is spherical aberration. In a magnetic lens, the strength of the radial component of the magnetic field increases with the distance from its axis. For this reason, non-paraxial rays of electrons suffer a stronger focusing than paraxial rays do, which means a positive spherical aberration [5, 6]. For a point object, a disc of radius r_{sph} is obtained in the image plane. With $r_{sph} = c_s\alpha^3$, where c_s is the spherical aberration coefficient with units of distance (typically between 0.5 - 1.5 mm [6] in modern microscopes) and α is the semi-angle of illumination of the lens which is usually limited by an aperture. Working at low semi-angles reduces the effect from spherical aberrations at the expense of increasing the contribution from the diffraction limit. Non-abberation corrected microscopes, in scanning mode, typically work with optimal values of about 10 mrad to achieve $\sim$1.6 Å resolution [7]. In this operation mode, α is frequently used to represent the semi-convergent[3]

[2]In an electromagnetic lens, due to the Lorentz force, the electrons entering the field in a non-axial direction follow a rather more complicated trajectory with a rotational Larmor effect.

[3]Usually in the electron microscopy literature the words semi-convergent and convergent angle are used interchangeably to describe the maximum angle at which a ray of electrons deviate from the optical axis. Here we will always use semi-convergent angle.

angle of the probe-forming system. Low c_s coefficients can be obtained when increasing the magnetic field of magnetic lenses (with values up to 2 T in objective lenses) [3], which minimizes spherical aberrations. However, the focal length is also reduced. Aberration-corrected TEMs reduce the need of stronger fields in objective lenses that would shorten the focal length up to a point that would limit the tilt range angle of a sample/holder or even would prevent energy dispersive X-ray (EDX) detectors been placed close to the sample. Modern TEMs use an objective lens divided in two polepieces, upper and lower polepiece that benefit from a "large" gap of about 5 mm on Thermo Fisher Scientific (formerly FEI) TITAN[3] microscopes, see Figure 1.1.

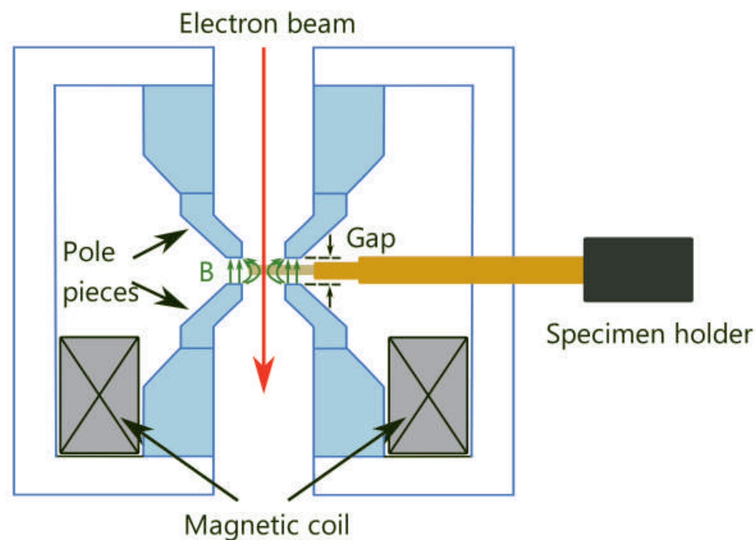

FIGURE 1.1: Twin objective lens (with a split pole piece) and specimen holder (side-entry holder). The pole pieces enclose the magnetic field B around the gap region.

Magnetic multipole lenses are employed to correct aberrations. Magnetic multipoles consist of pairs of magnetic coils, with opposite magnetic polarities, placed symmetrically with respect to the optical axis of the microscope (direction at which the electrons travel through the microscope column). Unlike the focusing lenses described earlier, whose axis corresponds to the axis of the microscope, multipoles are placed perpendicularly. The simplest multipole lenses are quadrupoles and are used to correct astigmatism. The Lorentz forces of a quadrupole are shown in Figure 1.2. The difference in focus because of astigmatism can be reduced by applying appropriate fields that change the strength of the orthogonal forces depicted in Figure 1.2. A pair of quadrupoles, one above the other, oriented 45° with respect to each other is employed in order to apply the orthogonal forces in different directions.

More sophisticated and hence expensive multipole lenses are required to correct spherical aberrations. A pair of hexapoles and a set of transfer lenses in between can be used for

this task. The purpose of the hexapoles is to increase the divergence of the non-paraxial rays of electrons. The result is a negative spherical aberration that compensates the strong focus of these rays. The first hexapole also induces a threefold astigmatism that is compensated by the second hexapole. The transfer lenses, which consist of round magnetic lenses, create an inversion so the two hexapoles can be placed identical to eliminate the threefold astigmatism. For an aberration-corrected TEM in scanning mode, a probe size of less than 0.8 Å (full width at half maximum, FWHM) is routinely achieved for HR after the correction of this aberration for semi-convergent angles around 20 mrad. While a spatial resolution bettern than 0.5 Å have been reported [8, 9]. Another corrector based on an octupole/quadrupole system can be employed to correct this aberration as well [10, 11].

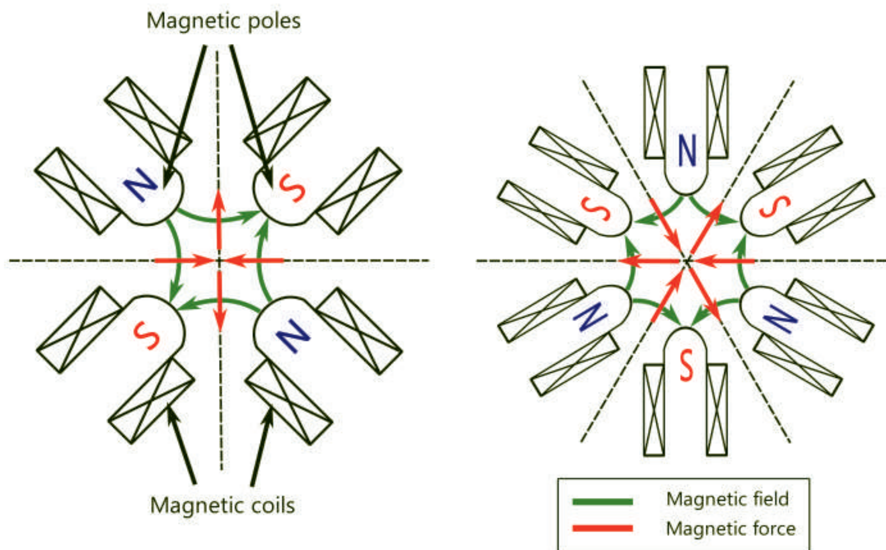

FIGURE 1.2: Magnetic multipole lenses. Quadrupole (left) and hexapole (right), not at the same scale.

Chromatic aberration is also present in magnetic lenses. Rays of electrons that follow the same path, however, travelling with different energies will be focused at different positions. The focusing power depends on the inverse value of the kinetic energy of the accelerated electrons [3]. In this case a point object will also be imaged as a disc with a size that depends on the angle of illumination α and the relation between the spread of the energy and the energy at which the electrons are accelerated. Current aberration-corrected TEMs are fitted with an electron gun with low energy spread, less than 1 eV, as we will see next. Furthermore, values of 0.1 eV can be achieved by the use of monochromators [5], with an improvement to 10 meV on Nion monochromators [12]. Electron beams in modern TEMs can be considered monochromatic as the relation between the energy spread and the energy of the accelerated electrons is very low, acceleration voltages of 120, 200 and 300 kV are the

most common. With the energy resolution provided by the monochromators, HR scanning tranmission electron microscopy (HRSTEM) in combination with electron energy-loss spectroscopy (EELS) have allowed unprecedented materials characterization at the atomic scale [13].

The role of the electron gun is to perform as a point source to emit a bright beam of electrons with constant kinetic energy; these requirements allow for high spatial coherency and low energy spread. Tungsten filaments and lanthanum hexaboride (LaB_6) crystals working based on the thermionic effect were used in TEMs decades ago. The requirements are outperformed by the use of electron guns working on the principle of field emission, usually tungsten needles are employed. In a field emission gun (FEG) or cold FEG, with the help of a suppressor, electrons are emitted mainly from the tip of the gun which is under a strong electric field applied through an extraction anode, Figure 1.3. The electrons seem to be emitted from the inside of the tip, creating a virtual source in the order of tens of nm. The gun can be heated to assist for the electron emission; this variation is called the schottky FEG. The brightness of these sources is between 100 - 1000 times the brightness of thermionic guns. With the brightness given by the current density per unit of solid angle,

$$\beta = \frac{4i_e}{(\pi d_0 \alpha_0)^2} \tag{1.2}$$

With d_0 the diameter, i_e the emission current and α_0 the divergence semi-angle that can be defined at the first gun cross-over[4] as in Figure 1.3. This is particularly important for HR as with more electrons available to irradiate the sample, more information can be extracted; however, beam sensitive materials also suffer more damage. On the other hand, bright sources permit to acquire images with short exposure times and hence to reduce the effects of mechanical instabilities like drift of the sample/stage for instance. Schottky guns have great emission current stability which is needed to obtain reliable quantitative information in HRSTEM or HRSTEM-EELS.

A TEM has similar components than a typical optical microscope. In a vertical column, from top to bottom, we can outline the elementary parts as follows: an illumination system, a condenser system, a sample stage, an imaging system and the detectors. With all these components precisely aligned along the optical axis. Here we mainly focus in the description of aberration-corrected microscopes for imaging mode. In Figure 1.4 a simplified diagram of a double corrected[5] TEM is shown.

In the illumination system we can find the electron gun with an acceleration anode, an electrostatic gun lens and an acceleration tube. Aberration-corrected microscopes equipped

[4]The brightness can be defined at any image plane as this quantity is conserved, when aberrations are excluded. For example if an aperture is present, the current density and the solid angle are reduced by the same proportion and the ratio between these values is kept constant.

[5]Double corrected refers to two aberration correctors, one for the probe forming system and one for the imaging system.

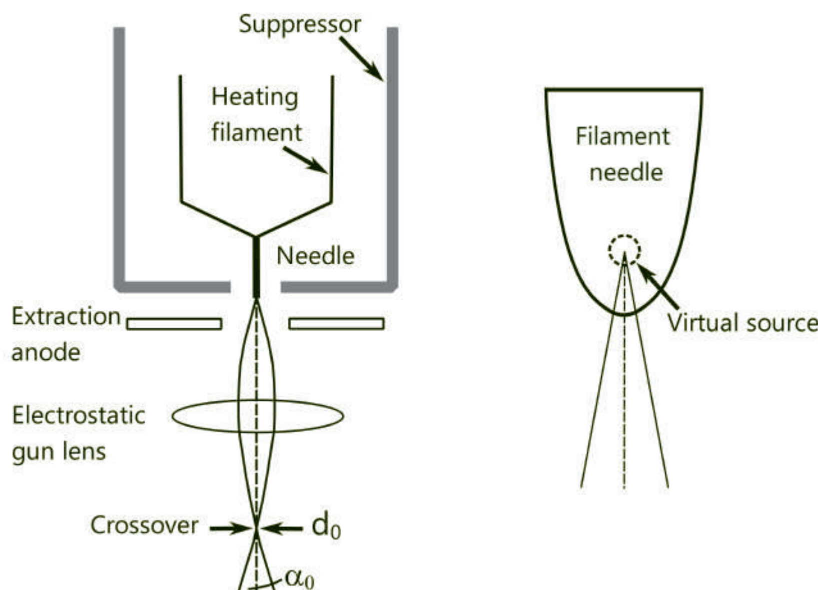

FIGURE 1.3: Schottky field emission gun (FEG) and an enlargment of the needle showing the virtual source.

with a monochromator, placed above the acceleration tube, permit continuous adjustment of the gun lens and hence control on the current that will be delivered to the sample (beam current); without changing the optical setup of the column, re-aligning the microscope or re-adjusting the corrector. This is extremely useful when working with beam sensitive materials, the beam current can be adjusted during experiments in a convenient way according to the sensitivity of the sample.

The condenser system comprises a group of condenser lenses that focus the electrons toward the sample and allows working with a parallel beam for conventional TEM (CTEM) or with a fine probe for STEM. Commonly, aberration-corrected microscopes are equipped with three condenser lenses, two condensers in non-corrected microscopes. These lenses are called C1, C2 and C3, positioned in the column from top to bottom. Three lenses give more flexibility to work with different setups; in scanning mode it is possible to work with a wider range of convergent angles, for instance. A cross-over in front of C2 is created by C1 lens. A parallel beam can be created if C2 is exited to form one more cross-over in the front-focal plane of the upper objective lens (C3 can be switched off so the system works as a two condenser system). For STEM, C2 lens can be slightly exited and C3 projects the rays onto the upper objective lens that converge the rays in its back-focal plane to create a probe. An aperture of around 50 μm below C2 limits the semi-convergent angle of the probe.

The most common sample stage is a side-entry type. The stage is fitted with a goniometer. A rod-shaped holder is inserted horizontally into the stage, see Figure 1.1, with the

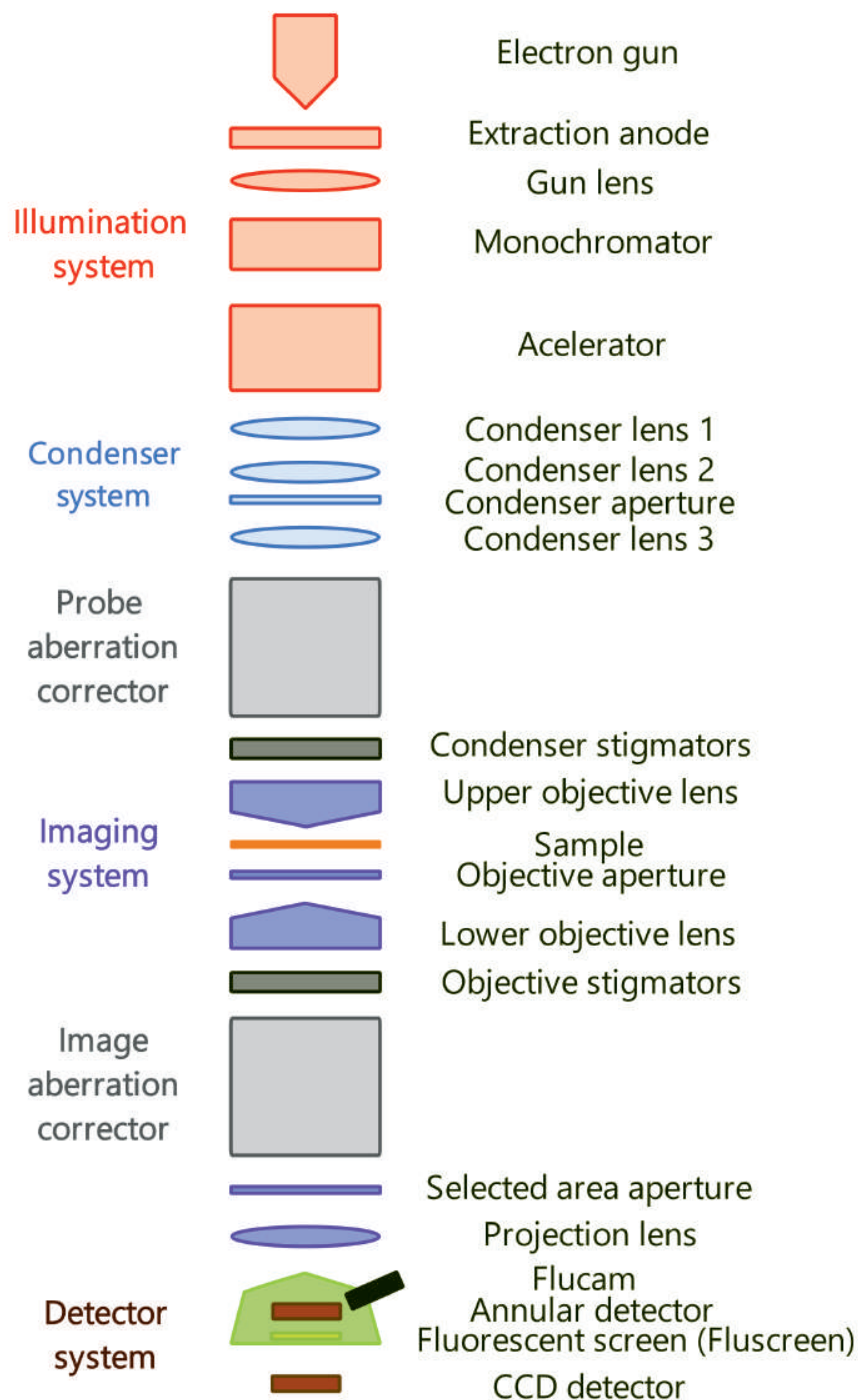

FIGURE 1.4: Diagram of a double aberration-corrected transmission electron microscope (TEM). The diagram shows the principal components of the microscope

sample clamped close to the end of the holder. Although this mechanism provides flexibility to control the position of the sample (translation and tilting), it exposes the sample trough the holder to mechanical or acoustical vibrations, either from the column or the surrounding environment. Thermal expansion in the holder, mainly in the axis of the rod, originates drift of the sample. These instabilities always translate to the acquired images as we will see in the next chapter. Waiting for stabilization and making fast acquisitions images help to reduce their effects.

The imaging system is based on the objective lens and a set of lenses called projection lenses, usually four lenses are employed. A diffraction pattern or an image can be displayed by the projection lenses when the back focal plane or the image plane of the objective lens is imaged by these lenses, respectively. The projection lenses are used to change either the image magnification or the camera length depending on the operation mode, real space imaging or diffraction.

The images or diffraction patterns generated in CTEM can be displayed on a fluorescent screen (flu-screen) or can be digitized by a CCD detector, usually positioned below the screen. In STEM, the signal scattered from each probe position is acquired by an annular detector based on a scintillator coupled to a photomultiplier tube. More details about these detectors will be given later in this document.

The present work was carried out on Thermo Fisher Scientific TITAN^3 microscopes. These are Schottky FEG, aberration-corrected microscopes which are enclosed to isolate the column from external disturbances and are remotely controlled and operated from a different room, see Figure 1.5.

1.2 Scanning transmission electron microscopy

In STEM an electron probe, formed by a convergent beam, is scanned across the sample. For each probe position the intensity of the signal coming from the scattered and/or transmitted electrons are acquired at the diffraction plane of the microscope. The scanning and the acquisition process are synchronized in order to display the intensities in a 2D array of pixels. In this operation mode, the spatial resolution is primarily given by the size of the probe and the aberrations of the objective lens. As it was noted before, sub-Angstrom probe sizes can be routinely achieved after correction of spherical aberrations. For HR imaging, the most employed technique is high angle annular dark field (HAADF) because of the direct interpretation of the contrast in terms of atomic composition and structure. The images are formed by electrons scattered elastically from the nucleus of the atoms, and can be explained by Rutherford scattering [4]. At high scattering angles, the signal is approximately proportional to Z^2, with Z the atomic number. This imaging method is different from CTEM imaging, where in the case the images are formed by the interference between diffracted electron waves is called phase contrast imaging or HRTEM. Annular detectors

FIGURE 1.5: Left, EMAT double corrected Thermo Fisher Scientific TITAN[3] microscope. Upper right, access to the side-entry stage. Bottom right, control room.

with collection angles in the range of 75 - 150 mrad can be used to acquire the HAADF signal. Other ADF signals can be measured with smaller collection angles; however, contributions from coherent scattering as in CTEM start to be present. The transmitted beam can also be acquired by a circular shape detector in analogy to the bright field (BF) signal in CTEM. These signals can be collected simultaneously by the use of independent detectors. In addition, the inelastic scattering signals that provide analytical information, like EDX or EELS, can also be collected simultaneously with HAADF acquisitions which make this the preferred method for HR.

1.2.1 Conventional raster acquisition

The electron probe movement is controlled by a set of deflectors or scan coils located right above the upper objective lens. Two sets of deflectors are employed to control the movement of the probe in the x and y direction of an X-Y plane. Each set of deflectors consist of a double deflection system, two pairs of coils mounted one above the other, designed to create a shift without tilting the beam (or viceversa). For each scan position, the probe is shifted from the optical axis. The ADF/BF detectors are aligned with respect to this axis and located in a conjugated plane of the back focal plane of the objective lens. In this plane the transmitted beam can also be aligned with respect to the optical axis for an effective measurement. A simplified sketch of this setup is given in Figure 1.6.

The conventional scanning path adopted for STEM imaging is raster scanning, in a similar way that was adopted in scanning electron microscopy (SEM) or indeed scanning probe microscopy (SPM) techniques. Here the electron probe is deflected from left to right in horizontal lines (fast scan direction), and then shifting the probe position vertically for the next line (slow scan direction); while the probe positions during scanning are regularly spaced by the pixel size. The magnification is controlled by changing the pixel size. When the probe reaches the end of one line it is deflected back to the beginning of the next line, see Figure 1.6, in the so-called 'flyback' motion. During this flyback, the finite time response of the scan coil system can lead to a deviation between the actual and the targeted position of the probe. This results in a deformation of the first few pixels of a new scan line until a constant probe velocity is reached. This effect is typically alleviated by adding a time delay (flyback time) at the beginning of each line. Typical flyback delays may vary from 100 - 2000 μs depending on the details of the microscope and it could be necessary to adjust this according to the acquisition conditions such as magnification and dwell time. Conventional dwell times in STEM imaging are between one and a few tens of μs. Besides increasing the total acquisition time, this solution has the drawback of injecting electrons into the flyback position which are not used for imaging. Such increased irradiation is unequally distributed and can lead to issues with electron beam sensitive samples degrading in ways that are difficult to predict.

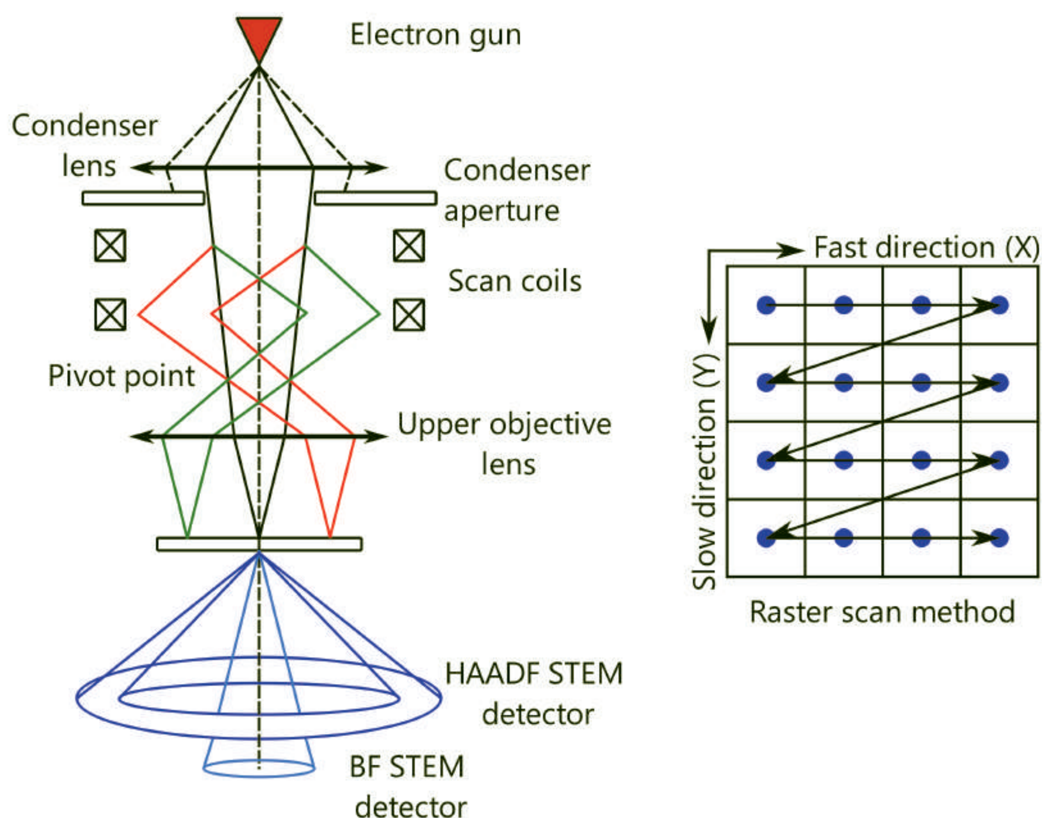

FIGURE 1.6: Simplified representation of the scanning operation mode in TEM (STEM), left. Two sets of scan coils are used to shift the probe without tilting. The pivot point happens at the front focal plane of the upper objective lens. The scattered and transmitted electrons corresponding to any position of the probe are stationary and formed at the back focal plane of the lower objective lens (not shown here for simplicity). Bright field (BF) and high angle annular dark field (HAADF) detectors are illustrated (scattered electrons can be collected at lower collection angles as well). Conventional raster scan method in STEM, right.

1.2.2 STEM imaging

Here we will describe the acquisition and digitization of the ADF signal in STEM. In particular, the HAADF signal is acquired at the collection angle range listed above. The azimuthal distributed ADF signal is detected by an annular scintillator to convert electrons to photons. Modern detectors employ an yttrium aluminum perovskite (YAP) crystal with a short light emission decay of ∼30 ns [14]. The photons are guided to a photomultiplier tube (PMT) by using a quartz light pipe. The time response of the PMT is on the order of a few ns [15]. A preamplifier converts the generated photocurrent to voltage. The signal is digitized by an analog to digital converter (ADC), and the conversion is repeated during the length of the selected dwell time. The intensities are integrated, averaged and assigned to each pixel corresponding to the position of the probe [16], and finally displayed in quasi real-time. The intensities are given in arbitrary counts. The Thermo Fisher Scientific TITAN[3] microscopes are equipped with a 16 bit converter; hence each pixel can be assigned with a value from 0 - 65536 of a gray scale. The brightness and contrast that is tuned to work within the dynamic range of the detection system is controlled by an offset voltage of the preamplifier and by the high voltage applied to the PMT, respectively [16, 17].

Despite the time decay of the scintillator being about two orders of magnitude shorter than the standard dwell time, and the fast response of the PMT, detailed characterizations of the detector system have shown a longer decay for single electrons events. Decay values between 1.7 - 3 μs have been reported [16, 17] and explained in terms of a long afterglow effect [18] and a slow response time of the preamplifier and read-out electronics [19]. The effect is severe for acquisitions with very short dwell time where smeared features along the scan line direction are identified [19, 20]. For longer dwell times, this effect is reduced as a result of the averaging signal process.

Figure 1.7 shows representative HAADF STEM images acquired at standard conditions for HR, 50 pA of beam current, 10 μs dwell time.

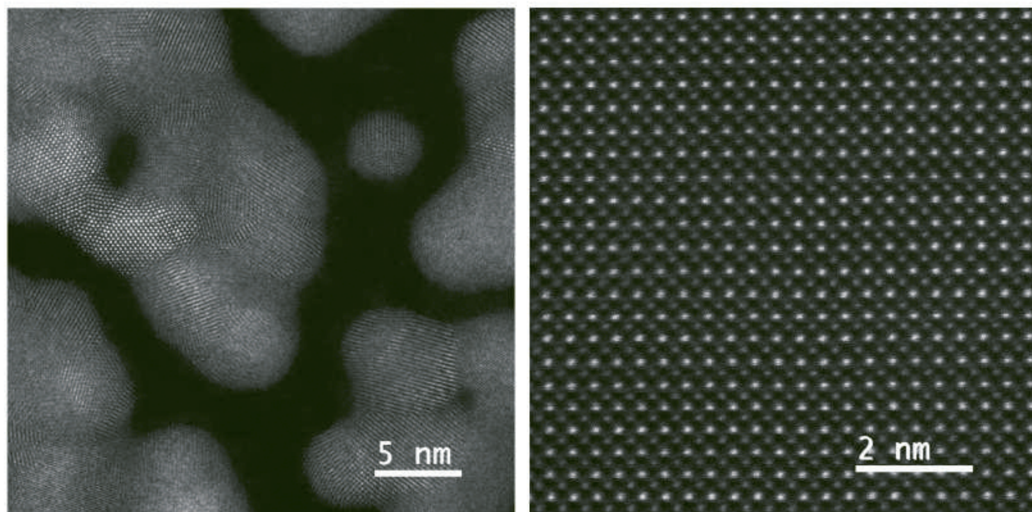

FIGURE 1.7: HAADF STEM images acquired at standard conditions for high resolution, 50 pA of beam current, 10 μs dwell time. The HAADF signal dependence on the atomic number, Z, allows for direct interpretation of the structure from the contrast in the images. Left, gold nanoparticles on carbon film. Gold nanoparticles are brighter than the carbon film, gold atomic columns and fringes can be distinguished. Right, $SrTiO_3$ (STO) crystal sample in [001] zone axis orientation. Sr atomic columns are brighter than Ti atomic columns.

Chapter 2

Distortions in STEM images

Along with the development of FEG electron sources and aberration correctors, improvements in the microscope environment (vibration damping, precise air conditioning and water cooling systems, acoustic and electromagnetic shielding, etc.) have also been key in the process to achieve sub-Å resolution [21]. The inherent serial acquisition of STEM makes this technique vulnerable to external and internal factors that create probe and sample instabilities with undesirable effects on the image quality. Currently, such factors cannot be completely countered and environmental disturbances can create unwanted imaging artefacts in even the most advanced STEM instruments. These distortions lower the accuracy and precision with which parameters can be obtained in a quantitative analysis. In HRSTEM, the precision with which the atomic column positions are determined is an important factor for crystal structure analysis and/or their defects, lattice parameter and strain measurement, etc. Values in the order of pm, lower than the image resolution, have been achieved by prost-processing techniques that partially overcome such issues [22, 23]. Here we will describe the main sources for distortions in STEM imaging as well as the conventional methods to reduce these problems which are based on post-processing algorithms.

2.1 Sources of distortions in STEM images

Perhaps the first critical factor when installing a new microscope is the location of the microscope room. Sources of ground vibrations, of a few Hz, can be busy roads or any laboratory equipment in the next room, or a close by building [24]. A slab of reinforced concrete or vibration dampers can mitigate the vibrations to the specifications given by the manufacturers [24]. Acoustic waves can be attenuated by covering the walls with a sound damping material made from fiberglass, polyurethane or other foams [24, 25, 26]. Air flow must be also reduced, adding a radiant cooling system and designing a laminar flow when working with air conditioning convection based systems [7] help in this task. Temperature variations of less than 0.25 °C per hour should be maintained in the microscope room [27] as this is a major source of sample drift, as it was mentioned earlier. Pressure fluctuations, coupled through the sample holder, can create distortions as the sample is in high vacuum while

the other side of the holder is at atmosphere pressure. The attenuation of sound vibrations and the laminar control of the airflow in the room will mitigate pressure fluctuations. For a schottky FEG microscope, working at 3×10^{-6} Pa, a deflection of 1 Å/Pa of the holder rod was measured [7]. Electro-magnetic interferences inside the column can drive the beam at the main frequency AC circuit, 50 Hz in Europe, or its harmonics. AC fields less than 0.01 μT root mean square (RMS) are advised near the column [27, 7]. Aberration-corrected microscopes may require magnetic shielded rooms, made from mu-metal, for the best performances [7]. In addition, ground currents should be avoided inside the room as these are sources of stray fields. The synchronization between the starting of each scan line with the phase of the external field helps to reduce these distortions [28]. When present, the effects can be revealed when evaluating strain with geometric phase analysis (GPA), as apparent expansion and contraction of the crystal lattice may occur [29, 30].

In general, we can classify the sources of distortions in STEM imaging as drift, scanning, and imaging system distortions, their effects are to distort the imaged atoms and induce a displacement from their actual positions. Here we briefly summarize these distortions.

2.1.1 Sample drift distortions

These distortions correspond to distortions of low frequency, less than 1 Hz [31]. According to the direction of the drift, either from the sample or stage, linear drift distortions can create expansion, compression and/or shearing of a crystal structure [32]. Non-linear drift can also occurs in the form of jumps of the sample position, for instance, creating discontinuities in the images. While continuous change of the drift direction can create curved atomic fringes [33]. The amount of drift distortions are proportional to the drift rate, in some cases it may be subtle to notice but might prevent crystallographic analysis. A skewed lattice image could be representative of the structure or the result of drift. In general, because of the longer acquisition time of a scan line compared to the dwell time, drift distortions result in an unequal effect on the fast versus the slow scan direction, with the slow scan direction being more prone to be affected by these distortions. Drift rate values of a few picometers per second are acceptable for HRSTEM imaging [34, 22].

2.1.2 Scanning distortions

Scanning distortions are mainly generated because of the finite time response of the scan coils and the bandwidth limit of the amplifiers driving them. The dynamic response of the coils is limited by its inductance and the Eddy currents in the deflector yoke, that oppose to changes in the excitation current and in the magnetic flux, respectively [35, 36]. In this thesis, we have already illustrated some of these distortions with the flyback motion while raster scanning. Even when a time delay is considered at the start of each line, distortion of the first few scan positions might be present as constant velocity is still building up.

The dynamic response of the scan coils can be approximated by a first order control system, with a time response for a step input signal given by the expresion

$$r(t) = 1 - e^{-t/\tau} \tag{2.1}$$

Where τ is a time constant that correspond to an amplitud response rise of 63%. During the transient period, a rise time t_s can be defined as the time the amplitude rises to 90%, Figure 2.1. In some cases, the rise time reported for a scanning system was several tens of μs [37], which is larger than standard dwell times in STEM imaging. A second order control system would be a more realistic approximation where undesired oscillations from an underdamped system are attenuated to reduce contributions to scanning errors, while still showing a fast rise time. This is a critically damped system.

In a similar way, stray fields can introduce intermediate (50/60 Hz and harmonics) to high frequency (radio frequency range, kHz - GHz) noise in the scan coils and induce scanning probe instabilities.

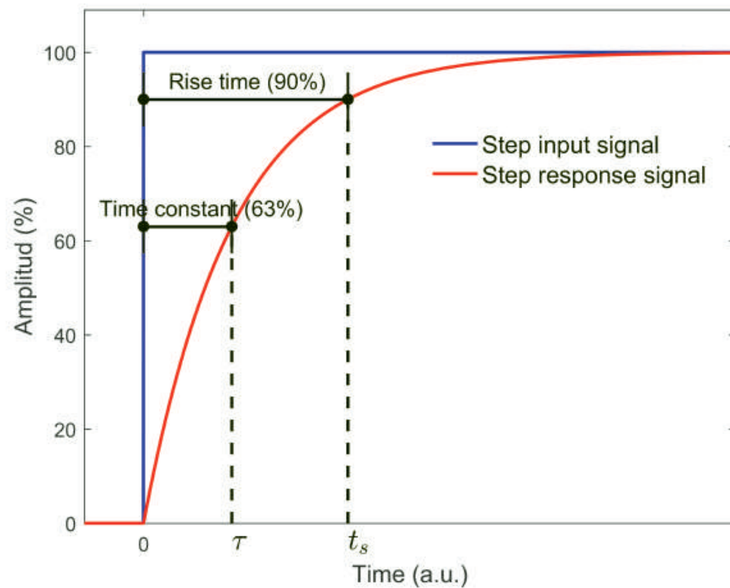

FIGURE 2.1: First order control system response to a step input signal, representing the dynamic response of the scan coils.

Because of the flyback motion, the slow scan direction of the raster method is more susceptible to scanning distortions.

Errors in the probe positioning can create misalignments between scanning lines, vertical and horizontal displacements, similar to the effect of drift. The distortions become far more obvious in a diffractogram, calculated by Fourier transforming images which contain periodic lattice features. Such diffractograms then typically show streaks in the vertical

(slow scan) direction as well as extra modulation peaks stemming from unwanted periodic modulation of the probe position (e.g. due to stray fields) [38, 34, 19].

Figure 2.2 shows a cropped area of an HAADF image acquired over a $SrTiO_3$ (STO) crystal sample oriented in [001] zone axis. The scanning was performed without any flyback delay with the effect of distorting the first left unit cells. The diffractogram, calculated from an area of the image not affected by the flyback motion, shows vertical streaks as a manifestation of random misalignment between consecutive scan lines because of drift and scanning probe instabilities.

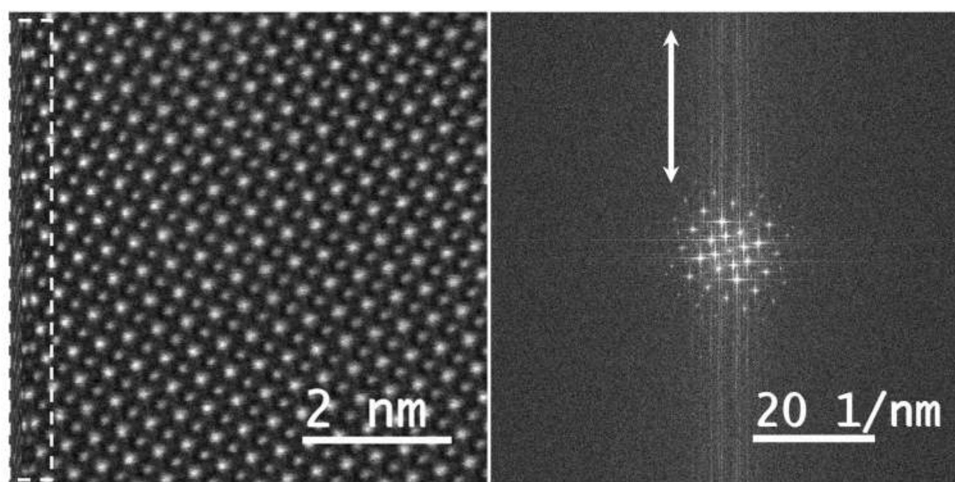

FIGURE 2.2: HAADF image acquired over a $SrTiO_3$ (STO) crystal sample in [001] zone axis orientation, acquisition at 4 μs dwell time. A cropped area is shown here. The first unit cells to the left are distorted because no flyback delay was applied. The difractogram shows vertical streaks mainly because of drift and scanning instabilities due to the finite time response of the scan coils and intermediate (50/60 Hz and harmonics) to high frequency (radio frequency range, kHz - GHz) noise induced to the coils by stray fields. The diffractogram was calculated from an area of the image not affected by the flyback motion.

The distortions can be classifed by their frequencies. In the literature, ground and acoustic vibrations coupled through the microscope column and/or the sample stage are commonly classifed as scan distortions, $\sim$ 1 - 100 Hz, and scan noise, $\sim$ 100 - 10 kHz, respectively [39]. With similar effects to the ones described here, horizontal and vertical misaligning between consecutive scan lines. As this section covers both frequency ranges, in this work, we categorize these distortions here.

2.1.3 Imaging acquisition system distortions

Besides the scanning distortions at high speed acquisitions, we also pointed out that at this condition the afterglow effect of the scintillator and the bandwidth limit of the detector system can induce smeared features. At moderate dwell times, these distortions can cause artificial anisotropy of the features of interest [16].

The detector acquisition system clearly has a time delay that must be compensated when synchronizing the scanning and acquisition system to form the images. Any remaining delay or even the settling time effect on probe positioning is less visible in raster scanning as it simply shifts the whole image (assuming adequate flyback time and avoiding the remaining distortions in the first few pixels of a row) [40]. Figure 2.3 shows a simplified block diagram of the STEM system and the main sources of image distortions. Electronic noise in amplifiers also lowers the data quality, however, time integration and averaging during reasonable dwell times reduce this problem. Table 2.1 summarizes the main sources of distortions in TEM along with typical remediations.

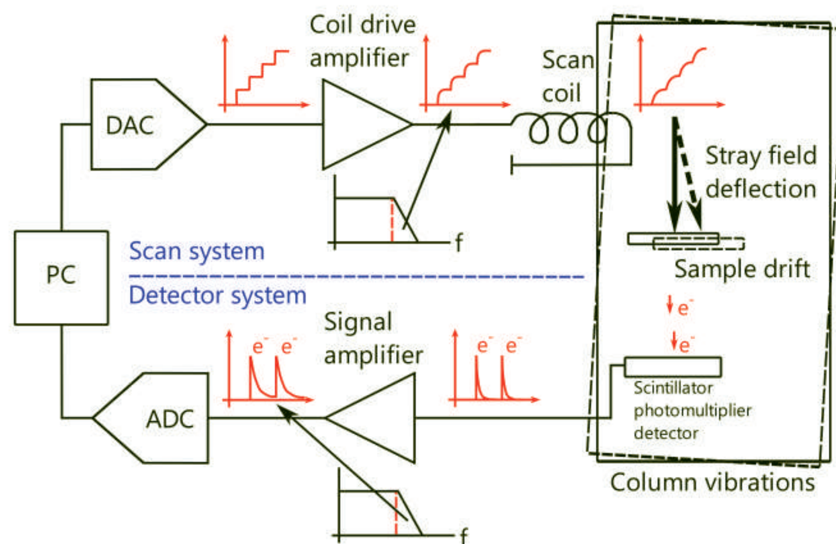

FIGURE 2.3: Simplified block diagram of the scanning (upper part) and detector (lower part) system in STEM. A digital signal to drive the coils is send by a computer (PC)/ microcontroller. The signal is converted into an analog signal by a digital to analog converter (DAC). The speed of the change in the probe positioning is limited by the bandwidth of the coil drive amplifier and the inductance of the scan coil. Electron events are detected by a scintillator-photomultiplier detector. The time decay of single electron events is explained by the effect of the scintillator afterglow and the bandwidth limit of the signal amplifier [18, 19]. The signal is digitized by an analog to digital converter (ADC), and stored and displayed by the computer system.

TABLE 2.1: Sources of distortions in transmission electron microscopy.

Source of distortion	Maximum magnitud	Frequency range	Countermeasure
Ground/microscope vibration (scanning distortions)	1 μm/s	1 - 5 Hz	Careful selection of the microscope room location. Microscope installed over a thick ($\sim$ 1 m) concrete slab. Vibration dampers. Remote operation. Air conditioning system with laminar airflow.
Acoustic noise (scanning distortions)	50 dB	0 - 2 kHz	Sound attenuator panels on internal walls. Microscope acoustic enclosure. Remote operation.
Temperature variation (drift distortions)	0.25° C per hour	Minutes to hours (< 1 Hz)	Avoid heat-generating electronics inside the microscope room. Air conditioning system. Radiation cooling panels on the wall.
External electromagnetic fields (scanning distortions)	0.01 μT	50/60 Hz	Avoid ground loops. Mu-metal (high permeability material) shielding. Active magnetic field cancellation system. Line synchronization at 50/60 Hz.
		Radio frequencies (kHz - GHz)	Microscope column shielding.
Electronic noise in amplifiers (imaging acquisition system distortions)	A/$\sqrt{\text{Hz}}$	Hz - MHz	Low noise design. Cooling system to reduce thermal noise. Time integration and averaging.

2.2 Conventional methods to address scanning distortions, post-processing techniques

A considerable number of theoretical models and algorithms have been proposed to address distortions in images acquired with raster scanning. Some of these methods are based on multiple acquisitions and applying a frame-averaging afterwards, which can also increase SNR [31]. Here we shortly describe different approaches to correct for these distortions.

A set of images can be simply aligned by a rigid registration considering only translations, the same translation vector is preserved for all the points in the images, such as in the work from K. Kimoto. et al. [22] and D. A. Muller et al. [25] (based on cross-correlation to track the drift vector). However, this method only correct drift displacements between acquisitions, e.g. any shearing in the images will still remain. Averaging individual frames that suffer from other higher frequency ($\sim$ kHz or more) scanning distortions usually induces blurred features and hence a loss of resolution. This type of distortions can be addressed by non-rigid registration methods as it is mentioned later in this section.

Affine transformation methods can be considered to correct the remaining linear drift distortions. The RevSTEM method, developed by X. Sang et al. [32], was proposed to correct dilatation, contraction and/or any skewing of the crystal lattice, and without prior knowledge of the sample structure. Multiple acquisitions are performed while rotating the scan coordinate system between frames. The drift direction and rate can be estimated from the change in image distortions at each rotation angle, by measuring the lattice vector angles over the acquired series, and an inverse affine transformation matrix can be calculated to restore each of the images. The restored images are registered and averaged by using the previous approach.

An approach to a non-rigid registration method is given in the work from J. Lewys et al. [34]. Scan high frequency distortions in single atoms or atomic columns can be reduced in both scan directions. A pixel of interest is centered in a row of a few pixels length, and a cross correlation method is applied to compare this row with rows of equivalent length positioned above and below. An optimal shift is obtained that represent the error in the horizontal probe positioning of the pixel of interest. In the vertical direction, the distortions are corrected by analyzing integrated profiles of a feature of interest and re-ordering the rows to obtain a decaying smooth profile with the brightest pixel in the central row. Linear drift correction is based on a prior knowledge of the crystal structure.

Further methods to correct scanning distortions and drift based on non-rigid registration of a series of images have been developed [39], and ultimately corrections from a pair of images acquired with orthogonal scan directions can be found in the work from N. Sang. et al. and C. Ophus et al. [38, 33].

Some disadvantages can be linked to the approaches described here like cropping of the imaged areas, not preserving the acquired pixel intensities when applying interpolation methods, etc. A question arises for the methods based on multiple-frame acquisitions, how many acquisitions are required? This question becomes more critical if working with electron beam sensitive samples, as the electron dose (number of electrons per unit area) will increase with the number of acquisitions. The work from L. Jones et al. suggests that 70% of scanning artefacts can be reduced with 20 - 30 acquisitions [31], no further improvement was observed with more acquisitions. Increasing the number of acquisitions implies conditions of extreme low electron dose per frame and high speed acquisitions with degraded data quality (low SNR in individual images, and scanning and imaging acquisition system distortions) that can not be properly registered. The work from I. Maclaren et al. reported dwell times in the range of 5 - 10 μs for individual frames [41]. As a result, optimal conditions of multiple acquisition approaches suggest high total electron doses.

2.3 Approach to non-conventional methods to address scanning distortions

As it was highlighted before, when performing fast imaging acquisitions, lower image quality is expected because of the scanning and acquisition system distortions. Moreover, the raster scan method, although implemented to reach a constant speed in each scan line, has discontinuities that create instabilities of the probe and makes this pattern far from being the optimal acquisition method. The algorithms listed above address distortions that rely on data treatment post-acquisition, with the drawbacks that these methods convey. Acquisition scanning methods that do not induce or enhance such distortions would be preferably before any post-processing.

In strain analysis, a simple procedure to circumvent the distortions when raster scanning is to align the fast scan direction parallel to a principal axis of strain. A pair of images can be acquired perpendicular to each other in the same area of interest. From each of the acquisitions, the strain components calculated in the slow scan direction are usually discarded [30, 42, 43]. This approach circumvents the scanning distortions in the order of kHz that induces missaligned scan lines. Higher frequency distortions within scan lines will remain as well as drift distortions.

However, in STEM imaging only a modest number of investigations have focused on alternative scanning paths to reduce scanning distortions. One example is the spiral scanning paths that were investigated by X. Sang et al. [44, 45] as a method to acquire images at extremely high speed without the need of a flyback delay and with a near single harmonic frequency spectrum of the scan coil drive signals. Different spirals scans were investigated and classified as constant angular velocity and constant linear velocity spirals, but both

suffer from non-uniform image quality over the scanned area. In the first case, to keep the angular velocity constant, the sampling density and applied dose on the edges is lower than in the central region. In the second case, to keep the linear velocity constant and the sampling density and applied dose uniform, the beam moves faster in the central region than on the edges possibly creating image distortions as the scan system can have a frequency dependent amplitude. A post-processing step is needed to correct for this distortion. With this scan method, drift distortions could be reduced as there is not need for flyback time delay and high speed acquisitions could be performed. In addition the use of a continuous path would eliminate missaligned lines.

Chapter 3

Electron beam damage

For many important classes of materials, e.g. zeolites, organic, biological materials, etc., electron beam damage in transmission electron microscopy is a detrimental effect that limits the capabilities to obtain information at different length scales. Displacement of atoms and consequent structure degradation is the result of the interaction between the highly energetic electrons and beam sensitive materials. These effects can be increased in modern microscopes equipped with bright FEGs as higher electron current densities can be obtained compared to thermionic guns. Besides the correction of aberrations and the attenuation of environmental distortions discussed in the previous chapters, for beam sensitive materials, the ultimate resolution achievable in aberration-corrected TEMs is dictated by the electron dose that the sample can withstand [46].

The primary mechanisms of beam damage are knock-on and radiolysis (or ionization), which can be material dependent. In this chapter we summarize these mechanisms.

3.1 Knock-on damage

Knock-on damage originates from the electrostatic interaction of an incoming electron (primary electron) and an atomic nucleus. The energy that is transferred to the atomic nucleus when an electron suffers an angular deflection θ is given by the expression [47]:

$$E = E_0 \sin^2(\frac{\theta}{2})(1.02 + \frac{E_0}{10^6})/(465.7A) \tag{3.1}$$

Where E_0 is the energy of the incident electron (in eV) and A the atomic mass number. For small scattering angles (around 100 mrad), the energy transferred is $\ll 1$ eV [46], and it can be considered an elastic interaction (as in DF STEM imaging). However, backscattered ($\theta > \pi/2$) electrons can transfer several eV. This energy increases when the incident energy E_0 increases and decreases as the atomic number increases. The maximum transferred energy corresponds to electrons scattered at π rad.

By this means, atoms can be displaced to interstitial positions and deteriorate the structure of a crystal. The displacement energy E_d required for an atom to be displaced by knock-on damage also depends on the crystal lattice, coordination number, bond strength (which energy can be in the order of a few eV), and it is higher for atoms in a bulk crystal (generally above 10 eV [48]) than for atoms in a surface where the coordination number is lower. The last process is also called sputtering. The energy that is needed for the incoming electrons to create atomic displacement is obtained by setting E_d equal to the maximum transferred energy. Table 5.1 shows the displacement and threshold energies for some common materials. For a compound, the threshold energy is usually determined by the threshold energy of the element with the lowest atomic number. Knock-on damage is dominant in electrical conductive materials, this type of materials are mostly not affected by radiolysis as we will see next. Although organic materials can be also affected by knock-on mechanism, usually the cross section (or the probability of the interaction to occur) of this interaction is small compared to the cross section of radiolysis. To mitigate or even stop knock-on damage, the energy of the incoming electrons can be reduced to the threshold energy or lower. For example, the reported threshold energy for graphene is 80 keV, damage starts above this energy [49, 50]. However, when reducing the incident electron energy, the radiation damage by ionization process may increase as the cross section of this inelastic interaction depends inversely on E_0 [46].

TABLE 3.1: Displacement and threshold energies for some common materials [47, 51].

Material	E_d (eV)	E_0 (keV)
Diamond	80	330
Copper	20	420
Aluminum	17	180
Magnesium	10	101
Gold	34	1320

3.2 Radiolysis

Radiolysis damage is the result of an inelastic interaction between an incident electron and an atomic electron. Irreversible damage happens if the excitation last for a period of time sufficient for the atoms to be displaced from their positions, and consequently destabilizing the structure. The atoms can be displaced by the momentum transfer from atomic vibrations or phonons (excitations of < 0.1 eV), which have a vibration period in the order of 0.1 ps [52]. Phonons can be generated via direct electron-lattice interactions or as a side effect of the inelastic interactions described here. The interaction of the incident electron with

free electrons in metals or with the bounded valence electrons in insulators or semiconductors, which is also an inelastic interaction, can induce a collective oscillation of the electrons called plasmon. Although plasmons have a higher cross section compared to ionization, these oscillations are damped out in fs [2], before any atomic displacement can occur.

The energy transferred to the atomic electrons generates electronic transitions. In the case of metals or a good conductor, transitions from the valence or conduction band leave vacancies or holes that can be filled by any of the conduction electrons in < 1 fs [52], a time-scale shorter than the atomic vibrations.

In insulators or semiconductors, the electrons can be excited either from the valence band or from an inner-shell. The excitation energies for transitions from the valence band can be up to ~ 25 eV [2]. As the concentration of electrons in the conduction band is very low, the holes are filled in a longer time than in conductors (in μs for semiconductors, or even longer for insulating materials). During this time the exited atom can experience a displacement (with a probability that depends on the bond dissociation energy [53]) due to the increased vibrational level at the excited state and the momentum transfered from phonons; an irreversible breakage of a chemical bond that can lead to desorption and mass loss of the sample. The exited electrons are secondary electrons that are free to move and can potentially create further electron-hole pairs.

To excite an electron from an inner-shell, energies above ~ 50 eV [2] are required. This is called inner-shell ionization. Excited electrons with this amount or energy are called fast secondary electrons and can travel to a distance of a few nm from where the primary electron hit and caused the initial excitation. In polymethyl methacrylate (PMMA) most of the damage is considered to be from the inelastic interactions of the secondary electrons rather than from the interactions of the primary electrons, based on an analytical electron-resist interaction model calculated by B. Wu et al., which is believed to be the reason of the limited spatial resolution in electron beam lithography ~ 10 nm [54]. The excited atom can get back to its ground state energy if an electron from an outer-shell fills the hole in the inner-shell, releasing a characteristic X-ray (which is the EDX signal that is collected in TEM). Alternatively, an electron from an outer shell can be released, called Auger electron, and create damage in a similar way the secondary electrons do.

The energy released from excitations of valence electrons is lower than from excitations of inner-shell electrons; however, its cross section is higher than the ionization cross section [2]. Although the dominant process may be different for different materials, in general these mechanisms are called radiolysis or ionization damage. R.F. Egerton summarizes radiolysis damage as a three step process in which bond breakage and secondary electron generation correspond to the first stage and happens on a time scale of sub-fs, in the second stage, atomic displacement and loss of crystallinity occurs on the range of tens of fs, and finally the third stage (on a larger time range) that corresponds to mass loss (that involves atom displacement over larger distances) [55].

3.3 Beam damage as a diffusion process

In TEM, it is well known that beam damage can extend over an area larger than the size of the irradiated area [56, 57]; as it was suggested for example by the damage created by secondary electrons generated during radiolysis. However, this effect may have many other causes which can itself depend heavily on the material: diffusion of heat, generation and diffusion of radicals, electrostatic charge and dielectric breakdown, delocalized inelastic scattering, etc. [57, 58, 59, 54].

Most of these effects are triggered primarily by ionization where a fraction of the energy from the incoming electrons is transferred to the sample with a subsequent energy transformation which can be recurrent during damaging until all primary energy is dissipated. This mechanism is dynamic in nature and has both a spatial and temporal scaling parameter that can be described as a diffusion process.

In this section we describe some time dependent mechanisms that can be sources of a diffusion process.

3.3.1 Possible time dependent damage mechanisms

Heating

Heating can affect specimens with low thermal conductivity, k, such as certain polymers as in the case of polystyrene ($k \sim 0.04$ W/mK) [60]. Besides the good thermal conductivity of metals ($k > 100$ W/mK), these materials can also be affected by heating at high electron beam currents. In a FEG-TEM at 200 kV, vaporization of solid gold have been reported at beam currents of 5 nA, with a probe size diameter of 0.5 – 1 nm [61]. R. F. Egerton et al. estimates the temperature rise (ΔT) for a thin specimen at steady state conditions, at which the heat generation is balanced by heat loss (mainly due to radial conduction) and a radiation term is neglected [47],

$$\Delta \mathrm{T} = \frac{I\langle E\rangle(0.58 + 2ln(2R_0/d))}{4\Lambda\pi k} \tag{3.2}$$

with I as the electron beam current, $\langle \mathrm{E}\rangle$ the mean energy loss per inelastic collision, Λ the inelastic mean free path, d the diameter of the incident beam and R_0 the radial distance of a given point with respect to the center of the beam.

The temperature rise for carbon (usually used as support film in TEM grids) with parameters $k = 1.6$ W/mK, $\Lambda = 150$ nm, $\langle \mathrm{E}\rangle \sim 40$ eV, for a beam current between 10 – 2000 pA at 200 kV [46] can be calculated, shown in Figure 3.1. The temperature rise is obtained for two different beam size diameters, 1 μm and 0.8 Å, and a radial distance $R_0 = 30$ μm, typical distance from the beam to the TEM metal grid (usually made from copper). ΔT is less than 0.2 K for the two cases at 50 pA beam current, typical current for an aberration-corrected

probe in STEM mode. ΔT is less than 2 K at 400 pA, while the difference between the curves is only 1 K. This plot also suggests that the temperature rise in STEM imaging is similar to the obtained in TEM imaging [47].

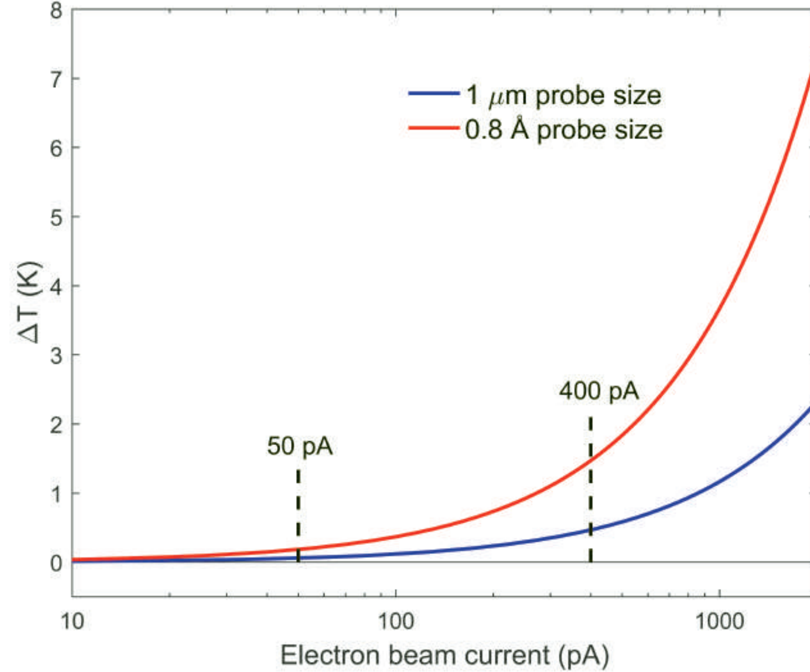

FIGURE 3.1: Temperature rise (calculated using equation 3.2) for a carbon film with parameters k = 1.6 W/mK, Λ = 150 nm, $\langle E \rangle \sim 40$ eV at 200 kV [46]. ΔT is calculated for two different beam size diameters, 1 μm and 0.8 Å, and a radial distance R_0 = 30 μm, typical distance from the beam to the TEM metal grid. X axis in logarithmic scale.

Although, at standard conditions of TEM imaging, the heating effect seems to be negligible, several works have demonstrated that working at cryogenic temperatures mitigates beam damage degradation. E. Tyukalova et al. reported phase transformation of energy related materials ($LiNi_{0.5}Mn_{1.5}O_4$ and $ZnCo_{1.8}Ni_{0.2}O_4$) while acquiring HRSTEM images at room temperature. At cryogenic temperatures, an increased electron dose (three to four times the electron dose applied at room temperature) was needed to observe phase transformation [62]. Although the inelastic interactions are not influenced by the temperature, the mobility of the radiolysis products and atomic displacement is reduced at lower temperatures, allowing the retardation of phase transformation at cryogenic temperatures [63].

Electrostatic charging

Secondary and Auger electrons are generated during the radiolysis process; these electrons can travel away from the probe position. In an insulator, this process generates an electron depletion region, leaving the irradiated column on the specimen positively charged [64],

illustrated in Figure 3.2. The electric field within the irradiated area and the surrounding shows a cylindrical symmetry with respect to the irradiated column and strength proportional to the accumulated charge ρ [65]. An electric force can potentially drive ions from their positions or even create dielectric breakdown. The driven mechanism for the diffusion of calcium (Ca) ions on glass materials, like $CaO - Al_2O_3 - SiO_2$ and $CaF_2 - Al_2O_3 - SiO_2$, under the irradiation of an electron beam was presumed to be electrostatic forces when electrostatic charge built up on the irradiated sample [66, 67].

The charge density builds up during irradiation. When the irradiation is stopped, the charge density varies with time as [64]

$$\rho = \rho_0 e^{-t/\tau_r} \tag{3.3}$$

Where ρ_0 represents the initial charge density and τ_r the relaxation time

$$\tau_r = \varepsilon_0 \varepsilon_r \rho_r \tag{3.4}$$

ε_0 being the permittivity of free space, ε_r the relative permittivity of the material and ρ_r the electrical resistivity of the material. Materials like soda-lime glass (commonly used for glass bottles) with resistivity in the order of 10^{10} Ωm shows a relaxation time in the order of s, while for SiO2 (silica) with a resistivity $\sim 10^{17}$ Ωm it can be in the order of days [65]. Most of the insulators have a resistivity in the range 10^5 – 10^{16} Ωm, with relaxation times higher than μs.

In TEM, the sample is grounded through the carbon film and the copper sample grid. The secondary electrons may flow through the ground to avoid charging effects. However, in a poor conductor, most of the charge accumulates on the insulating sample. Resembling an RC electrical circuit with a time constant τ_r = RC, with R the resistance of the sample and C its capacitance. Figure 3.2 (right) depicts the case when the irradiation is stopped.

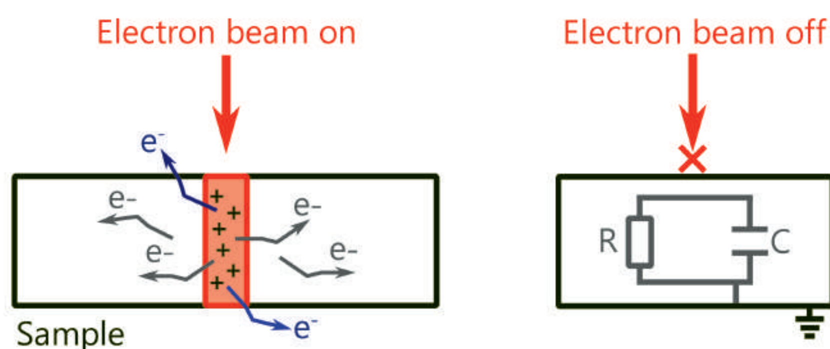

FIGURE 3.2: Left, diagram showing the positively charged column through the sample created by the electron beam. The secondary electrons (alternatively Auger electrons), created because of the radiolysis damage, leave the irradiated region. Right, interpretation of the electrostatic charging effect in an insulator sample as an RC electrical circuit.

3.4 Methods to address beam damage-radiolysis

While knock-on damage can be controlled by reducing the energy of the primary electrons, radiolysis damage is commonly considered to be proportional to the total electron dose that is applied to the sample. Indeed, beam damage on highly beam sensitive materials like organic and biological materials is often quantified from the fading of diffraction spots (or rings) during irradiation. The intensity of the spots commonly decreases when increasing the electron dose by irradiating the sample for a longer time [68, 69, 70].

The electron dose is calculated by multiplying the electron dose rate (number of electrons per unit area per second) and the irradiation time. The electron dose rate is obtained from the division between the electron beam current (expressed in electrons per second knowing the charge of an electron is $e^- = 1.6 \times 10^{-19}$ C) and the irradiated area. An electron dose threshold is commonly defined as the dose at which the damage starts to be significant to hinder the analysis of the acquired information.

Conventional methods to reduce radiolysis effects are based on low dose techniques [19]. In STEM imaging the size of the electron probe is maintained at a constant size. The irradiated area is calculated multiplying the pixel size by the number of scanned pixels; in the x and y scan directions. The irradiation time is obtained multiplying the dwell time by the total number of scanned pixels. The electron dose per acquisition can be easily calculated. For beam-resistant materials, in HRSTEM, the electron dose for imaging is usually in the range of $\sim 10^4 - 10^6$ $e^-Å^{-2}$ to obtain high quality images. This is the case for the images shown in Figure 1.7, chapter 1, an electron dose in the order of 10^5 $e^-Å^{-2}$ was employed for the acquisitions.

At a given magnification, low dose can be reached by making fast acquisitions (reducing the dwell time in STEM) or lowering the beam current; a combination of both approaches can be used to reach values comparable to low dose TEM [19]. A more relatively recent non-conventional strategy to reduce beam damage in TEM involves a compressed sensing (CS) approach. These methods are described in the following.

3.4.1 Conventional low dose techniques in STEM imaging

Making fast acquisitions or lowering the beam current to work at low dose conditions may degrade the image quality. As it was described in the previous chapters, high speed acquisitions will induce streaking artifacts because of the finite time response of the scan system. While, in general, reducing the electron dose will decrease the SNR due to the inevitable Poisson noise effect.

Besides the fact that at a given dose, the different approaches for low dose may show different image quality, experimental works have shown that the total electron dose is not the only factor to consider in beam damage. Dose rate (or beam current) effects may also play an important role. A. C. Johnston-Peck et al. reported a dose rate threshold for cerium dioxide (CeO_2) for which no structural changes were observed in STEM images as well as in the Ce $M_{4,5}$ edges monitored by EELS, no matter the amount of electron dose [71].

In this work, different damage effects of dose and dose rate were observed on a copper (Cu) based compound crystalline sample. This test sample[1] is a porous Cu-compound that exhibits high sensitivity under the electron beam. The experiments were carried out on a probe aberration-corrected Thermo Fisher Scientific TITAN[3] microscope, operated at 300 kV, with 50 pA and 25 pA of beam current[2] and a spatial resolution of approximately 0.8 Å. To avoid additional damage because of the extra dose when flyback delays are applied, images (with a frame size of 512 × 512 pixels) were scanned without any time delay. All the acquisitions were done over the same crystal on a large area of uniform thickness.

Working with 50 pA beam current, damage was observed on the lower area of the acquisitions with a dose of 2.1×10^4 $e^- Å^{-2}$, scanning at 8 μs dwell time and 34.3 pm pixel size; structural damage and change in the contrast as shown in Figure 3.3.b. More damage was observed for acquisitions with a higher dose, 3.2×10^4 $e^- Å^{-2}$, scanning at 12 μs and 34.3 pm pixel size; amorphization on the lower half of the acquisition on Figure 3.3.c. The beam current was reduced to 25 pA, which gives half of the previous dose rate, scanning with the same pixel size as before. In this case, no damage was observed for acquisitions

[1]This sample was kindly provided by Professor Robert Raja, from University of Southampton, head of the Functional Inorganic Materials Group (FIMS). More information about this sample and its study will be given in a future work.

[2]Beam currents as low as 40 pA can be measured from a pico-ammeter connected to the flu-screen. Lower currents can be estimated by acquiring a diffraction pattern of the carbon film with the CCD camera (typically used in TEM), previously calibrating its output in counts to the current measured from the pico-ammeter at higher currents. Due to the linear response of the camera, a beam current of 25 pA could be estimated.

with a dose of 2.1×10^4 e$^-$Å^{-2}, scanning at 16 μs dwell time; Figure 3.3.d. With a dose of 2.7×10^4 e$^-$Å^{-2}, 20 μs dwell time, damage was not observed either; Figure 3.3.e. Some damage on the lower area starts to be visible for acquisitions with a dose of 3.3×10^4 e$^-$Å^{-2}, 25 μs dwell time; Figure 3.3.f. Apparent formation of clusters was noticed even at the lowest dose applied here where no structural damage was observed, for both dose rates. The clusters can be identified as bright spots on the acquisitions of Figure 3.3. The scanning conditions used to acquired the images shown in Figure 3.3 are given in Table 3.2.

The effects of dose rate point to the temporal dependence of the various stages of radiolysis damage. Although understanding the exact damage mechanism in this sample would be challenging (as it would be the case for most beam sensitive materials), the process can be simplified considering two rates: a damage rate and a dissipation or recovery rate. Accumulation of damage would happen if the damage rate is higher than the last one [67]. As more interactions per unit of time would lead to a higher damage rate, most likely, this factor is proportional to the dose rate. Then the accumulation of damage can be controlled with this parameter, and the damage can be slowed down (or even stop it) as it was the case for the present test sample. A dissipation or recovery rate could depend on the thermal conductivity of the sample or its electrical conductivity, for instance. K. A. Mkhoyan et al. reported the diffusion of Ca ions in thin films of $CaO - Al_2O_3 - SiO_2$ when irradiating with an electron beam. Full recovery after mass migration from the damaged area was noticed. Electrostatic charging was presumed to be the reason for damage; however, the driving forces of the Ca atoms that diffused back remain unclear [66].

TABLE 3.2: Scanning conditions used to acquire images in Figure 3.3.

<table>
<tr><th>Image</th><th>Beam current (pA)</th><th>t_{dwell} (μs)</th><th>Pixel size (pm)</th></tr>
<tr><td>a</td><td rowspan="3">50</td><td>8</td><td>48.5</td></tr>
<tr><td>b</td><td>8</td><td rowspan="2">34.3</td></tr>
<tr><td>c</td><td>12</td></tr>
<tr><td>d</td><td rowspan="3">25</td><td>16</td><td rowspan="3">34.3</td></tr>
<tr><td>e</td><td>20</td></tr>
<tr><td>f</td><td>25</td></tr>
</table>

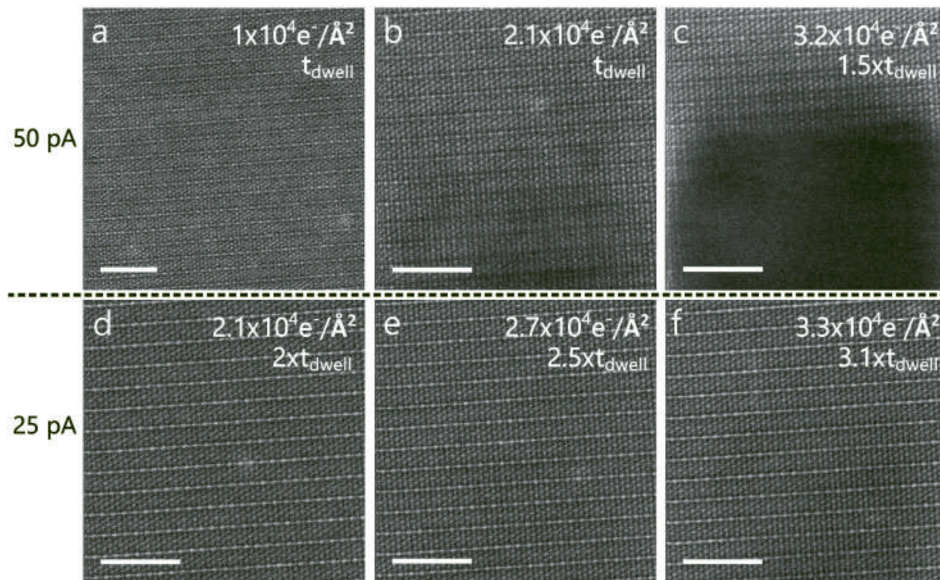

FIGURE 3.3: Images acquired on different areas of a crystal Cu-compound sample of uniform thickness. Acquisitions were done at different beam currents, 50 pA (a, b and c acquisitions) and 25 pA (d, e and f acquisitions). a. No structural damage was observed scanning at t_{dwell} = 8 μs, 48.5 pm pixel size. b. Damage on the lower area is observed scanning at t_{dwell}, 34.3 pm, indicated by contrast change. c. Amorphization on the lower half area is observed scanning at $1.5 \times t_{dwell}$, 34.3 pm. At 25 pA beam current, half the dose rate for the previous acquisitions at 34.3 pm pixel size, structural damage was not observed scanning at $2 \times t_{dwell}$, shown in d and same dose as in b. Damage on the lower area starts to be visible for acquisitions at approximately $3.1 \times t_{dwell}$, shown in f and similar dose as in c. The scale bar represents 5 nm.

3.4.2 Non-conventional low dose techniques in STEM imaging-compressed sensing

A more relatively recent non-conventional strategy to reduce beam damage in TEM through dose reduction involves a compressed sensing (CS) approach. In the theory of CS a faithful representation of a signal can be retrieved from a random undersampling data acquisition, under the assumption that the signal has a sparse representation in a properly chosen basis [72, 73]. Undersampling the data randomly ensures that the artefacts induced in the sparse basis resemble incoherent noise. The data can be retrieved by algorithms that promote sparsity, by inpainting methods, interpolation schemes, deep learning/neural networks, etc. [74, 75].

In the theory of CS a signal x of length n is represented in a n×n sparse basis Ψ, with $x = \Psi f$ and f with k non-zero components, $k \ll n$. The measurement matrix Φ is a m×n matrix and the recordings y are of length m with $m \ll n$,

$$y = \Phi\Psi f. \tag{3.5}$$

Applied to STEM, it is possible to obtain a faithful restoration of an image by scanning only a subset of the scan positions than on a conventional scan acquisition. To reduce scan distortions that would be induced by large jumps of the probe as in a completely random scanning, usually a random selection of positions are scanned in each line of a raster method. Atomic-resolution imaging with as little as 20% of the pixels have been demonstrated in STEM; either by fast blanking of the beam during scanning or by directly controlling the scan coils [76, 37]. A few scan strategies have been proposed in STEM imaging with CS to alleviate the scan distortions induced by the non-constant speed of the probe during the acquisition; a line-hopping scan where the speed of the probe is constant in the fast scan direction and the beam moves randomly across the slow scan direction [37], and non-rectangular strategies based on spiral scans [75, 77].

In a collaborative work with Dr. W. Van den Broek and Prof. Dr. C. T. Koch, from the department of Physics of Humboldt University of Berlin, we have shown that from a statistical point of view, CS does not present any improvement compared to denoising of standard sampling acquisitions. The result holds for both acquisition systems with equivalent electron dose and under the assumption of Poisson noise only, which is the case for particle counting experiments as when detecting electrons in TEM [78]. This was shown by the comparable reconstruction of CS acquisitions with the denoised version of noisy acquired images, and by comparing the amount of information from the recordings with both methods, which did not show any increase with CS. While others have obtained similar results through simulations [79], H. Vanrompay et al. reported experimental results in

agreement with this conclusion, electron tomography[3] reconstructions of a gold nanorod did not show any benefit acquiring 2D projections at each tilt angle with CS compared to acquisition where the same electron dose was distributed over all the pixels [80].

In this work we also demonstrate the application of CS in STEM to retrieve HR images of a beam sensitive sample. This method was tested on the highly beam sensitive porous Cu-compound sample. An external hardware was employed to control the probe positioning; more details about the hardware are given in the next chapter. The undersampled acquisitions were reconstructed using the spgl1 algorithm [81] which can solve the following optimization problem,

$$\text{minimize}\|f\|_1 \text{ subject to } y = \Phi\Psi f \tag{3.6}$$

where $\|\|_1$ is the $l1$ norm, which is the sum of the absolute values of the vector elements.

The acquisitions were done with a beam current of 25 pA, at 17.2 pm pixel size. A raster scanned image (512×512 pixels) acquired at 8 μs dwell time is shown in Figure 3.4 (left). The image was acquired with a dose of 4.2×10^4 e$^-$Å^{-2}, no flyback delay was employed. Structural damage is observed on the lower area of the acquisition. A CS acquisition was performed on a frame of 1024×1024 pixels scanning only 20% of the pixels, at 18 μs dwell time, with a dose of 1.9×10^4 e$^-$Å^{-2} (similar dose as for the acquisitions in Figures 3.3.b and 3.3.d). A cropped area of 512×512 pixels of the reconstructed version of the image is shown on Figure 3.4 (right).

Contrary to the theoretical calculations that have shown no benefit of CS compared to denoising at constant dose, we did observe some improvement from the experimental CS acquisitions, Figure 3.4. Indeed, in CS acquisitions, the average distance between consecutive pixels is larger than in conventional scanning. If the way the electron dose is spatially and temporally distributed on the sample does matter for beam damage, intuitively, one could imagine that this larger distance between sampled points could prevent damage accumulation by outrunning the diffusion-like effects coming from earlier scanning points. The temporal and spatial dependency of damage observed during this work lead us to propose a scanning method that allows the manipulation of this parameters during the acquisitions, which is shown in chapter 5.

3.4.3 Dose fractionation technique in STEM imaging

As it was mentioned in the previous chapter, multiple short acquisitions and registration procedures can be performed to improve image distortions. This methodology fractionates the available electron dose by scanning with a shorter dwell time that would be otherwise

[3]In electron tomography a 3D structure is retrieved from 2D projections acquired at different tilt angles.

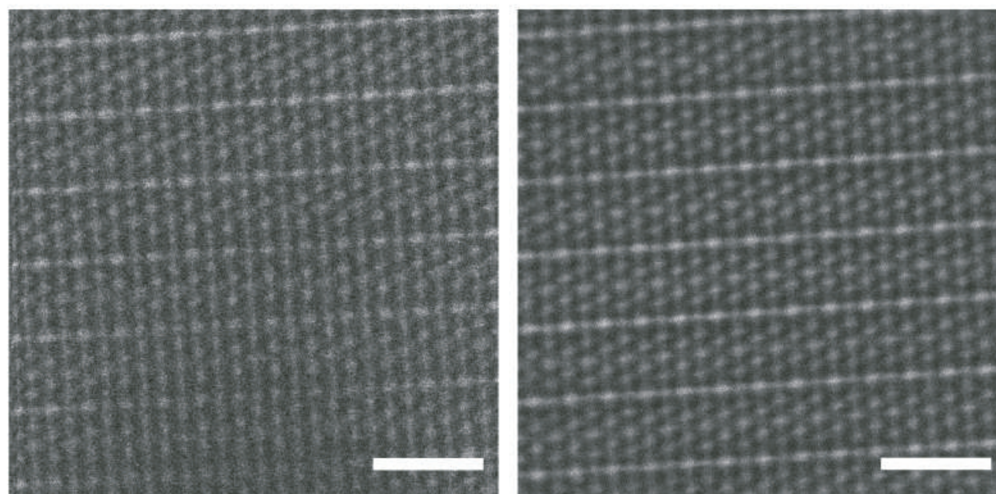

FIGURE 3.4: Raster and compressed sensing (CS) acquisitions with a beam current of 25 pA, at 17.2 pm pixel size. Left, raster acquisition (512×512 pixels) at 8 μs dwell time with a dose of 4.2×10^4 $e^- Å^{-2}$, no flyback delay was employed. Right, reconstruction of a CS acquisition. Only 20% of the pixels of a 1024×1024 frame were scanned at 18 μs dwell time, with a dose of 1.9×10^4 $e^- Å^{-2}$ (similar dose as for the acquisitions on Figures 3.3.b and 3.3.d). A cropped area of 512×512 pixels is shown here. The scale bar represents 2 nm.

employed in a single acquisition. Although the conditions for optimal distortion corrections suggest the use of high electron doses [31, 41]; experimental results have expose its applicability in damage reduction.

L. Jones et al. compared acquisitions under a fixed total dose and dose rate on a lead perovskite (Pb_2ScTaO_6); fast scanning multiframe acquisitions with equal dose per frame provided reduced sample degradation compared to a single acquisition in STEM imaging and EELS spectrum imaging (SI) [82].

Similar to the dose rate effects, dose fractionation can be related to the dynamic of the damage process. As suggested by the time scale between acquisitions, it may influence the latest stage of this process.

Chapter 4

Scan strategy to address drift and scanning distortions in STEM

From the discussions in chapter 1 and 2, we can imply that the images we acquire are a distorted version of the real objects we try to register. Although significant progress in probe forming systems and environmental disturbances has been achieved, little attention has been put on the scanning instabilities. As we revised earlier, much of these instabilities are caused because of the raster method itself, due to the large speed difference between the x and y scan direction and the interruption of the probe movement after each scan line, which results in non-isotropic deformations in the final image. The immediate remedy was focused on post-processing techniques rather than improving the scanning method.

A first approach given by the spiral scanning methods [44, 45] illustrates the need for improving the serial acquisition in STEM. An alternative scanning method that avoids discontinuities (such as big flyback jumps), delays, and improves on drift induced distortions, and requires no post-processing would be attractive.

We have investigated two different continuous patterns, snake and Hilbert pattern (the Hilbert pattern is a type of space filling curve [83] which provides a more isotropic scanning), and quantitatively compared them to the raster scanning in terms of distortions on the shape of atomic columns and in terms of lattice distortions on a single crystal sample. Here we also show that both are complementary means to measure image quality depending on the specific research goal.

4.1 Hardware to control the scan engine of the microscope

A custom hardware scan engine [84, 85] was employed to control the scan amplifier inputs of the microscope and to record the high-angle annular dark-field (HAADF) signal. A field programmable gate array (FPGA) controls the synchronized feeding of the high speed digital to analog converters with a programmable pattern while sampling the input with an analog to digital converter. The recorded signal is then progressively displayed in a 2D array according to the scanning sequence.

4.2 Continuous scan strategies without flyback compensation for STEM

The snake and Hilbert methods are illustrated in Figure 4.1. The snake and Hilbert scanning eliminate the need for flyback delays while the pixel size is kept constant for all the cases. The patterns are described below.

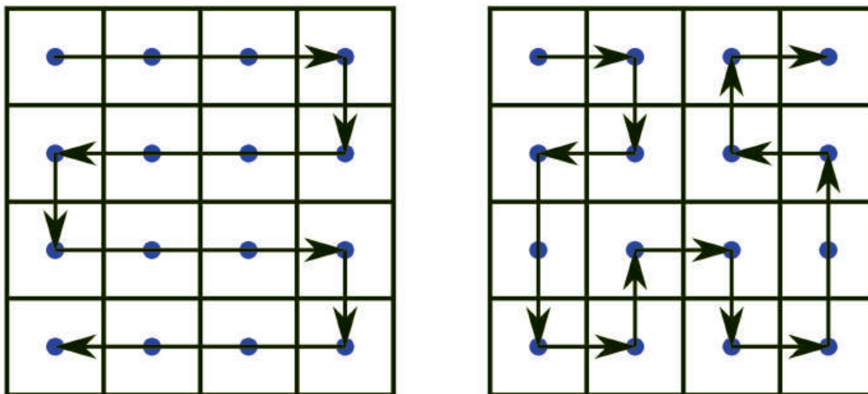

FIGURE 4.1: Different scanning methods. The blue dots indicate the scanning positions and the black arrows the scanning path. Left, snake scanning. Right, Hilbert scanning of order 2. A Hilbert curve of order N is created recursively by repeating four times the same pattern of order N-1. No flyback delay is needed unlike the raster scanning.

4.2.1 Snake scanning

A snake pattern changes the scan direction after every line as in Figure 4.1 (left) and eliminates the flyback motion. It can potentially improve probe instabilities while maintaining a constant speed in each scan line. As no flyback delays are applied, the acquisition time would be also reduced and no extra dose other than for imaging would be applied to the sample. This pattern has already been explored in STEM [45]; however a more quantitative evaluation is given here.

4.2.2 Hilbert scanning

The Hilbert scanning has been proposed previously as a rectangular pattern in scanning analytical instruments [86, 87], as an alternative to the raster method. This scanning method changes the direction of the scanning every one or two steps, resulting in only small jumps during scanning, eliminating the slow scan direction and making the path more isotropic, while each point is still scanned exactly once as in the raster method. A Hilbert pattern of order 2 is illustrated in Figure 4.1, right. Although an even more isotropic path could be

generated by a random scan, the time response of the current microscopes' built-in scanning system, amplifiers, detectors, and the longer step displacement of the probe in this mode would make this option not feasible for STEM imaging [84].

A Hilbert space filling curve of order N subdivides a square grid in 4^N sub-squares and it is created recursively by repeating four times the same pattern of order N-1 [83], for this reason only frame sizes with equal dimensions of a power of 2 are feasible. This is not an important restriction as these are very common dimensions in STEM imaging.

4.3 Experimental evaluation on a single crystal test sample

The experiments were carried out on a probe aberration corrected Thermo Fisher Scientific TITAN^3 microscope, operated at 300 kV, with 50 pA of beam current and a spatial resolution of approximately 0.8 Å. The experiments were performed on a strain-free reference sample of STO in [001] zone axis orientation.

Using the three scanning methods, HAADF images were acquired with the same pixel size, 12.6 pm, with a frame size of 1024×1024 pixels. A series of images were acquired at 2, 4, 7, 8, 9, 10, 12, 15 and 20 μs dwell time, representative of most experimental STEM imaging conditions. The entire experiment was done over the same area of the sample with the Sr sublattice (010) planes oriented close to the fast scan direction and the (100) planes oriented close to the slow scan direction. Only for the raster scanning a flyback delay was necessary. The delay was set to 1 ms, which worked well for all the raster images acquired at different dwell times. This delay added an extra dose and acquisition time per image of approximately 1 s.

In Figure 4.2, experimental images acquired at 15 μs dwell time are shown. Figure 4.2.a1 was acquired with raster scanning, the diffractogram shows vertical streaks in the slow scan direction as a manifestation of non-periodic distortions that arise from drift of the sample or scan instabilities. In combination with the periodicity of the line by line scanning results in modulation streaks in the slow scan direction. The dephasing (shifting) between the individual fast scan lines can be understood as a random shifting of the lines in the image depending on their vertical scan position. Figure 4.2.b1 was acquired with snake scanning, in addition to the vertical streaks, the diffractogram shows extra spots present on top of the streaks. The extra spots are the result of the distortions induced by the horizontal line shifting which, compared to the raster scanning, is no longer purely random. Every scan line will have phase continuity at the left or right hand side of the image [40]. This causes the modulation streaks to have correlation peaks at Nyquist frequency in the slow scan direction. Figure 4.2.c1 was acquired with Hilbert scanning, vertical streaks are absent in the diffractogram and only some extra spots at high frequency are visible in the vertical and horizontal direction. Here, the scanning direction of the probe is changed every few steps, creating a shift between two parallel short scan lines, similar to the snake scanning

case. The short scan lines can be oriented in the vertical or horizontal direction, introducing the extra spots, but now far less obvious compared to the snake scanning case due to the irregular pattern.

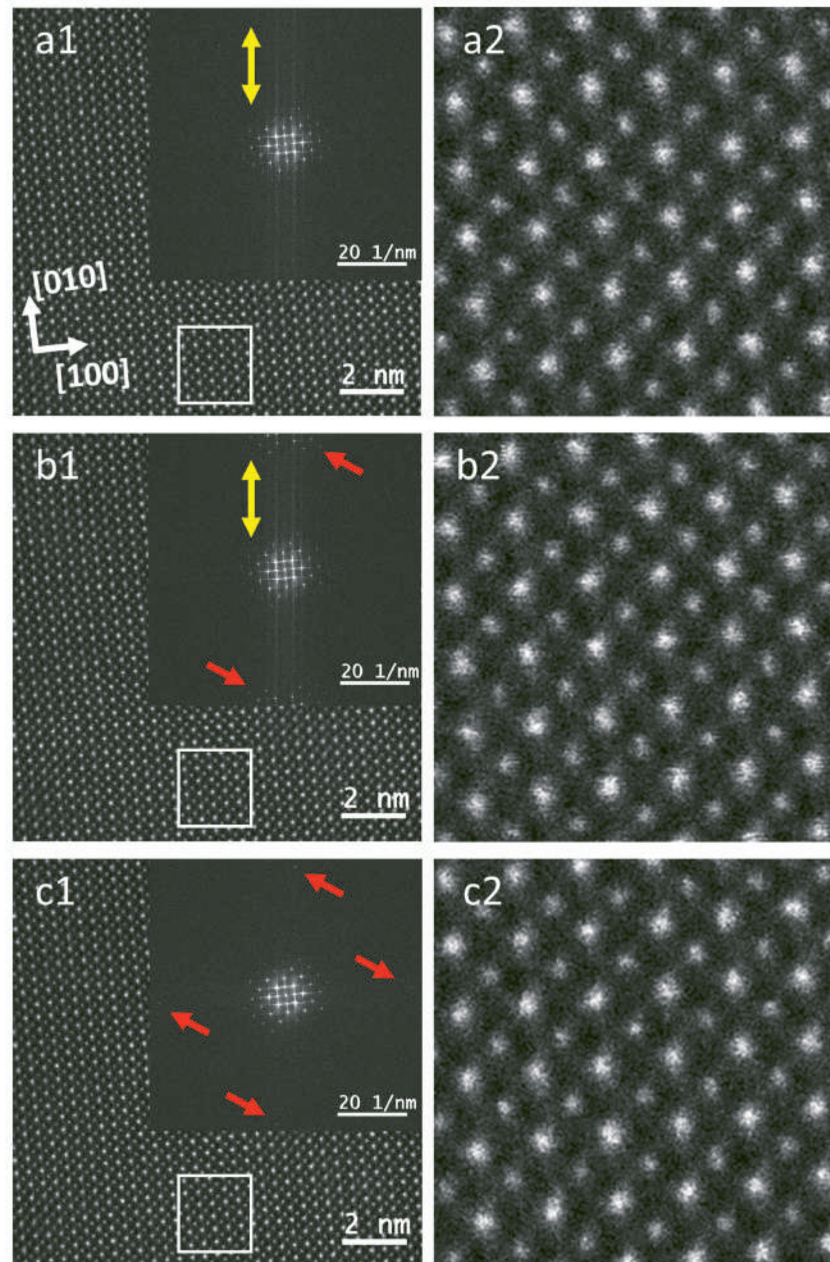

FIGURE 4.2: Experimental HAADF images acquired at 15 μs dwell time, total scan time 15.7 s. a1. Image acquired with raster scanning. The diffractogram in the inset shows vertical streaks, indicated by yellow double arrows, which are manifestations of drift or random external influences between scan lines. b1. Image acquired with snake scanning. In addition to the vertical streaks, the diffractogram shows extra spots, indicated by red single arrows, forming a replica of the central frequencies at Nyquist. The extra spots are the result of the periodic distortions between scan lines with periodicity of 2 pixels. c1. Image acquired with Hilbert scanning. Vertical streaks are not present in the diffractogram. Weak extra spots in the horizontal and vertical direction are the result of the inversion of the scanning direction after a short number of steps, creating a shift between two short horizontal or vertical scan lines. a2, b2 and c2 are highlighted areas in a1, b1 and c1, respectively.

4.3.1 Scanning distortions correction

Implied in chapter 2, the observed shifts can be explained predominantly by a time delay between commanding the scan generator to go to a new position and the reading of the HAADF input signal, the settling time effect on probe positioning and bandwidth limitations in the detector amplifier. Any delay or the settling time effect on probe positioning and possibly detector signal is less visible in raster scanning as it simply shifts the whole image. In snake scanning, this effect is more noticeable because a similar shift but now with reversed direction for odd and even rows is generated. In Hilbert scanning, the settling time effect is most critical as the scan direction is regularly changing.

We model the observed response between target scan positions and the actual probe positions by a narrow Gaussian function which lags in time as:

$$h(t) = e^{((t-t_d)^2)/\sigma^2} \tag{4.1}$$

with t_d representing the time delay of the entire setup and with σ chosen constant with a value of $\sigma = 1/8 \times t_{dwell}$ resembling the sharpness of an ideal impulse response. The tails of the Gaussian function provide some interpolation with the neighbouring time points. Choosing σ too high would result in too much interpolation and would add unrealistic smoothing to the scan path. Convolving the x and y scan signals with this impulse response function allow us to estimate the actual probe position from the target positions:

$$x(t) = x_{target(t)} * h(t);\ y(t) = y_{target(t)} * h(t) \tag{4.2}$$

where * denotes convolution. We optimised t_d in order to minimize the undesired reflections in the diffractogram for each experiment, indicated by the fading of the intensities (with respect to the background) of the extra spots at high frequency.

The corrections show an increasing time lag of the scan system and detector when the dwell time becomes shorter, with a correction going from a fraction of the dwell time to almost three times the dwell time, Table 4.1.

We use the estimated probe positions to correct the experimental images by using a linear interpolation to calculate the image intensities corresponding to the intended rectangular target pixel grid. The calculated diffractograms of the snake and Hilbert acquired images (at 15 μs dwell time) and the diffractograms corresponding to the corrected images are shown in Figure 4.3. Most of the extra spots at high frequencies disappeared; however, for the snake scanning the vertical streaks remain.

Before looking at the quantification of image distortions we focus again on the calculated diffractograms (Fourier transform, FT) of the images as these contain important information about distortions and offer an intuitive way to describe them. As shown in the calculated FTs of the images acquired with the different scanning methods, insets in Figure

TABLE 4.1: Time delays applied to correct images acquired with the snake amd the Hilbert methods.

Dwell time/pixel (μs)	Time delay (t_d) snake scanning (μs)	Time delay (t_d) Hilbert scanning (μs)
2	5.00	5.95
4	5.70	7.92
7	6.72	13.50
8	7.42	15.26
9	8.32	17.20
10	8.91	18.45
12	10.78	12.10
15	13.30	14.70
20	17.29	18.43

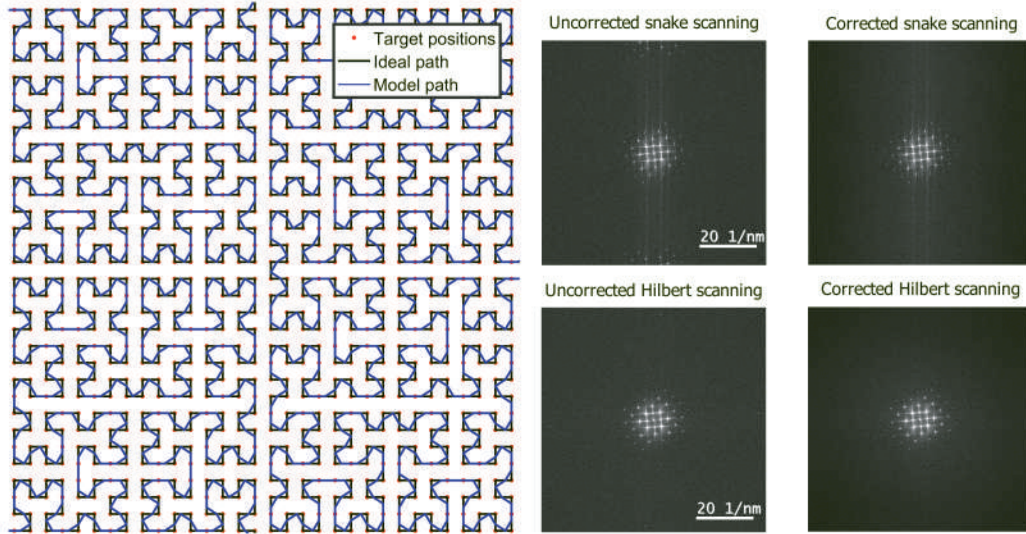

FIGURE 4.3: Left, target positions, ideal path and the model path representing the average position from where the input signal of a given scan point originated. The model only considers a time delay that was optimised to limit the artefacts on the scanned images. Right, raw diffractograms from Figure 4.2 and the diffractograms after the correction.

4.2.a1, b1 and c1, cross like features are identified over the spots that represent the spatial frequencies corresponding to the lattice. Commonly those features are associated with edge effects of the FT. To avoid those effects being mistaken as or associated with scanning distortions, before calculating the FT, a circular window with Gaussian smoothed edges (σ = 10 pixels) was applied to the images acquired at 15 μs dwell time. The calculated FTs in Figure 4.4.a and b correspond to the images acquired with the raster and snake scanning method, respectively, after applying a circular window. The horizontal streaks over the

spots of the FTs disappeared which was not the case for the vertical streaks. The FT in Figure 4.4.c corresponds to the image acquired with the Hilbert scanning method, contrary to the previous two cases, applying a circular window removed both horizontal and vertical streaks around the spots of the FT.

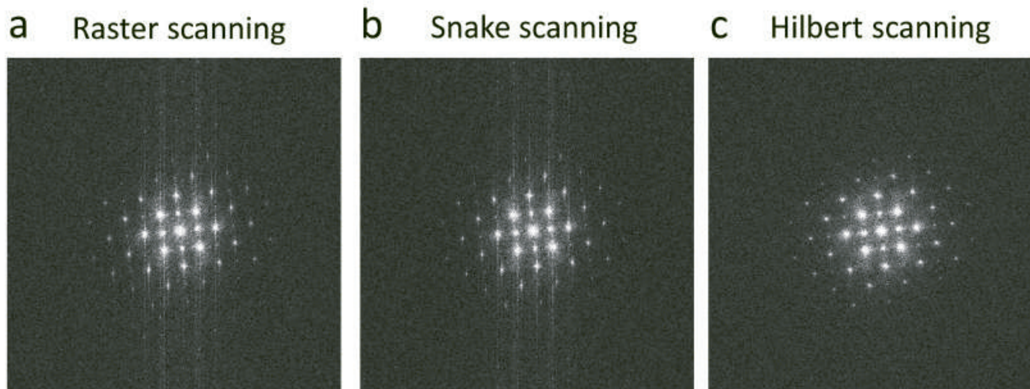

FIGURE 4.4: a, b and c, calculated FTs of the images acquired at a dwell time of 15 μs with the raster, snake and Hilbert scanning methods, respectively. A circular window with smooth edges was applied to the corresponding images to reduce edge effects in the FT. Spots in the FT of the same images without applying the circular window, shown in the insets of Figure 4.2.a1, b1 and c1, present cross like features. Note the absence of streaks in the Hilbert case.

Distortions in terms of atomic column shape and lattice parameter were quantified to compare the different scanning methods as we will see in the next sections.

To compare and quantify the distortions when scanning with the different methods, the images were processed with the help of the Atomap software [88]. First distortions in terms of atomic column shape were quantified, followed by a study of observed lattice distortions.

4.3.2 High frequency content evaluation

Two dimensional (2-D) Gaussian functions were fitted to the atomic columns of the Sr sublattice to estimate their positions (the images were processed with the Atomap software. More information on how this is calculated can be found in the work reported by M. Nord et al. [88]). The region around the atomic columns was masked and for each of the masked images the center of mass of every row was calculated. The centers of mass were compared to a linear fitting (to account for drift, misalignment, or anything that would cause the atoms to deviate from a circularly symmetric intensity pattern) and the standard deviation from this line was calculated to represent the local distortions in the slow scan direction[1]. The same procedure was applied to the centers of mass of the columns on the masked images to represent the distortions in the fast scan direction. The RMS of both the standard deviations in the fast and slow scan direction corresponding to every atomic column, σ_{RMSx} and σ_{RMSy} respectively, were calculated. The same methodology was applied to every image acquired with the different scanning methods at different dwell times. These deviations represent the high frequency noise content as this noise is commonly measured from lines profiles along lattice planes [34].

The results for the raw and corrected data are shown in Figure 4.5. Scanning with the snake method generates more deviations in the y direction (slow scan direction). The data from the snake corrected images shows a reduction of the distortions in the y direction. However, a reduction of the distortions in the x direction is also present as the interpolation method inherently smooths the data. The Hilbert scanning method generates more symmetric deviations. For acquisitions with dwell time longer than 4 μs, the deviations in the y direction are smaller compared with the raster scanning method. For the uncorrected Hilbert scanning data, compared to raster scanning, a reduction of the deviations in the y direction of up to 21.5% was achieved while the deviations in the x direction are higher with an increase of up to 21%. The lowest deviation produced when scanning with the Hilbert method can be identified as the data point closer to the origin, which was at 10 μs dwell time. For the corrected Hilbert scanning data, a significant reduction of the deviations in x and y direction show that the time lag correction is very important here. Compared to the raster scanning data, now the deviations in the y direction are smaller for all the dwell times. The total deviations, calculated as the RMS of σ_{RMSx} and σ_{RMSy}, for all the scanning conditions and their corrections are given in Table 4.2. The total deviation corresponding to the corrected Hilbert data is less than the total deviation calculated for all the other cases. This shows that as far as the image of the atomic columns/atoms is concerned, Hilbert scanning provides clear benefits in terms of scan distortions and equal treatment of both

[1]For the software implementation of this algorithm, see `https://atomap.org/quantify_scan_distortions`

scan directions without requiring e.g. a double acquisition with 90° rotated scan direction as mentioned in chapter 2.

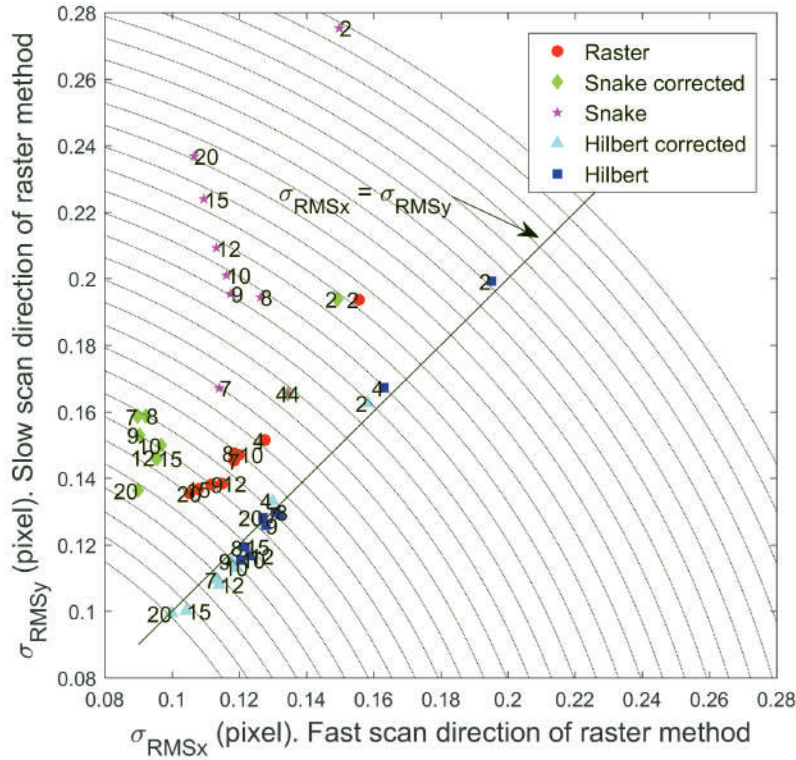

FIGURE 4.5: Standard deviation of the location of the center of mass in intensity profiles through atomic columns. The deviations are calculated in both scan directions, for the different scanning methods and dwell times. Dwell times, in μs, are indicated by the numbers next to each data point. The dotted curves correspond to circles of constant RMS deviation in both x and y directions: cte = $\sqrt{(\sigma^2_{\text{RMSx}} + \sigma^2_{\text{RMSy}})}$.

TABLE 4.2: Combined standard deviation of the center of mass location in intensity profiles through atomic columns in both x and y direction, obtained with different scanning methods and dwell times for a total of 966 atomic columns per image.

Dwell time/pixel (μs)	Raster scanning σ_{RMS} (pixel)	Snake scanning corrected σ_{RMS} (pixel)	Snake scanning σ_{RMS} (pixel)	Hilbert scanning corrected σ_{RMS} (pixel)	Hilbert scanning σ_{RMS} (pixel)
2	0.176 ± 0.002	0.173 ± 0.002	0.222 ± 0.003	0.160 ± 0.002	0.197 ± 0.002
4	0.140 ± 0.001	0.151 ± 0.002	0.151 ± 0.002	0.132 ± 0.001	0.165 ± 0.002
7	0.133 ± 0.001	0.129 ± 0.002	0.143 ± 0.002	0.111 ± 0.001	0.131 ± 0.001
8	0.134 ± 0.001	0.130 ± 0.002	0.164 ± 0.002	0.120 ± 0.001	0.130 ± 0.001
9	0.126 ± 0.001	0.126 ± 0.002	0.161 ± 0.002	0.116 ± 0.001	0.127 ± 0.001
10	0.134 ± 0.001	0.126 ± 0.001	0.164 ± 0.002	0.116 ± 0.001	0.118 ± 0.001
12	0.127 ± 0.001	0.123 ± 0.001	0.168 ± 0.002	0.111 ± 0.001	0.120 ± 0.001
15	0.123 ± 0.001	0.123 ± 0.001	0.176 ± 0.002	0.102 ± 0.001	0.121 ± 0.001
20	0.121 ± 0.001	0.115 ± 0.001	0.184 ± 0.002	0.100 ± 0.001	0.128 ± 0.001

4.3.3 Lattice parameter evaluation

Image distortions in the slow scan direction are clearly reduced when using Hilbert scanning, as vertical streaks in the diffractograms were not apparent. However, drift of the sample/stage is still present and results in abrupt discontinuities in the image at boundaries that were acquired with a long time difference, Figure 4.6. The fact that these boundaries are fixed and known allows the experimenter to reject them during analysis. Rather than a line modulation as in raster and snake scanning, the modulation due to sample drift is now smeared over the image with approximately equal weight in all directions, leading to a better behaviour when calculating the diffractogram.

Atomic resolution images contain direct information about strain, which can be very relevant in many material systems [89]. STEM images are however often problematic for this application as the sequential scanning mixes actual strain with artefacts during the recording time. Strain mapping techniques offers the possibility to quantify these distortions [90, 31, 91, 29], in order to verify the role of the scan strategy for this application we applied a strain mapping technique based on real space analysis. Deviations in the interplanar spacing of the Sr sublattice were calculated with the Atomap software. Because of the orientation of the sample with respect to the raster scanning directions, measuring the interatomic distances of the (010) planes will quantify the distortions generated in the slow scan direction and the interatomic distances of the (100) planes will quantify the distortions generated in the fast scan direction. Figure 4.7 shows the interplanar spacing maps for images acquired with the raster, snake and Hilbert scanning at 9 μs dwell time. As the shape of the atomic columns does not significantly influence the interplanar spacing of the sublattices, we employed the corrected snake and Hilbert images instead of the uncorrected images.

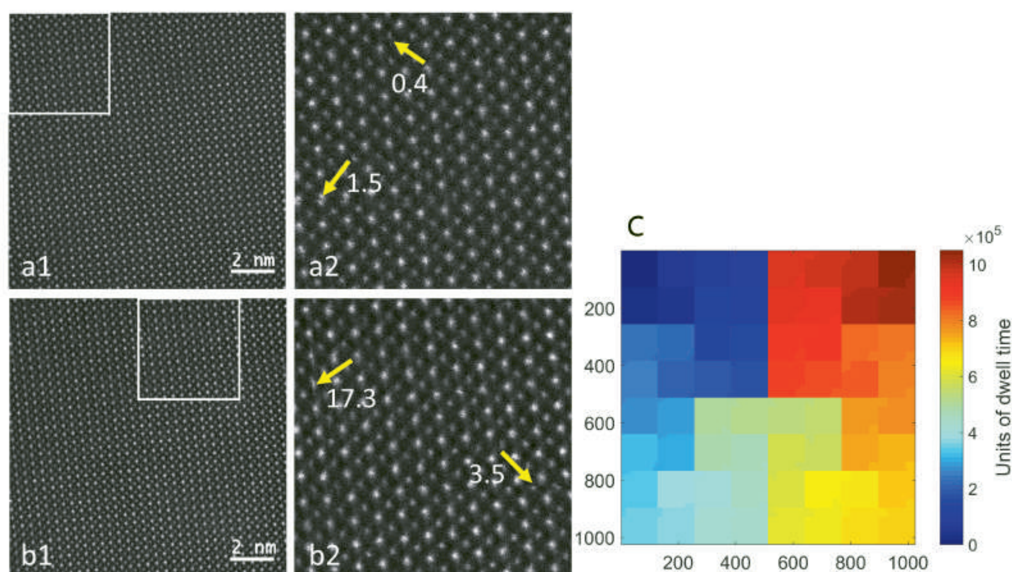

FIGURE 4.6: Experimental HAADF images acquired with Hilbert scanning. a1. Image acquired at 7 μs dwell time, total scan time 7.3 s. b1. Image acquired at 20 μs dwell time, total scan time 21 s. The highlighted areas in a1 and b1 are shown in a2 and b2, respectively. Yellow arrows indicate abrupt discontinuities in the images caused by the interplay between sample drift and the scan pattern. The number noted next to the arrows indicates the time difference (in seconds) across the artefact boundary. c. Acquisition time map of each pixel following the Hilbert scanning sequence.

The interplanar spacing maps of the (010) planes calculated from the images acquired with the raster and snake methods, Figures 4.7.a1 and 4.7.b1, respectively, show horizontal bands commonly found because of drift leading to distortions in the slow scan direction. For the Hilbert case, the map is more homogeneous, Figure 4.7.c1. No bands are present in the corresponding maps of the (100) planes.

The standard deviation of the interplanar spacing maps as a function of dwell time is shown in Figure 4.8. The results from the snake and Hilbert uncorrected and corrected images are included. Only slight differences between the results of the uncorrected and corrected data were found as there is not a substantial influence of the high frequencies distortions on the interplanar spacing. It can be seen that scanning with the Hilbert method at high speed acquisitions, 2 μs dwell time, generates more distortions than at slower speeds (these distortions were reduced for the corrected Hilbert images). As explained before, the continuous change of the scanning direction prevents the probe to reach a constant speed during the entire scanning path which is not the case for the raster scanning. At longer dwell times, when scanning with the Hilbert method the distortions become approximately constant for both scanning directions, while for the raster and snake methods the distortion first decrease and then keep increasing for the slow scan direction and first decreases and then becomes constant for the fast scan direction. This behaviour can be explained as follows. For very short dwell times, distortions occur due to the finite settling time of the

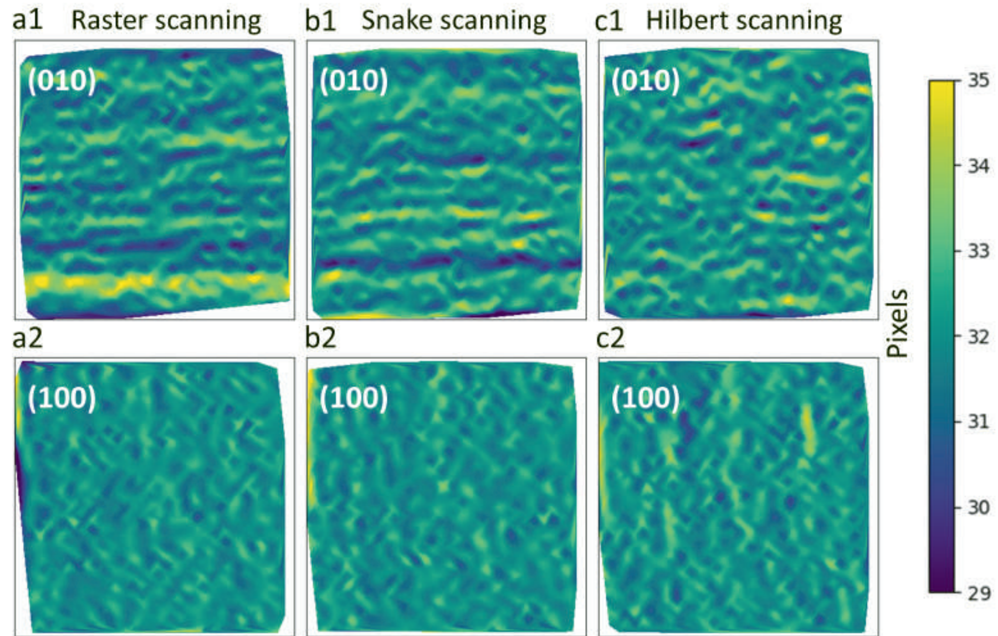

FIGURE 4.7: Interplanar spacing (010) and (100) maps of the Sr sublattice calculated from images acquired at 9 μs dwell time, for the three different scanning patterns. Sr sublattice (010) planes oriented close to the fast scan direction and the (100) planes oriented close to the slow scan direction.

probe on the sample. This occurs in this instrument and at the given magnification up to approximately 2 μs. Increasing the dwell time results in the disappearing of such artefacts, but now slow drift variations come into play that become more apparent with higher dwell times. This effect of drift depends strongly on the scan pattern and is low in the fast scan directions for raster and snake scanning, while it is high for the slow scan direction. In Hilbert scanning, there is no slow and fast axis and here the standard deviation is equally distributed in both directions with higher deviations for higher dwell times. The total deviations, calculated as the combined standard deviation of the interplanar spacing maps, for the (010) and (100) planes, for the scanning methods after the correction are given in Table 4.3. The RMS of the standard deviations and the mean Sr interplanar spacing for the raster and corrected Hilbert scanning data are comparable, Figure 4.8.c.

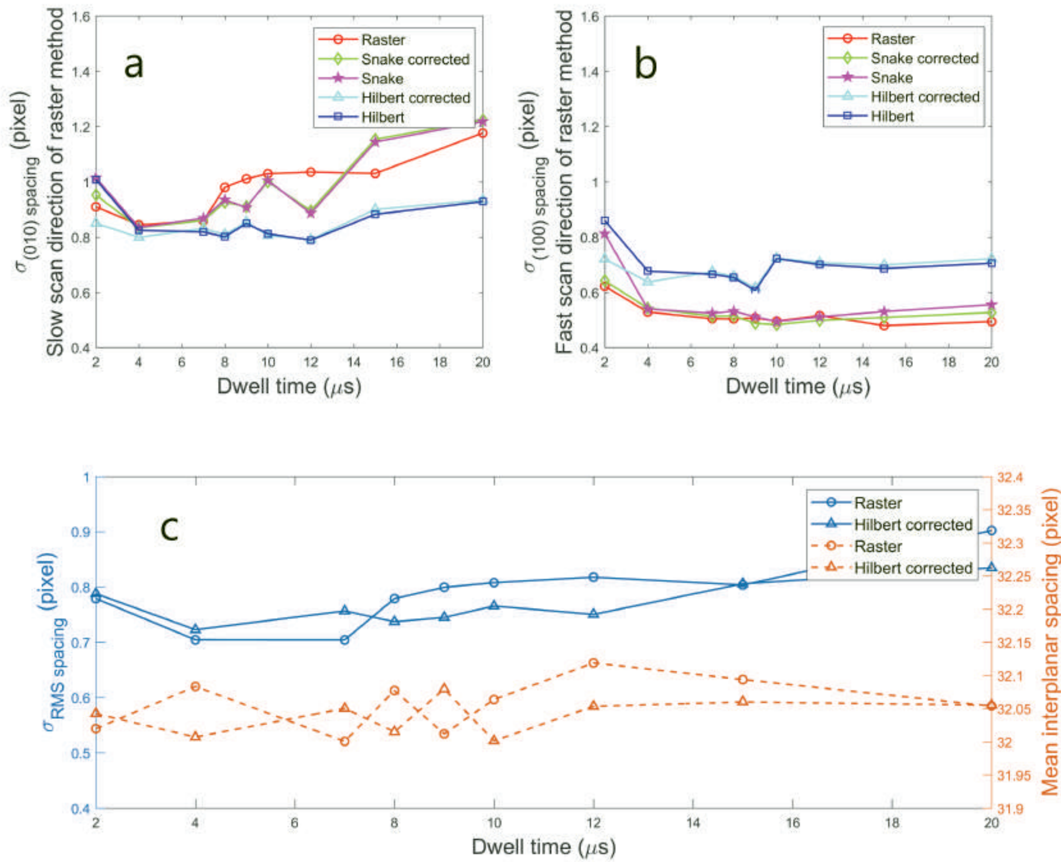

FIGURE 4.8: Standard deviations calculated from the interplanar spacing maps on Figure 4.7. a. Standard deviations from the (010) planes. b. Standard deviations from the (100) planes. c. RMS of the standard deviations and the mean interplanar spacing, calculated from the results in x and y directions, at different dwell times. This shows that Hilbert and raster scanning provide similar total standard deviations of the lattice spacing with no apparent bias for equal dwell times.

TABLE 4.3: Combined standard deviation of the interplanar spacing maps, for the (010) and (100) planes, obtained with different scanning methods and dwell times. Only the data after the correction is shown here.

Dwell time/pixel (μs)	Raster scanning σ_{RMS} (pixel)	Snake scanning σ_{RMS} (pixel)	Hilbert scanning σ_{RMS} (pixel)
2	0.779 ± 0.026	0.812 ± 0.027	0.788 ± 0.026
4	0.704 ± 0.023	0.704 ± 0.023	0.723 ± 0.024
7	0.704 ± 0.023	0.708 ± 0.023	0.756 ± 0.025
8	0.779 ± 0.026	0.749 ± 0.025	0.737 ± 0.024
9	0.799 ± 0.026	0.730 ± 0.024	0.745 ± 0.024
10	0.808 ± 0.026	0.785 ± 0.026	0.766 ± 0.025
12	0.818 ± 0.027	0.725 ± 0.024	0.750 ± 0.025
15	0.803 ± 0.026	0.892 ± 0.029	0.806 ± 0.026
20	0.902 ± 0.030	0.941 ± 0.031	0.835 ± 0.027

4.4 Discussion

Comparing the different scan regimes resulted in a few general observations. When it comes to the local high frequency information in an image, e.g. the shape of the atomic columns, we find that both raster and snake scanning introduce significant anisotropy because of the difference in fast and slow scan directions. This results in the presence of streaks in the diffractograms of the images. These streaks can be understood as a slow modulation affecting the different scan lines, and is caused by sample or probe drift on the sample. This issue can be alleviated with Hilbert scanning which shows a reduced total standard deviation around a localised feature with isotropic behaviour in both directions. This results in a much 'cleaner' diffractogram where the streak features are completely absent. In the image however, specific abrupt features appear along lines where pixels that are scanned with large time interval meet.

Regarding strain mapping, for the Hilbert scan, the distortion effect due to drift is also more isotropic while the total precision of the strain measurement depends entirely on the amount of drift and the total acquisition time as long as very short acquisition times are avoided. The total standard deviation caused by drift could be interpreted as an 'errorbudget' that is more equally distributed over x and y direction for Hilbert scanning as opposed to the two other scan methods.

There are however two important benefits in doing a single Hilbert scan as compared to two orthogonal raster or snake scans.

- Single scan is faster and requires a lower dose, which might be essential for beam sensitive samples.
- A single scan containing correct information about x and y strain allows to correctly calculate the relation between both strain directions which is important for e.g. shear

strain. This is more difficult for raster scanning as it requires combining low noise x and y strain maps from two different images.

The Hilbert space filling curve of order n subdivides a square grid in 4^n sub-squares, for this reason only frame sizes with equal dimensions of a power of 2 are feasible but as these are very common dimensions in raster scanning too, this is not an important restriction.

4.5 Conclusions

The proposed Hilbert method shows a reduced total standard deviation around a localised feature with isotropic behaviour in x and y directions.

The distortion effect due to drift is also more isotropic while the total precision of the strain measurement depends entirely on the amount of drift and the total acquisition time. The total standard deviation caused by drift in terms of strain mapping is nearly independent of the scan method.

In terms of dose, both snake and Hilbert scanning are preferred as no flyback time is required (hence the acquisition time is reduced as well). The distribution of the dose with the Hilbert method is clearly different than with the raster method. Small neighbouring areas are registered in a shorter time than a line by line scanning, this could have an influence on beam damage as the dose is distributed faster in smaller areas, further experiments on beam sensitive samples could help to clarify these effects. In the field of selective laser sintering, it was shown that the distribution of temperature in the treated object was more uniform when scanning with a Hilbert method compared to a raster method [92].

No post-processing was required to achieve the results other than implementing an experimentally determined time lag representing the finite response of the system.

The method can be implemented on any existing STEM instrument, either by the manufacturer changing the scan engine firmware/hardware or alternatively by the customer adding an external scan engine.

Chapter 5

Scan strategy to address electron beam damage in STEM

The notions regarding the spatial and temporal characteristics of beam damage given in chapter 3, along with the experimental results, allow us to describe the mechanism in terms of a diffusion process as e.g also attempted by D. Nicholls et al. [93].

In STEM, the highly focused electron probe interacts with the sample and the conventional raster scan applies the electron dose to adjacent positions that are scanned consecutively. A damage process that spreads spatially with time, can affect regions of the sample that will be visited by the next probe position. In this way the damage could build up rapidly as regions that come later in the scan will have been affected more by earlier scan points. For similar reasons, scan points with more neighbours will suffer from more damage than positions which have fewer neighbours.

Unlike CTEM where the sample is uniformly irradiated by a parallel beam, in STEM the irradiation is performed locally in a sequence manner. The difference on the distribution of the dose in these two operation modes may influence the damage behaviour when a diffusion-like process is present.

A question results from the possibility of beam damage being related and mediated by a diffusion process, could different scan strategies reduce beam damage while keeping the same image quality and total dose on the sample?

Similar strategies were explored in the field of SEM and low-voltage electron beam lithography (LVEBL) to reduce the undesirable effects of electrostatic charging in insulators [94, 95]. Changing the sequence of the scanning positions in SEM and the sequence of the scanning patterns in LVEBL allowed to counteract the charging effects that otherwise build up when immediately adjacent positions/patterns are scanned/written; taking advantage of the characteristic time decay of electrostatic charging depending on conductivity.

In STEM hyperspectral imaging, A. Zobelli et al. [84] have recently investigated a random scan operation mode in order to reduce beam damage effects. The effect of the scanning pattern was shown in the cathodoluminescence map of hexagonal boron nitride flakes

which exhibited intensity instabilities. The instabilities were suggested to come from variations in the charge state of defect centers, which can be influenced by the accumulation of electrostatic charge in the sample caused by the ejection of secondary electrons. In this sense, raster scanning would generate a fast accumulation of electrostatic charge as adjacent pixels are scanned consecutively. Intensity instabilities were reduced when scanning with a random pattern. However, as stated in the previous chapter, a random scanning would not be feasible in STEM imaging.

In this section we investigate the role of the scan pattern on the damage behaviour of a commercially available zeolite sample with the clear aim to make our observations as reproducible as possible. Damage reduction by this means is reported on this sample. Similar results concerning damage reduction are reported for the porous Cu-compound sample described in chapter 3.

5.1 Interleaving pattern

We propose an alternative interleaved scan pattern, sketched in Figure 5.1. The pattern skips pixels regularly in both scan directions (allowing a constant speed) until the full frame is scanned, alternatively, the interleaving sequence can be done in a single scan direction. The scanning is done without any interruption which allows achieving the same acquisition time (and hence dose) than for the conventional raster method with the same spatial resolution. The maximum number of pixels that are skipped in each scanning direction is limited by the dynamic performance of the scan system where magnification and dwell time play a decisive role as they determine the settling time of the probe to within an acceptable region from the new probe position. More importantly, the number of pixels to skip would be dictated by the diffusion parameter that governs the beam damage process. We attempt to make the distance between consecutively visited sample positions such as to ensure that a newly visited position is not yet influenced by the diffusing effect from the previous one. This makes finding an optimal alternative scanning pattern a non-trivial problem and likely dependent on the sample characteristics.

The external hardware described in the previous chapter was employed to control the probe positioning.

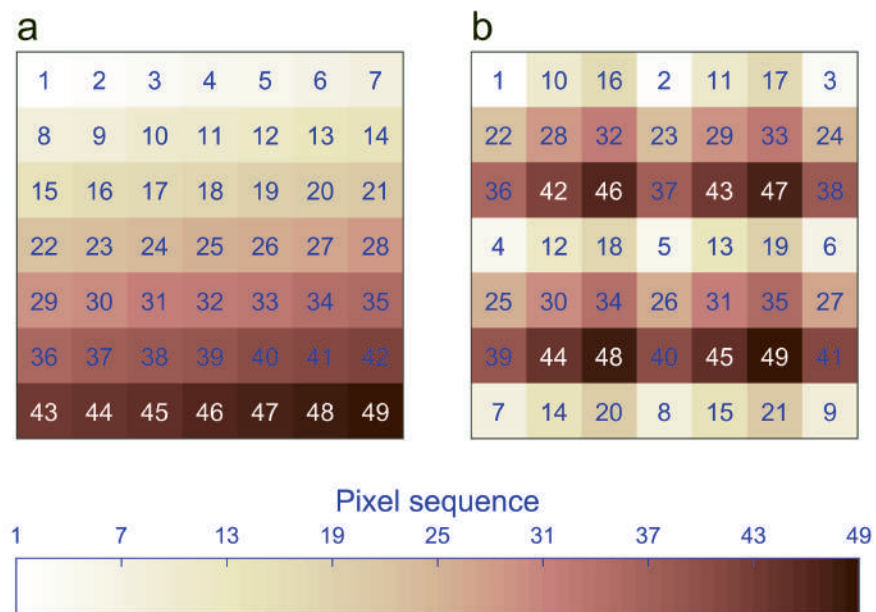

FIGURE 5.1: Different scanning patterns for a 7×7 pixels frame. The numbers and color scale indicate the order of the scanning positions. a. Conventional raster scanning sequence. b. Interleaved scanning sequence, skipping two pixels in each scan direction. The total electron dose is the same in both cases; however, the temporal distribution of the dose is different. Note that the actual number of sampled points is far higher as displayed in this sketch, but the pattern is analogous.

5.2 Experimental findings on electron beam sensitive samples

Zeolite sample

We compare the proposed interleaved scanning with the raster method in terms of damage behaviour on a beam sensitive commercial zeolite sample.

Zeolites are considered a highly relevant class of microporous[1] materials for their industrial applications such as in catalysis, ion exchanging, molecular sieving, etc. [97, 98]. These are crystalline microporous aluminosilicates with three dimensional network structures that have SiO_4 and AlO_4 tetrahedra[2] as building units that are connected by sharing oxigens, Figure 5.2. The tetrahedra are arranged forming cages that are considered as the secondary building units, Figure 5.2. The framework structure depends on the combination of the tetrahedra, and the properties of zeolites rely on these structures.

Unfortunately atomic local analysis of zeolites with (S)TEM has been difficult because of its poor stability under the electron beam [100, 101]. Radiolysis is considered to be the dominant mechanism of damage in zeolites, either by the direct interaction of the primary beam with the framework structure resulting in the bond breakage of the oxygen bridges or by the damaging radicals created from the radiolysis of water contained in the structure, as deduced by the dependence of the damage rate on the degree of hydration [99, 102, 103]. The Si/Al ratio is another factor related to the sensitivity of the zeolite upon electron irradiation, a zeolite with a high Si/Al ratio (a Si-rich zeolite) shows more tolerance to the electron irradiation than a zeolite with a low Si/Al ratio [100, 99, 102].

Taking special care on the employed dose and assisted by a direct phase imaging technique (such as integrated differential phase contrast or iDPC [104, 105]), relatively recent works have already demonstrated the possibility to acquire atomic resolution STEM images before severe damage takes place [106, 107].

Although standard methods to synthesize these materials do exist [108], the use of self-prepared samples adds more variables to control in the experiments. Here, we deliberately opt for a commercially available sample as it enables others to repeat and reproduce our experiments. This way we avoid the all-too-often circumstantial evidence that seems to surround the topic of beam damage in TEM and hinders progress in this important domain.

The experiments were carried out on a commercial Linde Type A (LTA) zeolite sample (calcium exchanged sodium aluminium silicate, Sigma Aldrich BCR-705), which is among the most beam sensitive zeolites, Si/Al = 1. In Figure 5.2 a model representing the LTA structure is shown. The large cage, unit cell, corresponds to the alpha cage and the smaller

[1]Microporous materials are classified as materials containing pores of sizes below 2 nm, according to the IUPAC [96].

[2]The aluminum and silicon atoms are located at the so-called crystallographic T-sites which are tetrahedrally coordinated by four oxygen atoms [99].

one corresponds to the sodalite cage [106]. The sample was crushed in a mortar for 5 min, dispersed in ethanol and drop casted on a holey carbon TEM grid.

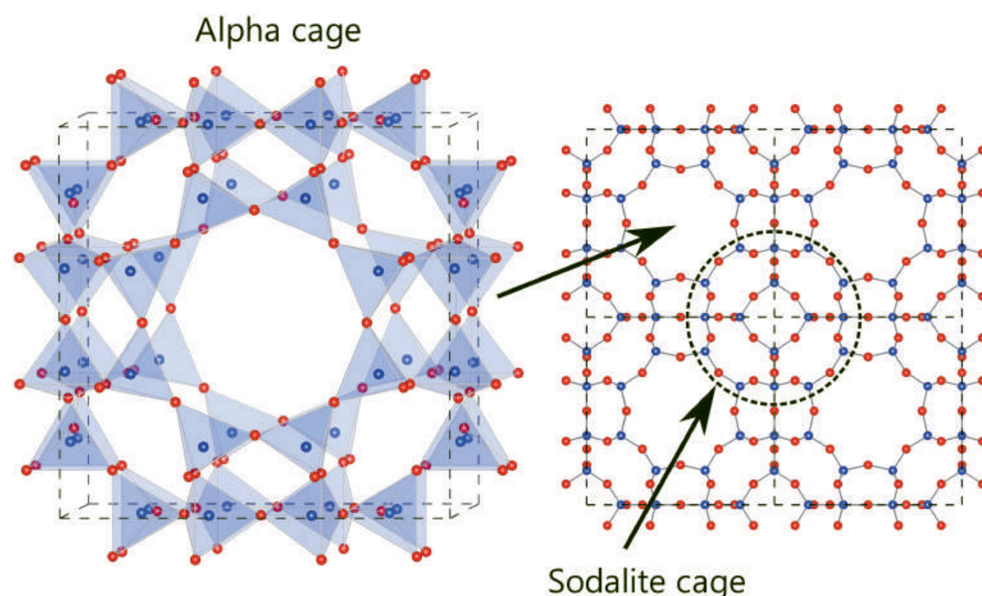

FIGURE 5.2: Framework structure corresponding to a Linde Type A (LTA) zeolite. Red spheres represent oxygen (O) atoms and blue spheres silicon/aluminum (Si/Al) atoms. Left, Alpha cage (unit cell indicated by the dashed line) formed by SiO_4 and AlO_4 tetrahedra, slightly tilted from [001] projection. Right, structure along the [001] crystallographic orientation. Sodalite cage is shown in the centre.

The experiments were performed on a probe aberration-corrected Thermo Fisher Scientific TITAN^3 microscope, operated at 300 kV in HAADF-STEM mode, reaching a spatial resolution of approximately 0.8 Å for a beam current of 50 pA (measured from a pico-ammeter connected to the fluscreen).

Using the scan engine described in the previous chapter is another way how we increase the reproducibility of our findings by repeated automated experiments that rule out local variations in sample conditions. Our methodical experiments show that under the same conditions of total electron dose and dose rate, the interleaved scanning systematically reduces electron beam damage compared to the raster scanning.

In order to have similar conditions for all the acquisitions, the raster and interleaved scanning were compared by acquiring high resolution images on areas of thin crystals with uniform thickness showing the same [001] crystallographic orientation. Practically, the flexibility of the scan engine allowed us to acquire raster and interleaved scans within the same image. As shown in Figure 5.3, single experiments consisted in scanning 3×3 sub-images continuously from top to bottom and from left to right, alternating the raster and interleaved scanning. All the sub-images or scanned areas, consisting of a frame size

of 512 × 512 pixels, were scanned with the same pixel size and dwell time. To avoid any pre-damage coming from earlier scanned sub-areas, these were spaced by a distance of half of the field of view of each area (256 pixels in the present case). The images were acquired without any flyback delay to remove extra source of damage.

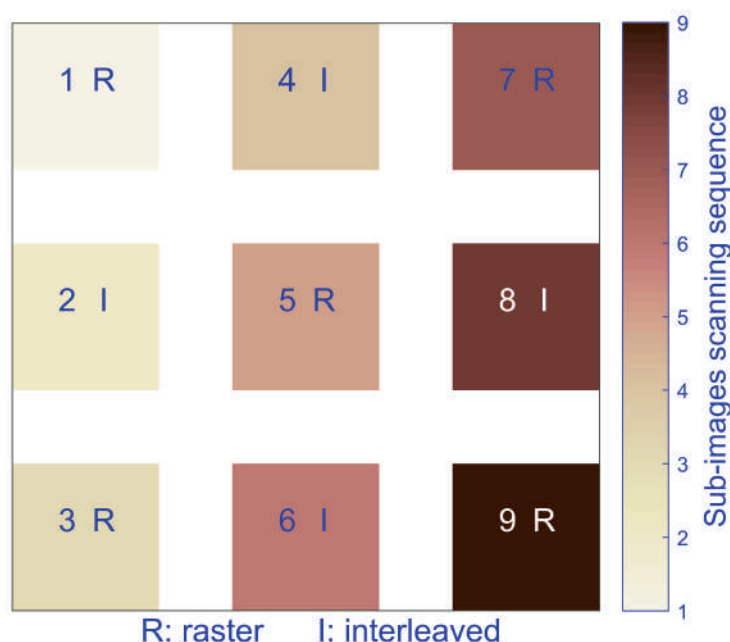

FIGURE 5.3: 3 × 3 sub-images experiment performed on areas of interest of thin zeolite crystals. The numbers indicate the sequence of the squared scanned areas. The areas were scanned with either the raster (R) or interleaved (I) scanning pattern. The space between the scanned areas in the vertical and horizontal direction is half of the size of the scanned areas.

To avoid any beam damage from the static probe, first an area of interest was found scanning at low magnification, then the beam was blanked and the scanning was stopped. The experiments were performed at high magnification, allowing high resolution imaging, and the beam was manually unblanked immediately after the start of the first scanning sub-area and blanked before the scanning of the last sub-area finished. For this reason the first and last scanned sub-areas of the experiments, numbered 1 and 9 in Figure 5.3, were disregarded when comparing both scanning methods. Multiple acquisitions over the same area of interest were acquired following the same procedure; the time between consecutive acquisitions was approximately 6 s. Minor sample drift effects were observed during the acquisitions. These well-controlled experimental conditions allowed us to fairly compare both scanning methods.

An instantaneous electron dose rate per pixel can be defined as the electron beam current, expressed in electrons per second, divided by the area of individual pixels. Since for each experiment, the same beam current, pixel size and dwell time were employed, the

electron dose and electron dose rate per pixel were the same, independent of the scanning pattern. The experiments were performed at high resolution with two different pixel sizes, 24.3 pm and 34.4 pm, with corresponding dose rates per pixel of approximately $5.3 \times 10^9 e^- Å^{-2} s^{-1}$ and $2.7 \times 10^9 e^- Å^{-2} s^{-1}$, respectively. The electron dose is calculated directly by dividing the electron beam current by the size of the individual scanned areas of the sub-images experiments and multiplying this value by the time to scan that area.

Figure 5.4 shows two images acquired respectively with the raster and interleaved methods. The images were extracted from a 3×3 sub-image experiment acquired with 24.3 pm pixel size, 6 μs dwell time and a total dose of $3.17 \times 10^4 e^- Å^{-2}$. Both images are comparable in terms of contrast and resolution as can be seen directly from the LTA framework in the HAADF image and the diffractograms; however the diffractogram that corresponds to the image acquired with the interleaved method presents some extra spots at high frequency (indicated by the yellow arrows in Figure 5.4.b2. The extra spots could be the result of sample drift which in combination with the nonconsecutive scanning leads to a periodic modulation which can be corrected as described in the previous chapter. However, this was not applied here since it involves interpolation methods that would unavoidably change the intensity values of the acquired pixels and contrast of the images, hampering objective comparisons. Furthermore, drift was estimated to be negligable as it will be shown later in this chapter. Another reason for these effects can be beam damage itself which is imprinted according to the interleaved pattern. This point will also be discussed later in this chapter. The effects of settling time of the probe can be identified as distortions on the left side of the images, as no flyback delay is applied, see enlarged images of Figures 5.4.a1 and 5.4.b1. The distortions are more pronounced for the interleaved scanning. The dashed squares in Figure 5.4.b1 overlay over 2×2 crystal unit cells, alpha cages; the small cage in the center corresponds to the sodalite cage.

Figures 5.5 and 5.6 show multiple acquisitions extracted from two different 3×3 sub-images experiments performed on different areas of the same crystal. In both cases the scanning was performed with the same pixel size, 24.3 pm, and the same dose rate per pixel, $5.3 \times 10^9 e^- Å^{-2} s^{-1}$. Each figure shows images acquired with the raster and interleaved methods, the images correspond to the areas numbered 5 and 4, respectively, of the experiments (see Figure 5.3). Figure 5.5 corresponds to an experiment carried out scanning at 6 μs dwell time with an electron dose of $3.17 \times 10^4 e^- Å^{-2}$, three consecutive acquisitions were performed for this experiment. Figure 5.6 corresponds to an experiment carried out scanning at 9 μs dwell time with an electron dose of $4.76 \times 10^4 e^- Å^{-2}$, two consecutive acquisitions were performed for this experiment. The total accumulated dose on each scanned area of both experiments is the same, $9.51 \times 10^4 e^- Å^{-2}$. The scanning conditions used to acquire the images shown in Figures 5.5 and 5.6 are summarized in Table 5.1.

As can be seen from Figures 5.5 and 5.6, the HAADF signal changes progressively as the accumulated dose increases, which indicates sample degradation. Loss of mass and

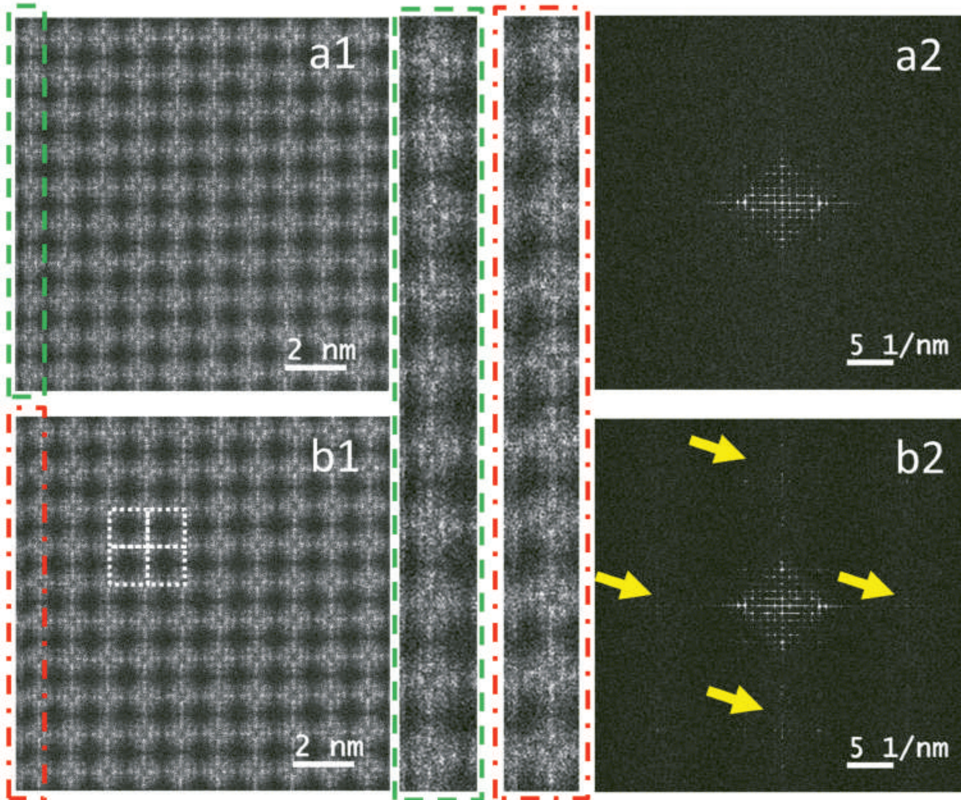

FIGURE 5.4: Images extracted from a 3 × 3 sub-images experiment acquired with 24.3 pm pixel size, 6 μs dwell time and a calculated dose of $3.17 \times 10^4 e^- Å^{-2}$. a1. Image acquired with the raster scanning. b1. Image acquired with the interleaved scanning. Highlighted areas show image distortions on the left side of the images because of the settling time effect of the probe when no flyback delay is applied. The contrast on the raw images was adjusted equally for feature enhancement. a2. Diffactogram calculated from the raster image. b2. Diffractogram calculated from the image acquired with the interleaved scanning. The extra spots indicated by the arrows are the effect of the misaligning scanning lines in the x and y directions.

TABLE 5.1: Scanning conditions used in experiments shown in Figure 5.5 and 5.6.

Experiment	Scanning pattern	Acquisitions	Dwell time (μs)	Pixel size (pm)
Figure 5.5	Raster Interleaved	3 ×	6	24.3
Figure 5.6	Raster Interleaved	2 ×	9	24.3

amorphization can be distinguished as areas that become dark and areas where the framework structure becomes blurred, respectively. These changes are more visible in the central-bottom region of the areas acquired with the raster method while mainly in the central region of the areas acquired with the interleaved method. A clear observation in both experiments is that degradation of the sample is more pronounced when scanning with the

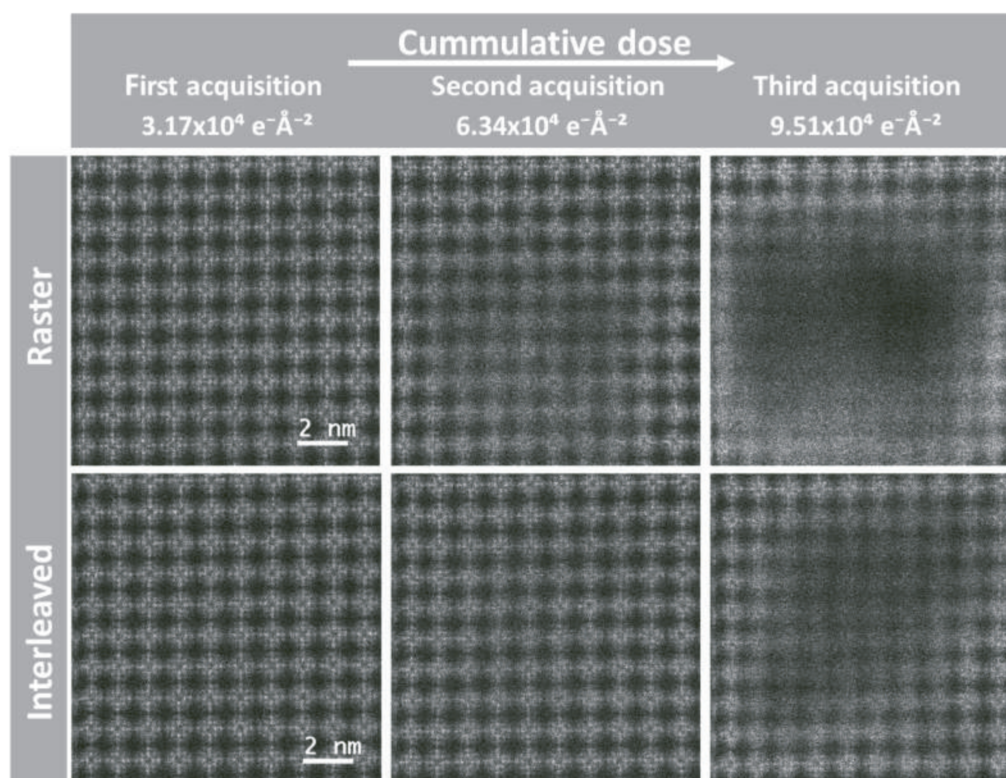

FIGURE 5.5: Sub-images extracted from three consecutive acquisitions over the same 3×3 sub-images experiment. The scanning was performed with 24.3 pm pixel size, 6 μs dwell time and a calculated dose of approximately $3.17 \times 10^4 e^{-} Å^{-2}$ peracquisition. The contrast on the raw images is chosen equal to allow a fair comparison of the evolution under beam damage.

raster method, except for the first acquisitions where the image quality seems to be comparable for both scan types. Moderate beam damage after the first acquisitions is observed, blurring of the sodalite cages to some extent. Deformation of the structure is apparent as a curved framework on the top region of the last acquisition images acquired with both scanning methods. In general, after applying the total electron dose, the experiment performed at 9 μs dwell time presents more damage than the experiment performed at 6 μs dwell time, for both raster and interleaved methods, despite the fact that the total accumulated dose is the same in all four cases.

Figures 5.7 and 5.8 show integrated line profiles from the images in Figures 5.5 and 5.6, respectively. The profiles were extracted from the center of the images, where damage is most apparent, along the black arrows in the figures and considering a width of 256 pixels. The intensities were normalized with respect to the maximum intensity of the integrated line profile corresponding to the first acquisition.

The line profiles in Figure 5.7 correspond to the images acquired with 6 μs dwell time, shown in Figure 5.5. For the first acquisition, the subnanometer scale variations in the

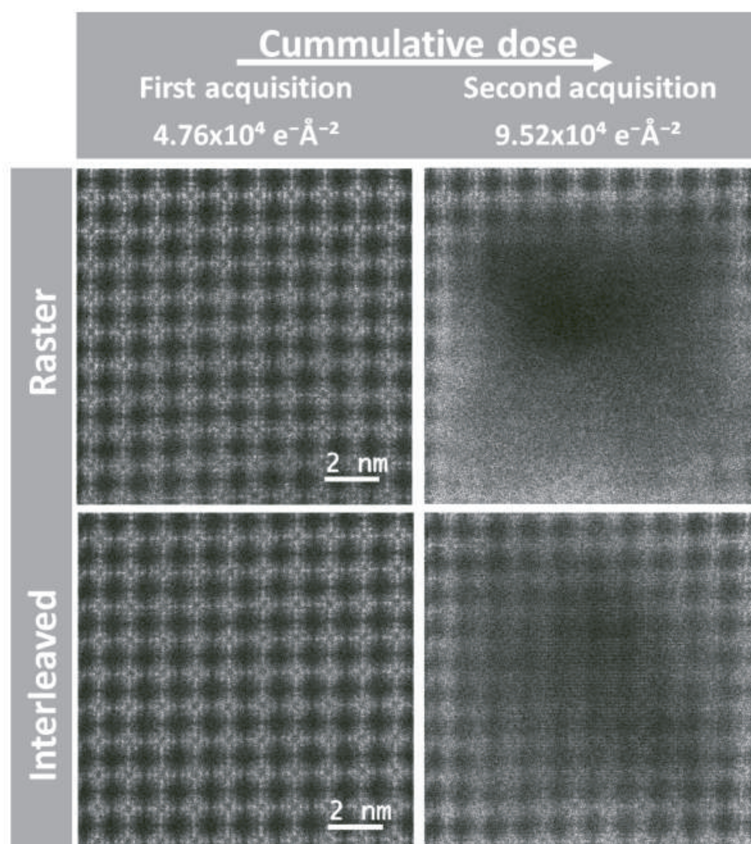

FIGURE 5.6: Sub-images extracted from two consecutive acquisitions over the same 3×3 sub-images experiment. The scanning was performed with 24.3 pm pixel size, 9 μs dwell time and a calculated dose of approximately $4.76 \times 10^4 e^- Å^{-2}$ per acquisition. The contrast on the raw image is chosen equal to allow a fair comparison of the evolution under beam damage.

profile, small peak fluctuations inside the dashed circle in Figure 5.7.a, correspond to variations in the density of atomic columns around the sodalite cages. The larger variations, at nanometer scale, correspond to variations on the density of atomic columns around the unit cells of the framework. The line profiles corresponding to the first acquisition with both scanning methods are quite comparable.

In Figure 5.7.a, second acquisition, the loss of the subnanometer scale variations and the reduced signal amplitude are clearly visible on the central region of the profile, and to a lesser extent on the right region. While the profile from the data acquired with the interleaved scanning, Figure 5.7.b, second acquisition, becomes more noisy without showing a clear reduction of the signal amplitude. In both cases, deformation of the structure is also evident here which is indicated by the shift of the positions of the leftmost peaks with respect to their positions on the first acquisitions. For the third acquisition with the raster method, the nanometer scale variations are completely lost mostly from the center

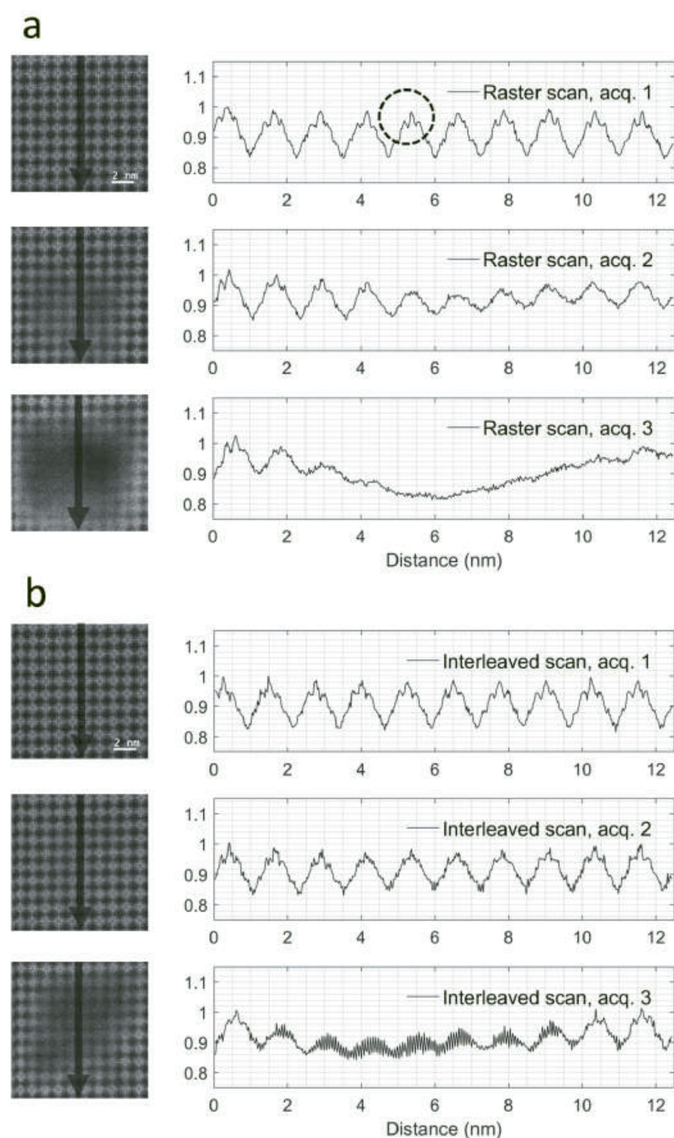

FIGURE 5.7: Integrated line profiles of images in Figure 5.5, experiments performed at 6 μs dwell time. Line profiles extracted from the center of the images with a 256 pixel integration width. Line profile corresponding to the experiment scanning with the raster method in a and to the interleaved method in b.

to the right of the profile (middle to down direction in the images), which indicates amorphization of the sample. In the central region, the reduced intensity suggests loss of mass. For the data acquired with the interleaved method, the profile still preserves the nanometer scale variations with reduced signal amplitude on the central region; however, with a sub-nanometer scale modulation suggesting alternating loss of mass resulting from the periodic array of pixels that came early in the scan with respect to those that came later. Here the shift of the peaks continues for the leftmost positions.

In Figure 5.8 the line profiles correspond to the images acquired with 9 μs dwell time,

displayed in Figure 5.6. The line profile corresponding to the first acquisition acquired with the raster method, Figure 5.8.a, already shows missing subnanometer scale variations mostly in the central region of the profile while the profile corresponding to the alternative method already looks noisy. For the second acquisition with the raster method, the nanometer scale variations are completely lost mostly from the center to the right of the profile, which indicates that amorphization of the sample is enhanced in the scanning direction. In the central region, the reduced intensity suggests loss of mass while the increased intensity to the right indicates mass accumulation. For the data acquired with the interleaved method, Figure 5.8.b, the profile still preserves the nanometer scale variations with a clear reduced signal amplitude on the central region; however, with a subnanometer scale modulation suggesting alternating loss of mass.

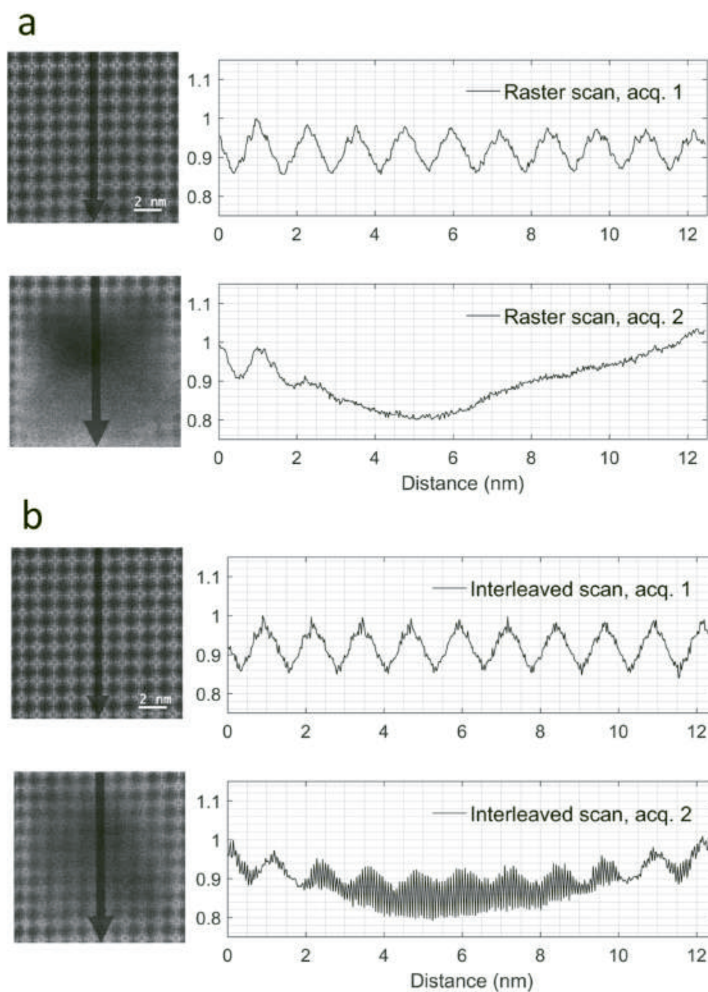

FIGURE 5.8: Integrated line profiles of images in Figure 5.6, experiments performed at 9 μs dwell time. Line profiles extracted from the center of the images with a 256 pixel integration width. Line profiles corresponding to the raster method in a and to the interleaved method in b.

As mentioned earlier in this chapter, the alternating loss of mass could also be the reason for the additional spots at high frequency in the diffractogram shown in Figure 5.4.b2. This effect is clearly identified in the line profiles corresponding to the last acquisitions shown in Figures 5.7.b and 5.8.b; however, it cannot be identified in the line profiles corresponding to the first acquisitions, probably because of very small contrast variations and the integration of the signal to plot the line profile. The interleaved method scans multiple sub-frames to acquire all the pixels in a frame. Skipping two pixels in each scanning direction, 11.1% of the pixels are scanned in each sub-frame, hence nine frames can be obtained by applying a 3 $\times$ 3 sub-sampling procedure to the images acquired with this method. This procedure was applied to the first acquisition of the images acquired with the interleaved method in the 3 $\times$ 3 sub-images experiments, images in areas 2, 4, 6 and 8 as shown in Figure 5.3. These acquisitions pertain to the experiment performed at 6 μs dwell time, 24.3 pm pixel size. The signal from each of the sub-frames was integrated and the mean value of the integrated signals was calculated from all the interleaved acquisitions. Figure 5.9 shows this signal for all the sub-frames. The same procedure was applied to the images acquired with the raster method to show any possible signal variation because of the framework structure. The signals has been normalized with respect to the first sub-frame of the interleaved scanning. Compared to the raster scanning data, for the first sub-frame, a small increase in the signal of the interleaved method is noticed; an increase of about 1%. For the second and third sub-frames the increase is less than 1%. For the rest of the sub-frames, the signal is quite similar to the one obtained for the raster acquisition. The signal variation of the data obtained for the raster acquisitions is larger, which is indicated by the error bars. This data suggests a small decrease in the signal within the first three sub-frames scanning with the interleaved method, probably because of the effect of early beam damage. The signal decay can be fitted to an exponential curve. This function can be used to weight the pixels in the sub-frames according to the signal decay. Figure 5.10 shows the diffractogram of the raw image acquired in one of the areas of the 3 $\times$ 3 sub-images experiment and the diffractogram after applying this approach. Fainter extra spots are shown in the latter case.

The observations described above were consistent for all the scanned areas of the 3 $\times$ 3 sub-images experiments. Figure 5.11 shows larger field of view acquisitions recorded after the experiments from which the images in Figure 5.5 and 5.6 were extracted. The images were acquired with the conventional raster method at a lower magnification, at 3 μs dwell time, after the last acquisition of the corresponding experiment finalized. The flyback delay was set to zero, and only cropped central regions, exempt from distortions, are shown. The areas scanned with the raster method, areas numbered 1, 3, 5, 7 and 9 as depicted in Figure 5.3, are darker indicating an increased loss of mass compared to the areas scanned with the interleaved method. The bright edges surrounding the scanned areas indicate accumulation of mass. The mass probably diffused from the scanned area (darker) to it surrounding

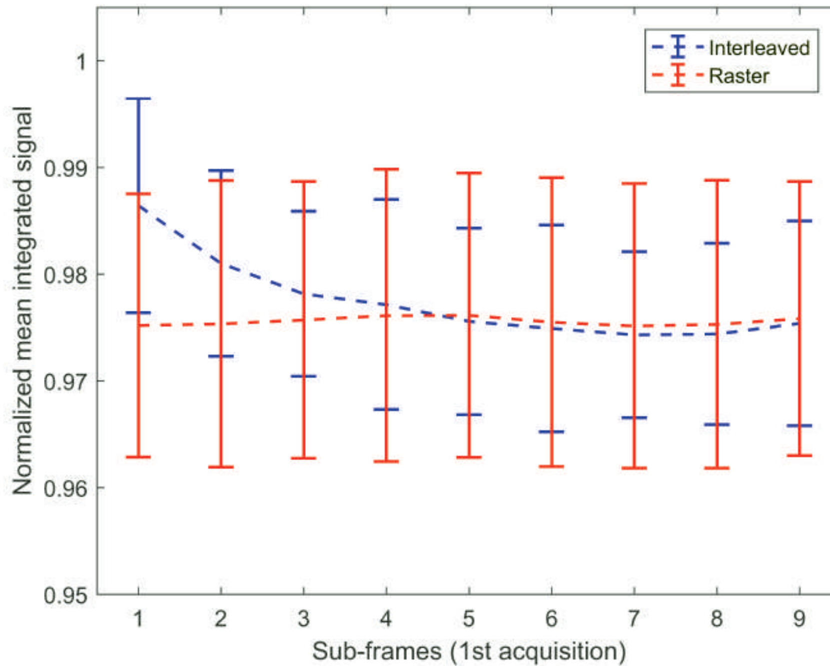

FIGURE 5.9: The interleaved method scans multiple sub-frames to acquire all the pixels in a frame, 11.1% of the pixels are scanned in each sub-frame. A 3×3 sub-sampling procedure is applied to the images acquired with the interleaved method. The intensity from each of the sub-frames is integrated and the mean value is calculated from all the acquisitions with the interleaved method in the 3×3 sub-images experiments (as shown in Figure 5.3) scanning at 6 μs dwell time, 24.3 pm pixel size, three acquisitions. The procedure is applied to the first acquisition. As a comparison, the same procedure is repeated to the raster acquisitions. The signals has been normalized with respect to the first sub-frame of the interleaved scanning. Compared to the raster scanning data, for the first sub-frame, a small increase in the signal of the interleaved method is noticed; an increase of about 1%. For the second and third sub-frames the increase is less than 1%. For the rest of the sub-frames, the signals are quite similar. The signal variation of the data obtained for the raster acquisitions is larger, which is indicated by the error bars. This data suggests a small decrease in the signal within the first sub-frames scanning with the interleaved method, probably because of the effect of early beam damage.

(brighter) during the scanning. More damage is noticed when comparing the last acquisitions of the experiments in Figures 5.5 and 5.6 with these large field of view images. The increased damage could be explained by its dynamic nature which would explain damage propagation even during intervals of no-irradiation and/or could be the effect of unavoidable beam damage during this large field acquisition itself, even at lower magnification and reduced dwell time. Although, in the course of the experiments, negligible beam damage was observed from single acquisitions at those conditions; however, this could be enhanced by the accumulation of damage from the previous experiments performed at much higher magnification. Here, the increased damage of the experiment acquired at 9 μs dwell time compared to 6 μs dwell time is also clear. For the 9 μs dwell time experiment, the scanned

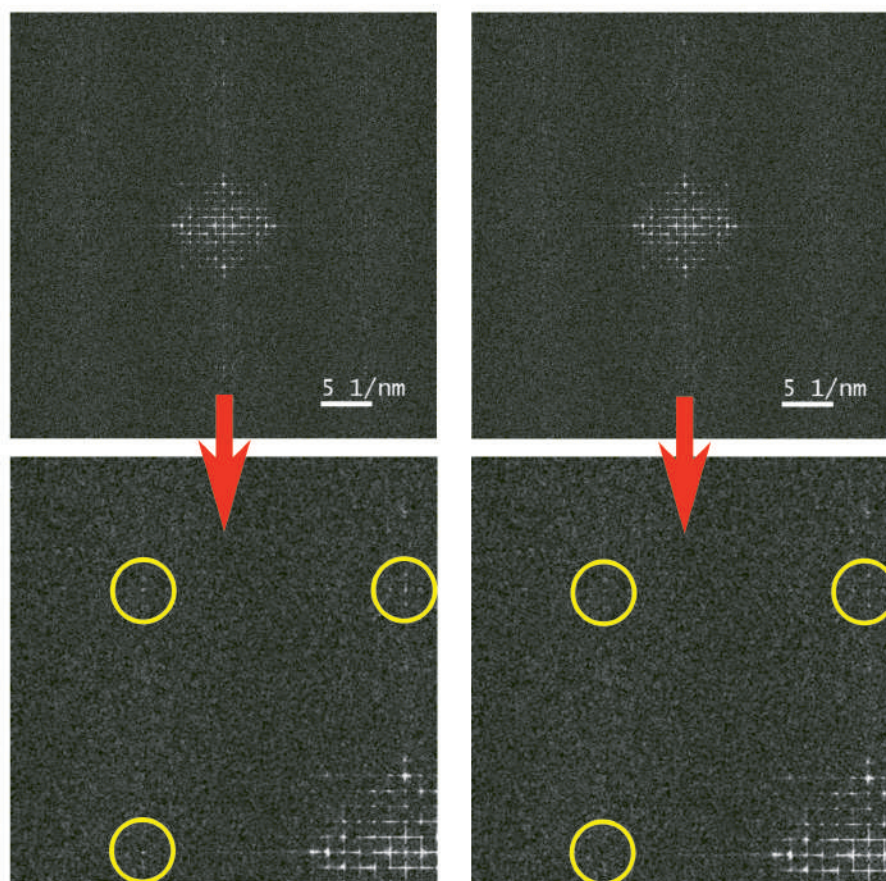

FIGURE 5.10: The data from the interleaved acquisitions shown in Figure 5.9 can be fitted to an exponential curve. This function is used to weight the pixels from each of the sub-frames according to the signal decay. Left, diffractogram of the raw image acquired in one of the areas of the 3 × 3 sub-images experiment. Right, diffractogram after applying this approach. Fainter extra spots are shown in the latter case.

areas, scanned with the raster and interleaved methods, are darker than in the 6 μs dwell time experiment, furthermore the edges are brighter.

More experiments were conducted over the same crystal at different dwell times and pixel size, showing similar results; less damage was observed on areas scanned with the interleaved method. As an example, images corresponding to an experiment acquired at 12 μs dwell time and 34.3 pm pixel size, with a dose of $3.18 \times 10^4 e^- Å^{-2}$ per image, can be found in Figure 5.12. Two consecutive acquisitions were performed. Drift of the sample is observed during the large dwell time.

According to the assumed role of diffusion in the damage process, discussed in chapter 3, an area that will be scanned at some point in the acquisition sequence could be already affected while scanning the other areas. For example, the central region scanned with the

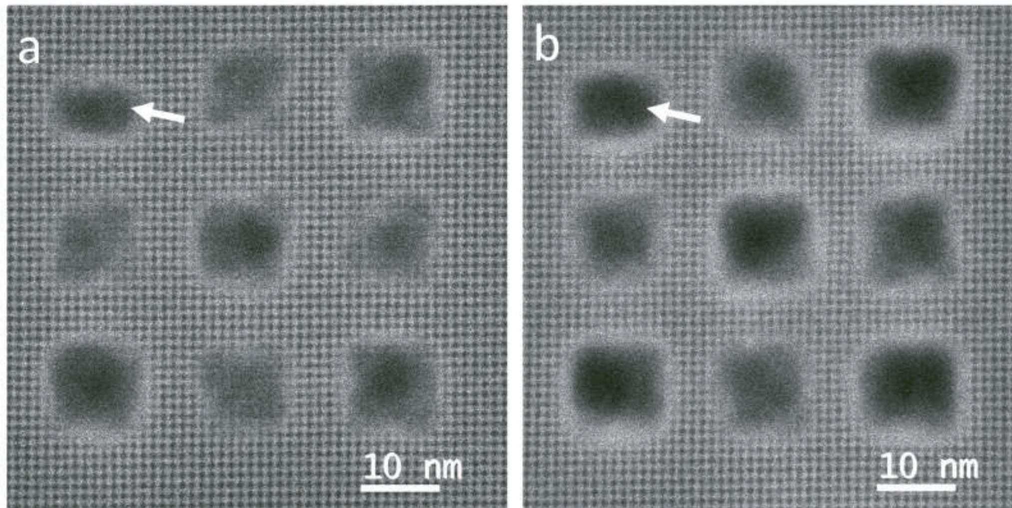

FIGURE 5.11: Large field of view acquisitions after performing the experiments shown in Figure 5.5 (3 aquisitions at 6 μs) which is presented in a, and in Figure 5.6 (2 aquisitions at 9 μs) which is presented in b. Identical contrast settings were used. As indicated by the contrast, the areas scanned with the interleaved method show less damage in both experiments. When comparing areas scanned with the same method in both experiments, less damage is observed in a compared to b, even though the same electron dose was applied in both cases. The first and last sub-images were illuminated partially due to the manual opening and closing of the beam shutter and are ignored for further analysis. The white arrow indicates the first sub-image that was clearly partially illuminated.

raster method, area numbered 5 in Figure 5.3, which is enclosed by the rest of the neighboring areas, would potentially suffer more. To clarify whether or not the scanning sequence has some influence on the damage patterning, acquisitions were conducted inverting the sequence of the scanning methods. Experiments were performed starting with interleaved scanning instead of raster scanning and alternating the methods afterward. Similar results were obtained in a different crystal with the inverted scanning sequence. More damage was found in the areas scanned with the raster method, independent of the scanning sequence. A large field of view image acquired after the sub-images experiment is shown in Figure 5.13.

To further illustrate and quantify the diffusion process, holes were created by placing a static beam over the sample for different irradiation times. At the time scale in s reported here, the size of the holes, which increases with the irradiation time, were bigger than the area irradiated by the probe, clearly indicating a non-local process. The holes were created in the same crystal where the 3×3 sub-images experiments were performed, close to the region of the experiments. The beam was placed in areas of interest previously focused in scanning mode. The irradiations were carried out for 2 s, 5 s, and 10 s. Low magnification images at 3 μs dwell time were acquired afterwards. The images are shown in Figure 5.14, only cropped central regions are presented in the figure. The inset shows a line profile

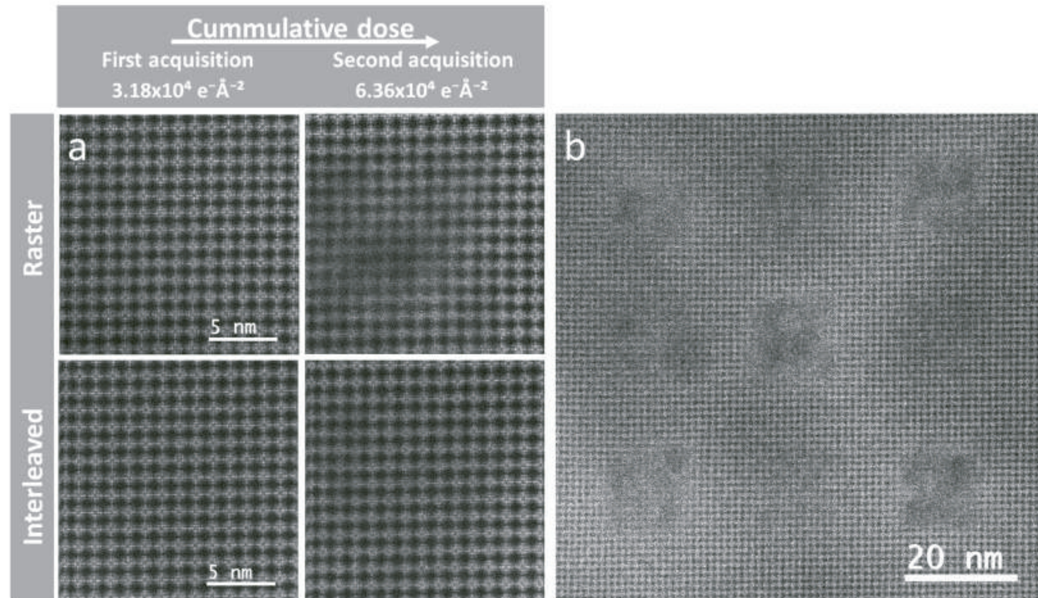

FIGURE 5.12: Images from a 3×3 sub-images experiment consisting of two acquisitions performed at 12 μs dwell time, 34.3 pm pixel size, and a calculated dose of approximately $3.18 \times 10^4 e^- Å^{-2}$ per image. a. Extracted images from the areas 5 and 4 (corresponding to the raster and interleaved scanning, respectively) of the sub-images experiment, as depicted in Figure 5.3. Drift of the sample is observed during the large dwell time. b. Large field of view acquired after performing the experiment, image acquired at 3 μs dwell time. The areas scanned with the interleaved method show less damage than the areas scanned with the raster method.

taken across the center of the hole created with the longest irradiation time, the intensity corresponding to the center of the hole is approximately ten times the intensity in vacuum, which indicates that these are not through holes.

A rough approximation of a diffusion coefficient can be calculated from the size of the holes and the irradiation time. We assume a constant diffusion coefficient for regions of uniform thickness. Perhaps, the experiment with the shortest irradiation time, 2 s, is more representative of the diffusion process as the density of the material that diffuses out will change as a function of the irradiation time. As the width of the damage profiles is less than 10 nm and the irradiation time in s, the diffusion constant would be in the order of $\sim$ nm^2/s. An estimation of this coefficient based on a comparison with the experimental results is given in the next chapter.

In this sample, damage was observed to occasionally heal with time, in line with others observing similar effects [66, 109]. As a comparison, K. A. Mkhoyan et al. reported the diffusion of Ca ion in thin films of $CaO - Al_2O_3 - SiO_2$ glass when irradiating with a static electron beam. A diffusion coefficient was estimated from the size of the holes created on the sample and the irradiation time $\sim$ 1 nm^2/s. Full recovery after mass migration from the damaged area was reported. Electrostatic charging was presumed to be the reason for

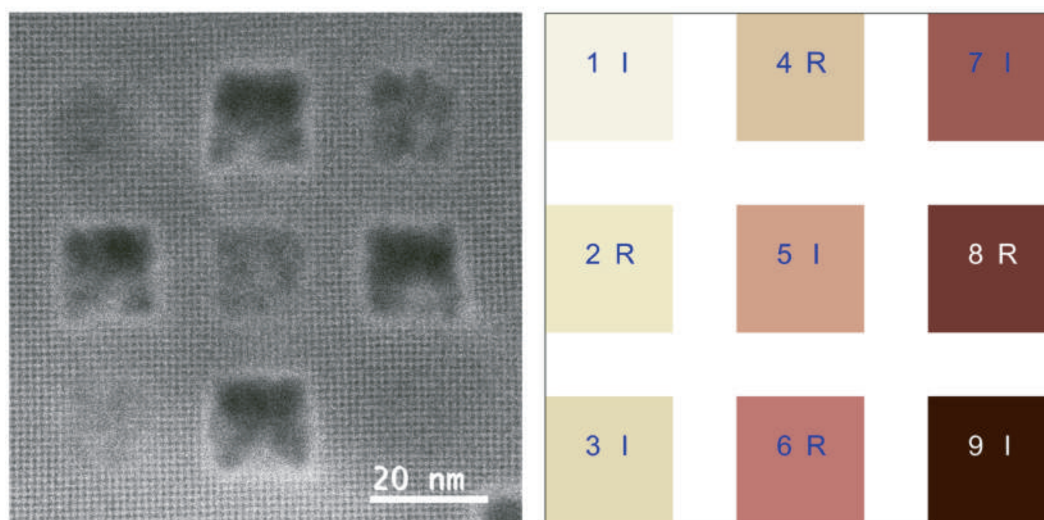

FIGURE 5.13: Left, large field of view acquired after performing an experiment consisting of two acquisitions acquired with 34.3 pm pixel size, 14 μs dwell time and a calculated dose of approximately $3.71 \times 10^4 e^- Å^{-2}$ per image. The sequence of the scanning methods for each squared area was inverted with respect to the previous results. Right, sequence of the scanning methods employed here, alternating the interleaved scanning (I) and raster scanning (R). The sequence is inverted with respect to the sequence in Figure 5.3. The areas scanned with the interleaved method show less damage than the areas scanned with the raster method.

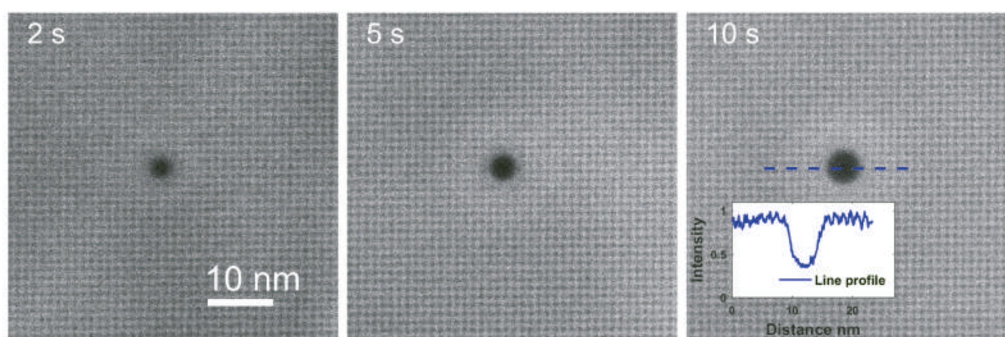

FIGURE 5.14: Holes created by placing a static beam over the sample for different irradiation times, 2 s, 5 s and 10 s. The images were acquired at low magnification scanning at 3 μs dwell time, only cropped images of the central regions are shown. Inset, line profile across the center of the hole, as shown by the dashed line.

damage; however, the driving forces of the Ca atoms that diffused back remain unclear. In our sample, similar in composition, we report partial self-filling of a hole after being created with the stationary beam, Figure 5.15.

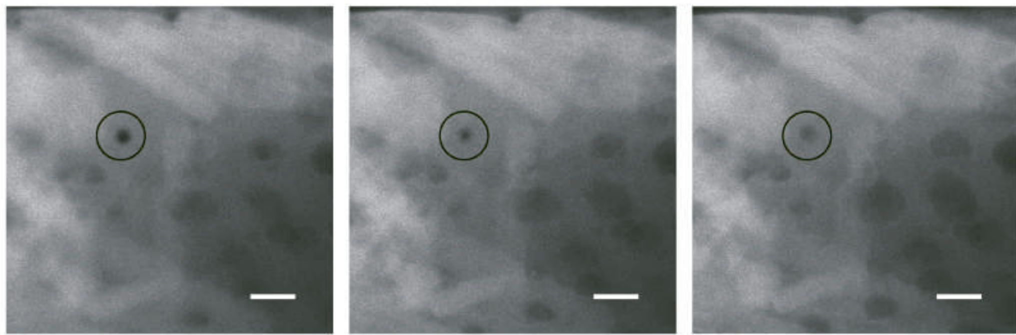

FIGURE 5.15: Partial self-filling of a hole after being created with a stationary beam. The hole is marked by the black circle. From left to right, the images were scanned with a time interval of approximately 38 s between the acquisitions. The scale bar represents 20 nm.

Porous Cu-compound sample

The experiments described above were repeated on the porous Cu-compound sample. The microscope was operated at the same conditions as before (300 kV in HAADF-STEM mode, a spatial resolution of approximately 0.8 Å, and 50 pA of beam current). Again, 3×3 sub-images experiments were performed on a thin crystal of uniform thickness, alternating the raster and interleaved scanning following the sequence sketched in Figure 5.3.

Two images, acquired with the raster and interleaved methods, extracted from a 3×3 sub-images experiment are compared in Figure 5.16. The experiment was performed with 34.3 pm pixel size, scanning at 12 μs dwell time, and an electron dose of $3.2 \times 10^4 e^- Å^{-2}$. Amorphization is present on the lower half of the acquisition with the raster method. The scanning conditions and dose are the same as the employed to acquire the image in Figure 3.3.c from chapter 3. Damage is not visually identified on the image acquired with the interleaved method. Figure 3.3.f shows and image acquired with similar electron dose, reducing the beam current to 25 pA and scanning with the raster method. In that case, damage was reduced compared to an acquisition with 50 pA of beam current and similar dose. However, some damage was still identified suggested by the change in the contrast on the lower area and the bright spots indicating the formation of clusters. This is not the case, compared to the image acquired with the interleaved method here.

Occasionally, partial recovery was also observed in this sample. Partial self-filling of holes is reported in this case as well.

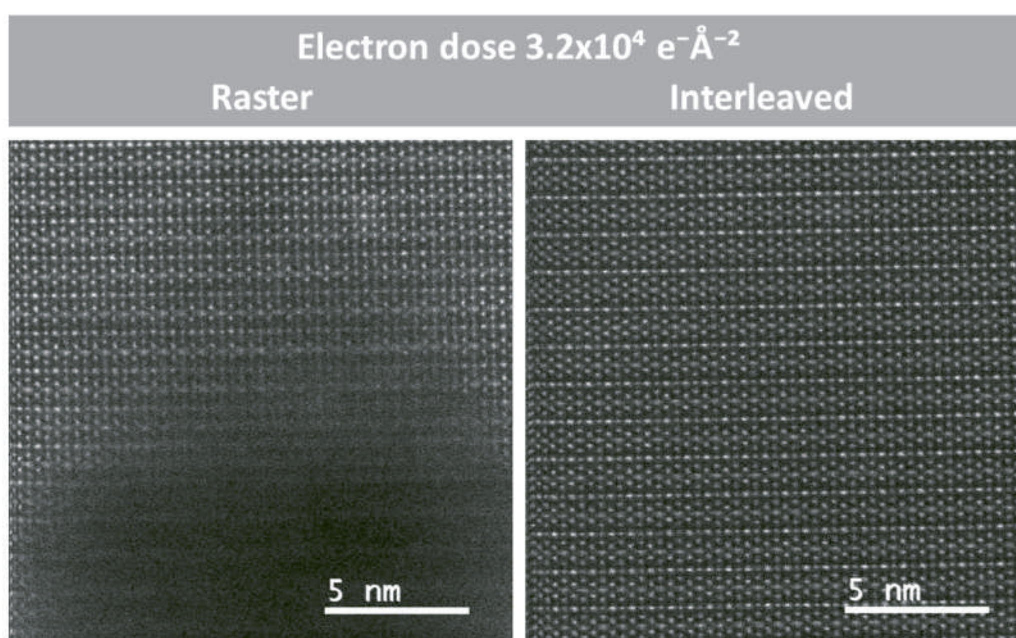

FIGURE 5.16: Extracted images from a 3×3 sub-images experiment consisting of one acquisition performed at 12 μs dwell time, 34.3 pm pixel size, and a calculated dose of $3.2 \times 10^4 e^- \text{Å}^{-2}$ per image. The images were acquired with the raster and interleaved scanning following the sequence sketched in Figure 5.3. Similar dose as the applied to acquire the images in Figure 3.3.c and 3.3.f from chapter 3.

5.3 Comparison and quantification of beam damage

In this section we compare and quantify the amount of damage observed on the zeolite sample when scanning with the raster and interleaved methods.

Beam damage can be quantified by the local information at the unit cell scale and can be used to monitor the information content as a function of the applied dose. A template-matching procedure based on a cross-correlation function was employed to find regions (unit cells) of the images that have similar features compared to a template [110].

These similarities were evaluated as a function of the applied dose. The procedure was performed over the first acquisition of the sub-images experiments (i.e. the first acquisition in Figures 5.5 and 5.6), which exhibits moderate damage. A template of 50×50 pixels size corresponding to the sodalite cage was selected and an averaged image was obtained from all the cells that matched the template.

A good match was considered when the outputs of the cross-correlation function where larger than a threshold, 45% with respect to the maximum output value. This averaged image was used iteratively as a new template for all the acquisitions. First, the template-matching methodology was applied to a Gaussian (sigma = 3.5 pixels) filtered version of the raw images, which exhibit low SNR and poor contrast because of beam damage effects. Then, the positions of the cells that matched the templates were used to extract the cells from a new template-matching procedure applied to the raw unfiltered images. Because of the distortions on the left side of the images, the first left column of the sodalite cages was excluded during the template-matching procedure. The first or last row of the sodalite cages was excluded only in cases where the cages were not fully imaged on the first acquisitions. The same procedure was applied separately for each of the scanned areas in the 3×3 sub-images experiments. With this procedure, an averaged template image can be also obtained for all the further acquisitions of the experiments. Figures 5.17 and 5.18 show the averaged images of the sodalite cage obtained from each of the acquisitions in Figures 5.5 and 5.6, experiments performed at 6 and 9 μs dwell time, respectively. In both figures, reduced loss of the structure is evident after the first acquisitions done with the interleaved method.

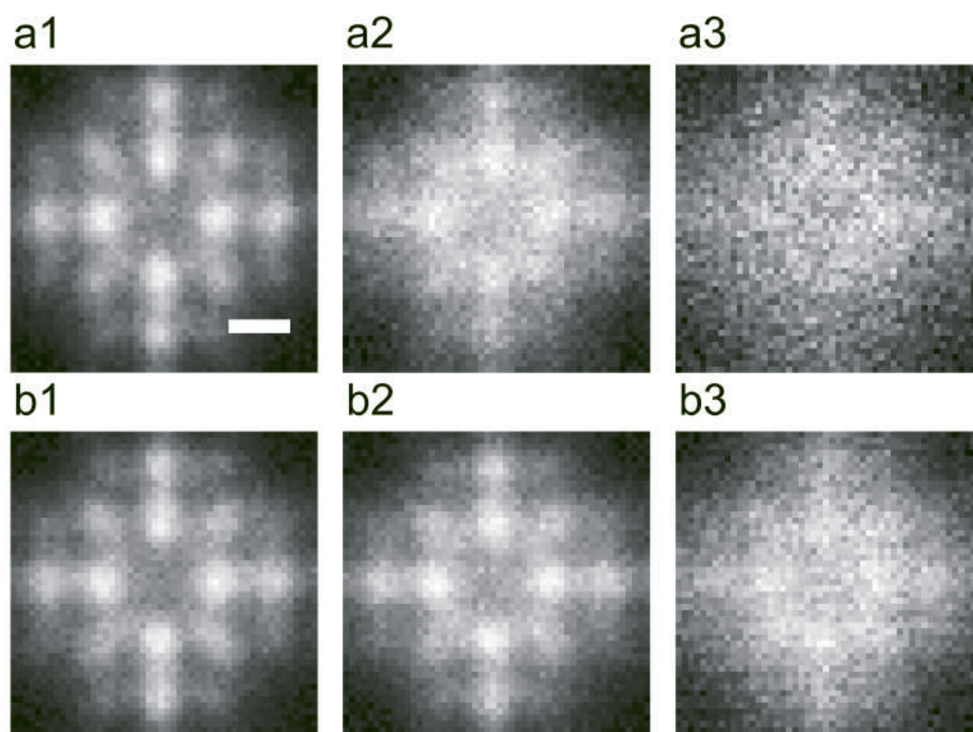

FIGURE 5.17: Averaged image of the sodalite cage obtained with a template-matching procedure applied to the images from Figure 5.5 (6 μs). a1, a2 and a3, represent first, second and third acquisitions with the raster method, while b1, b2 and b3 represent results from the interleaved scan method. The number of cells found in each case is listed in Table 5.2. (scale bar 0.2 nm).

Table 5.2 summarizes the number of cells found with this procedure.

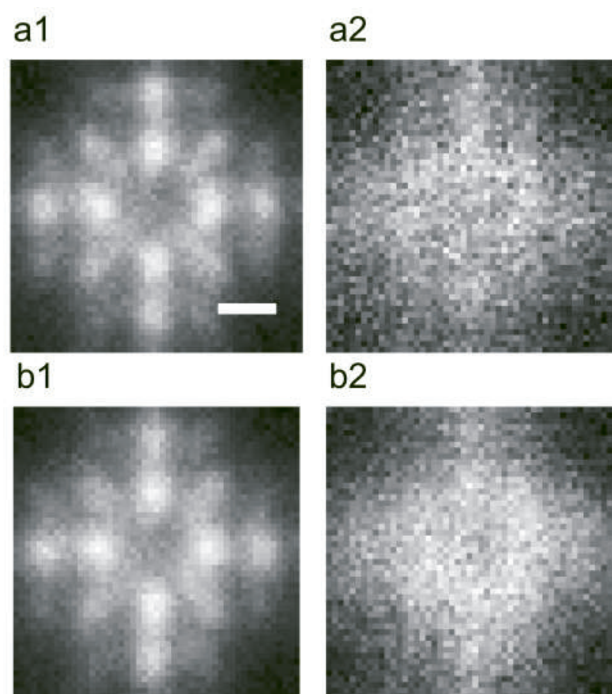

FIGURE 5.18: Averaged image of the sodalite cage obtained with a template-matching procedure applied to the images from Figure 5.6 (9 μs). a1 and a2, represent first and second acquisitions with the raster method, while b1 and b2, represent results from the interleaved scan method. The number of cells found in each case is listed in Table 5.2. (scale bar 0.2 nm).

TABLE 5.2: Number of cells averaged in the template-matching procedure.

	6 μs dwell time Number of cells		9 μs dwell time Number of cells	
	Raster scanning	Interleaved scanning	Raster scanning	Interleaved scanning
1st acquisition	81	81	81	81
2nd acquisition	81	81	35	81
3rd acquisition	55	81		

The reduced number of cells found in the last acquisitions for the raster method is the result of severe loss of mass and amorphization in the central-bottom regions making it difficult to recognise the template. In these cases, the cells were found mainly on the edges of the images. Figure 5.19 shows the location of the cells on the three acquisitions of the raster images from Figure 5.5. Their locations with respect to the first acquisitions may change because of sample deformation or drift of the sample. As indicated earlier, deformation of the structure was observed predominantly on the top region of the images while negligible drift was noticed.

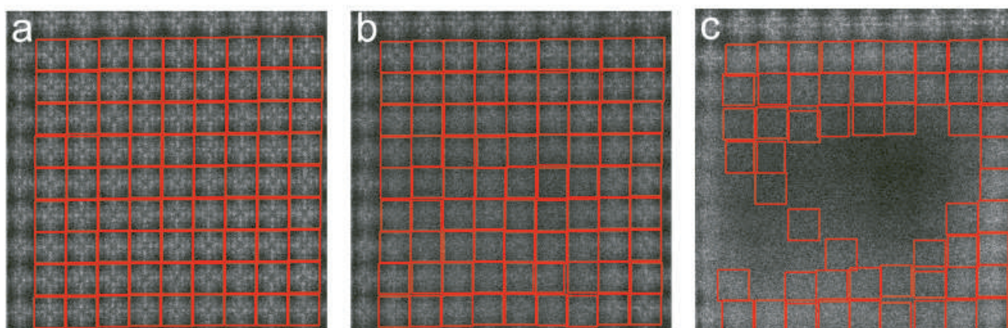

FIGURE 5.19: Location of the cells (red squares) obtained with the cross-correlation method. The locations are shown on the raw raster images from Figure 5.5. a, b and c correspond to the first, second and third acquisitions, respectively.

Before quantifying damage, we used the location of the cells to estimate the drift during the 3×3 sub-images experiment consisting of three consecutive acquisitions, scanning at 6 μs dwell time, 24.3 pm pixel size, with a time difference of 6 s between acquisitions. The interleaved acquisitions shown in Figure 5.5 correspond to this experiment. Drift was estimated by measuring the displacement of the cells between consecutive acquisitions. It was measured from the alternative acquisitions as less beam damage was observed in these images. The lower part of the first and second acquisitions were analysed as more damage was identified in the upper part (shown by the line profiles in Figure 5.7), and the drift was assumed constant during the course of the experiment. The drift rate was considered negligible during the acquisitions, see Figure 5.20. In addition, the displacement of the cells is presumed to be mainly because of shrinkage of the sample, which is deduced from Figure 5.20.

As the sample degradation increases, the cells corresponding to the sodalite cages deviate more from the ideal averaged image. The degree of similarity can be represented by the normalized cross-correlation (NCC) coefficients and can serve as a quantative parameter representing beam damage [69]. The coefficient values vary from -1 to 1, which indicates a variation from a bad to a good similarity with respect to the template. However NCC = 1 is infeasible as the cells are compared to an averaged template and noise in the images

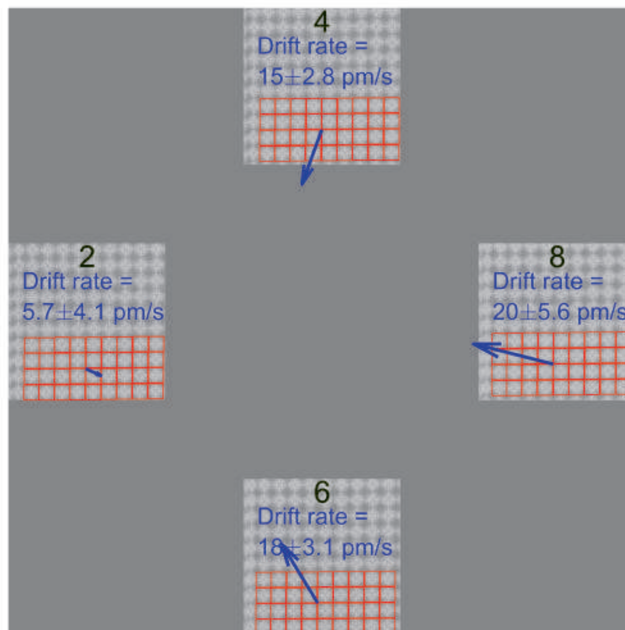

FIGURE 5.20: Areas 2, 4, 6 and 8 of a 3 × 3 sub-images experiment (see Figure 5.3) acquired with the alternative scanning at 6 μs dwell time, 24.3 pm pixel size. The interleaved images shown in Figure 5.5 correspond to this experiment, which consisted in three acquisitions with a time difference of 6 s between them; only the first acquisition is shown here. The red squares indicate the location of the cells obtained with the cross-correlation method. Drift was estimated from the displacements of the cells between the second and first acquisitions. The arrows represent the sum of the drift vectors obtained for each of the cells shown here. The vectors suggest displacement of these areas in the outside-in direction, presumably because of shrinkage of the sample. Furthermore, the magnitude of the vectors increases following the sequence of the scanned areas, suggesting more damage/shrinkage as the scanning progresses. A mean value for the drift rate is given for each of the scanned areas. The drift rate is considered negligible during the acquisitions.

will make that two images are never identical even when no damage occurs[3]. The actual level of the NCC coefficient even for a perfect match depends on the SNR but could be calculated from Poisson statistics. For example, Figure 5.21 shows the variation of the coefficients, with the SNR, calculated for two images (100 × 100 frame size, created from a normal distribution) that only differ from Poisson noise. In general, sample deformation, amorphization, contrast loss, increased noise, etc., all reduce the NCC.

Here, the indices corresponding to the NCC coefficients of all the cells found on the first acquisitions were used to extract the coefficients for the next acquisitions. This way the same number of cells are always considered, 81 cells in all the cases, and beam damage is not understimated by considering a reduced number of cells. The mean of the NCC coeffcients was calculated for all the scanned areas of the 3 × 3 subimages experiments and

[3]Although the NCC coefficients give an indication of damage, these are not an absolute measure for damage. For instance, NCC = 0 would correspond to an image that is orthogonal to a reference undamaged image which would be an unphysical situation that cannot occur from damage.

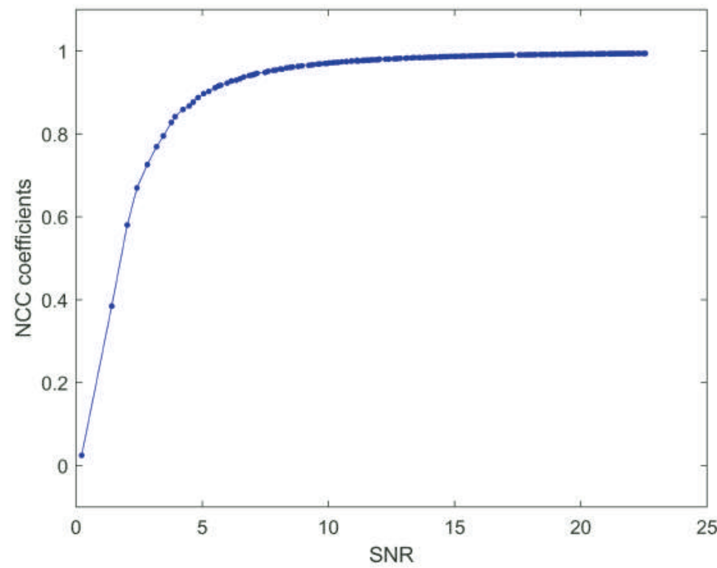

FIGURE 5.21: Variation of the NCC coefficients with SNR. The coefficients were calculated for two images (100 × 100 frame size, created from a normal distribution) that only differ from Poisson noise.

plotted as a function of the applied dose in Figure 5.22.

With both scan patterns the mean of the NCC coefficients decreases as a function of dose. The mean of the coefficients of the first acquisitions is quite similar for the raster and interleaved scanning. However, for the further acquisitions (as the dose increments), the average NCC for raster scanning is significantly lower when compared to interleaved scanning for the same collected dose. This agrees with the qualitative observations of beam damage in the images in Figures 5.5 and 5.6 and in the line profiles in Figures 5.7 and 5.8, where damage is more pronounced when scanning with the raster method but now takes into account all scanned images for improved statistics and provides an error bar as the standard deviation across all unit cells.

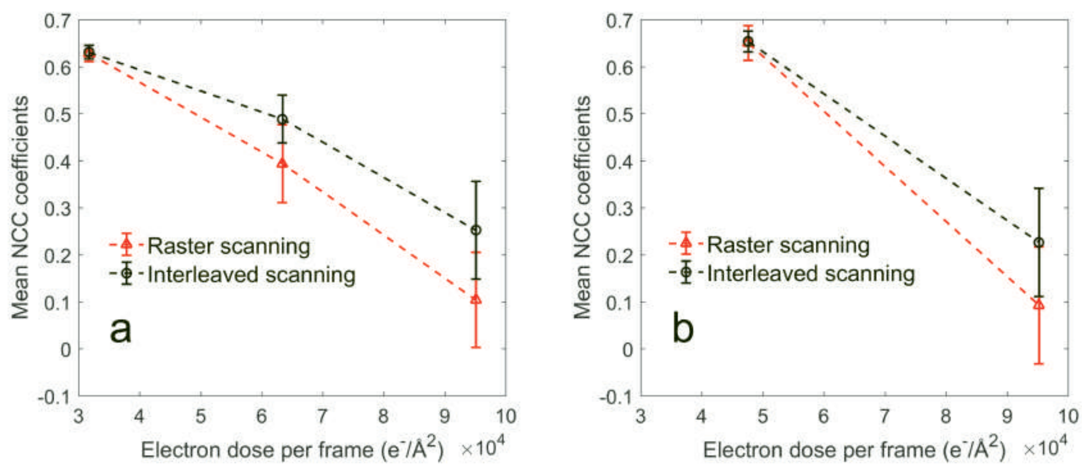

FIGURE 5.22: Mean NCC coefficients, obtained with template-matching as a function of accumulated dose per frame. The error bars pertain to the standard deviation over the multiple areas scanned in each 3×3 sub-images experiment. a. Plot corresponding to the three acquisitions of the experiment performed at 6 μs dwell time. b. Plot corresponding to the two acquisitions of the experiment performed at 9 μs dwell time.

The mean NCC coefficients for both experiments, from Figures 5.22.a and 5.22.b are given in Table 5.3. The reason for having similar coefficients for the first acquisitions of both experiments is due to the fact that the scanned areas from each experiment were compared to its own averaged image. Even then, as highlighted from the line profiles, the first acquisition of the experiment acquired at 9 μs dwell time, applied dose $4.76 \times 10^4 e^- Å^{-2}$, already shows more damage compared to the first acquisition of the experiment acquired at 6 μs dwell time, applied dose $3.17 \times 10^4 e^- Å^{-2}$. The coefficients are clearly reduced with respect to the first acquisitions. From Figure 5.22.a, when scanning with the raster method, a reduction of 37.3% and 83.4% for the second and third acquisitions are observed, respectively. While for the interleaved method, 22.5% and 60.0% of reduction are remarked for the second and third acquisitions, respectively. From Figure 5.22.b, a reduction of 85.8% and a reduction of 65.4% for the second acquisitions scanning with the raster and interleaved method are observed, respectively. For all the cases, the reduction of the coefficients obtained for the raster method is larger than the ones obtained for the interleaved method.

TABLE 5.3: Mean NCC coefficients from Figures 5.22.a and 5.22.b obtained with the template-matching procedure.

	6 μs dwell time Mean NCC coeficcients		9 μs dwell time Mean NCC coeficcients	
	Raster scanning	Interleaved scanning	Raster scanning	Interleaved scanning
1st acquisition	0.628	0.631	0.650	0.653
2nd acquisition	0.394	0.489	0.092	0.226
3rd acquisition	0.104	0.252		

Another way to quantify the changes in the sodalite cages/cells is by the mean intensity in each cell. As the HAADF signal is proportional to the thickness of the sample, the changes in the signal corresponding to the sodalite cages can be interpreted as a change in density of the material, e.g. due to mass loss or accumulation of mass. Again, the locations of the cells found on the first acquisitions with the previous procedure were kept for all the further acquisitions to make sure also the more damaged areas are maintained in the evaluation. In order to maintain the absolute intensity, this methodology was applied to the raw images with an intensity scale zero calibrated with a blanked beam. The histogram distributions of the mean intensities of the cells corresponding to the first, second and third acquisitions from Figure 5.5 at 6 μs dwell time, can be found in Figure 5.23.

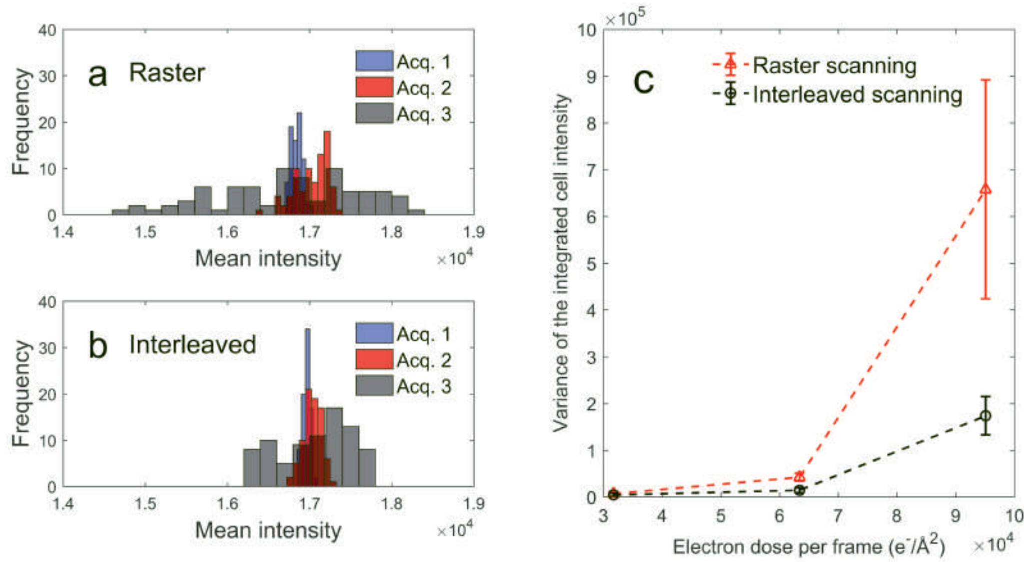

FIGURE 5.23: Histogram distribution and variance of the mean intensities of the cells found with the template-matching procedure. The locations of the cells found on the first acquisitions are kept for all the further acquisitions, and the mean intensities of each of the cells are calculated for all the acquisitions. Distributions corresponding to the experiments acquired at 6 μs dwell time, 24.3 pm pixel size. a and b show the results for the raster and interleaved scanning acquisitions, respectively, from Figure 5.5. c. Mean variance of the mean intensities as a function of the accumulated dose per frame. The mean of the variance is considered from the scanned areas of the 3×3 sub-images experiment. Areas numbered 3, 5 and 7 were considered for the raster scanning and areas numbered 2, 4, 6 and 8 were considered for the interleaved scanning. The errors bars correspond to the standard deviation.

For the first acquisitions, low variation on the mean intensities of the cells is expected as the images were acquired on regions of uniform thickness, this is indeed observed as a narrow distribution in the histograms. However, as the applied dose increases, the histogram distribution widens as an indication of mass variation. For the second acquisition, with the raster scanning, a left-tailed distribution with the mean slightly shifted to the right is shown, which may suggest that mass is moving around from regions of the sample that become thinner. In Figure 5.7.a, the clear reduction of the signal amplitude observed in the central region of the line profile can be interpreted as thinning of the sample. For the interleaved scanning, the distribution becomes wider, suggesting that the mass is re-distributed in the frame. The line profile in Figure 5.7.b does not reveal any evident reduction of the signal amplitude. For the third acquisition, with the raster scanning, the histogram shows a wide distribution with tails towards lower intensities suggesting loss of mass. Likewise, for the interleaved scanning, the distribution widens and skews even though the width remains lower than for the raster case and remains centered with respect to the mean of the first acquisition. Figure 5.23.c shows the mean of the variance from the histograms of the raster and interleaved acquisitions calculated from the different scanned areas of the 3×3

sub-images experiment. The mean of the variance was calculated for the three acquisitions of the experiment, the error bars on the plot correspond to the standard deviation. For both scanning methods, the variance increases as a function of the dose. This is an indication of the broadening of the distributions which relates to the mass variations in the cells. Here the variances for the first acquisitions are quite similar for both methods. However, for the further acquisitions (as the dose is incremented), the values from the raster scanning show a significantly larger variance as compared to the interleaved scanning. For the raster method, the variance of the second acquisition is 6 times the variance of the first acquisition. For the third acquisition, it is 94 times that value. For the interleaved method, the variance of the average intensity in a unit cell of the second acquisition is 3 times the variance of the first acquisition. For the third acquisition, it is 37 times that value.

For the experiment acquired at 9 μs dwell time, the histogram distributions of the mean intensities of the cells can be found in Figure 5.24. Again, for the first acquisitions, narrow normal distributions are shown. For the second acquisitions, non-normal distributions are depicted. In both cases, the distributions are centered to the left with respect to the mean of the first acquisitions; however, the width of the distribution from the raster scanning is larger compared to the one from the interleaved scanning. Similar to the previous experiment, this suggests loss of mass, being more severe for the raster scanning method. Figure 5.24.c shows the mean of the variance from the histograms of the raster and interleaved acquisitions calculated from the different scanned areas of the 3×3 sub-images experiment. The mean of the variance was calculated for the two acquisitions of the experiment, the error bars on the plot correspond to the standard deviation. For both scanning methods, the mean of the variance increases as a function of the dose. The variances for the first acquisitions are quite similar for both methods. However, for the second acquisitions, the values from the raster scanning deviates from the value of the interleaved scanning. For the raster method, the variance of the second acquisition is 132 times the variance of the first acquisition. For the interleaved method, the variance of the second acquisition is 48 times the variance of the first acquisition. Loss of mass is apparent from the histogram of the experiment at 6 μs dwell time scanning with the raster method, while for the experiment performed with the interleaved method at 6 μs dwell time, only a re-distribution of the mass is proposed from the histogram. Despite the fact that the total accumulated dose in both experiments is the same (experiments consisting in three acquisitions at 6 μs dwell time and two acquisitions at 9 μs dwell time), increased loss of mass is apparent from the last histograms of each of the experiments at 9 μs dwell time. These findings suggest reduced damage scanning with the interleaved method and for distributing the dose in more acquisitions scanning at a higher speed. This can also be interpreted from the plots in Figures 5.23.c and 5.24.c where the variance from the last acquisitions is less when scanning at those conditions.

From the large field of view images acquired after performing the 3×3 sub-images

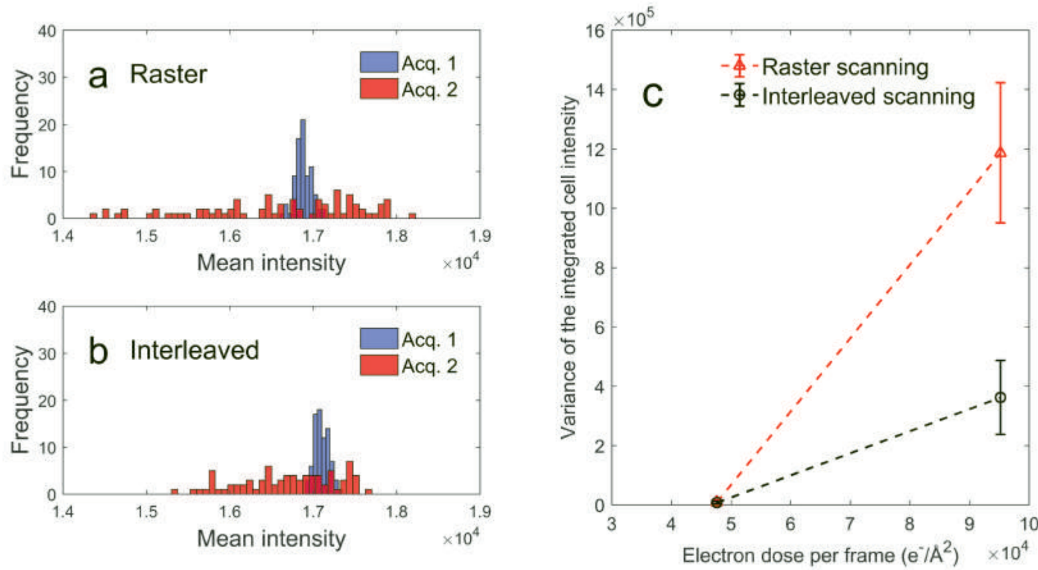

FIGURE 5.24: Histogram distribution and variance of the mean intensities of the cells found with the template-matching procedure. The locations of the cells found on the first acquisitions are kept for all the further acquisitions, and the mean intensities of each of the cells are calculated for all the acquisitions. Distributions corresponding to the experiments acquired at 9 μs dwell time, 24.3 pm pixel size. a and b show the results for the raster and interleaved scanning acquisitions, respectively, from Figure 5.6. c. Mean variance of the mean intensities as a function of the accumulated dose per frame. The mean of the variance is considered from the scanned areas of the 3×3 sub-images experiment. Areas numbered 3, 5 and 7 were considered for the raster scanning and areas numbered 2, 4, 6 and 8 were considered for the interleaved scanning. The errors bars correspond to the standard deviation.

experiments, images in Figure 5.11, relative mass loss can be quantified by calculating the ratio between the mean HAADF intensities of the scanned areas and the non-scanned areas in the experiments. Negligible beam damage was considered when acquiring the large field of view images. The relative quantification with respect to the non-scanned areas will allow us to compare the amount of damage between different block experiments. Only the central regions, half of the size of the scanned areas, were considered for the calculations as the damage was observed to be more uniform there. The relative values were calculated with respect to the mean HAADF intensity of the areas close to the corners of the large field of view images in Figure 5.11, non-scanned regions during the experiments, and are tabulated in Table 5.4.

We deduce two clear trends from this table:

- interleaved scanning suffers significantly less mass loss when compared to raster scanning (7.7% and 11% for the 3 and 2 acquisition experiments, respectively, using the same total dose)
- 3 acquisitions at 6 μs dwell time cause significantly less mass loss as compared to 2

TABLE 5.4: Relative mean HAADF intensity between the scanned areas and non-scanned areas of the two different 3×3 sub-images experiments shown by the large field of view images in Figure 5.11.

	6 μs dwell time 3 acquisitions		9 μs dwell time 2 acquisitions	
	Raster scanning	Interleaved scanning	Raster scanning	Interleaved scanning
Relative HAADF intensity (%)	86.5 ± 0.1	94.2 ± 0.1	74.0 ± 0.1	85.0 ± 0.1

acquisitions with 9 μs dwell time for both scan patterns even though they represent the same total dose and total recording time (12.5% for raster, 9.2% for interleaved).

Although no apparent beam damage was found in between the scanned areas of the experiments, for the acquisitions at 9 μs dwell time, some accumulation of mass was observed in those regions as an increased intensity. The gap between the sub-images was approximately 6.2 nm distance; the scanning was performed with 24.3 pm pixel size. As mentioned previously, the mass removed from the central regions was accumulated mainly in the surroundings and could probably diffuse beyond as a result of the experiment itself or when acquiring the large field of view images shown in Figure 5.11. Figure 5.25 shows integrated line profiles, with 15 pixels width, taken horizontally over the large field of view acquisitions of the experiments performed at 6 μs, three acquisitions, Figure 5.25.a1, and 9 μs dwell time, two acquisitions, Figure 5.25.b1. Line 1 and line 4, correspond to the top and bottom regions, respectively, enclosing the area of the experiments, line 2 and line 3 correspond to the regions in between the actual scanned areas. A fixed offset was added to the intensities from the data of line 1 and line 2, and subtracted to the data of line 4 in Figures 5.25.a2 and 5.25.b2 to clearly compare the profiles. The mean intensities and amplitudes of the raw data from the different line profiles are comparable, the experiments were done over the same crystal in areas of uniform thickness. Besides the intensity variations because of the framework structure, the line profiles in Figures 5.25.a2 are mostly flat. Similar characteristics can be seen from the profiles of line 1 and 4 in Figure 5.25.b2; however, lines 2 and 3 show three bumps, indicated by arrows, at the positions where the areas in Figure 5.25.b1 were scanned. The accumulation of mass in the regions between the scanned areas was also found for higher doses, applied in two acquisitions and scanning with a dwell time higher than 9 μs; more accumulation was found when increasing the dose.

The images presented here were acquired at moderate oversampling conditions. Scanning with 24.3 pm and 34.3 pm pixel size, the probe covers approximately a radial distance of 1.6 pixels and 1.2 pixels, respectively. Though some accumulation of damage may have its origin on the overlapping of the irradiated areas corresponding to the size of the probe,

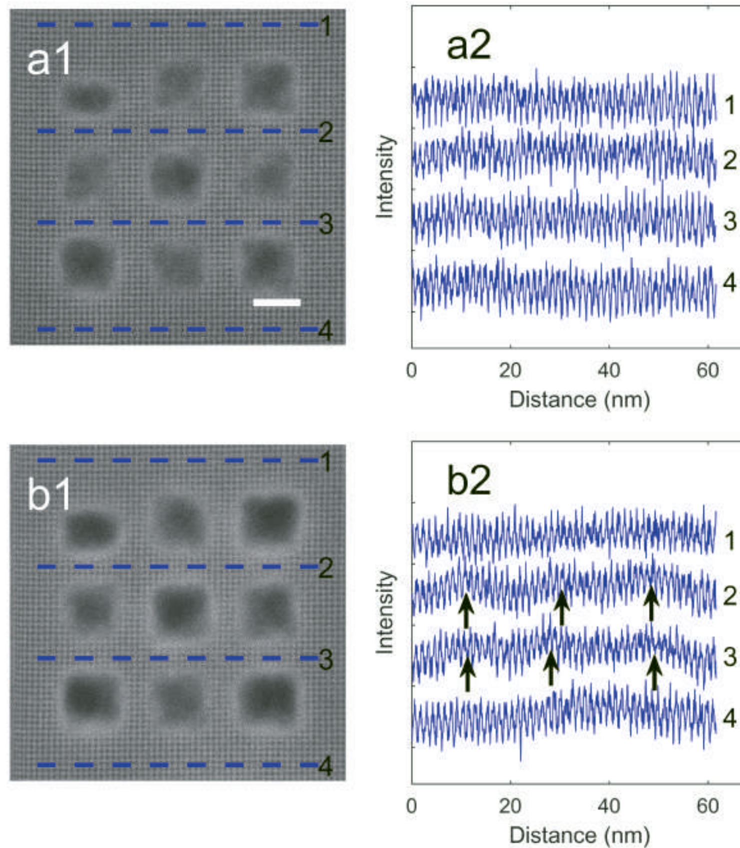

FIGURE 5.25: Integrated line profiles, with 15 pixels width, over the large field of view images acquired after performing the 3 × 3 sub-images experiments shown in Figure 5.11.a1 and b1 correspond to the experiments acquired at 6 μs, three acquisitions, and 9 μs dwell time, two acquisitions, respectively, with 24.3 pm pixel size. a2 and b2 show the data from the line profiles on a1 and b1, respectively. To clearly compare the profiles, a fixed offset was added to the intensities of line 1 and line 2, and subtracted to the data of line 4. The mean intensity and amplitude of the raw data from the different line profiles is quite comparable. Besides the intensity variations because of the framework structure, the line profiles in a2 are mostly flat. Similar characteristics can be seen from the profiles of line 1 and 4 in b2; however, lines 2 and 3 show three bumps, indicated by arrows, at the same positions where the areas in b1 were scanned. The scale bar represents 10 nm.

our experiments indicate a greater damage extension as can be seen from the accumulation of mass on the edges of the scanned regions on the 3 × 3 sub-images experiments, and in between those regions, as indicated in Figure 5.25, and to a greater extent from the damage created with the stationary beam, Figure 5.14.

Figure 5.26 illustrates the proposed damage behaviour when scanning with the raster and interleaved methods with a pixel size smaller than the extension of the diffusion. The spread of the damage from three sequential scanning positions is illustrated, areas inside the dashed circles. A radial damage spread of approximately three pixels distance, greater than the size of the probe, is assumed for illustration purposes. The overlapping of the areas represents accumulation of damage, which is less when scanning with the interleaved

method. Reduced damage in EELS SI by increasing the pixel size greater than the delocalization of damage was achieved in the work from R. F. Egerton et al., the leapfrog scanning method [111]. Similarly, the work from M. Ilett et al. proposes to explore this method in cryo-analytical STEM to reduce beam damage in vitreous ice [112]. However, as mentioned in the work, the maximum increase in pixel size depends on the resolution needed for a specific study, which can be overcome with the interleaved scanning as the same resolution as in the raster method is accomplished.

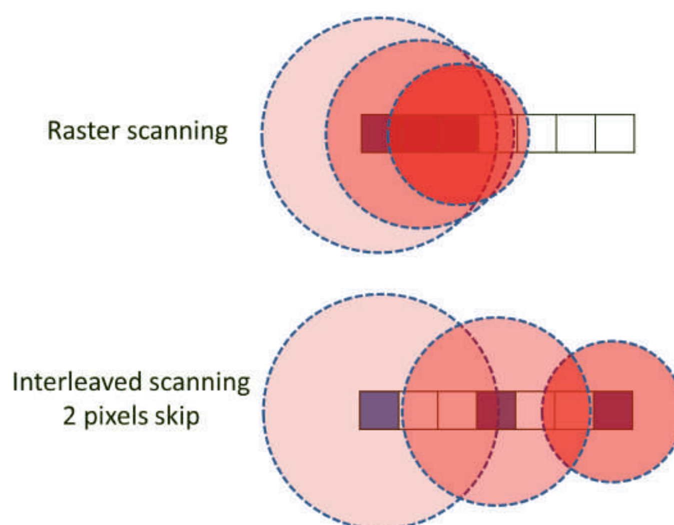

FIGURE 5.26: Illustration of the proposed damage behaviour when scanning with the raster and interleaved methods. The spread of the damage from three sequential scanning positions are illustrated by the areas inside the dashed circles. A damage spread of less than two pixels radial distance per dwell time, greater than the size of the probe, is assumed here for illustration purposes. The color transparency is chosen to change proportionally with the area of the circles to illustrate the diffusion process. The overlapping of the areas represents more damage, which is less when scanning with the interleaved method. The time interval between sequential scanning positions with the raster method corresponds to the dwell time while with the interleaved method, scanning 11.1% in each sub-sampled frame (with a total frame size of 512 $\times$ 512 pixels) at 6 μs dwell time, this interval is approximately 0.17 s.

While the schematic in Figure 5.26 illustrates the difference in the damage spatial distribution scanning with both methods, the temporal characteristic can be exposed by the instants of time at which neighboring pixels are visited by the probe. With the raster method, two neighboring pixels are visited with a time difference of the dwell time. However, with the interleaved method this is done in a much longer interval. Skipping two pixels in each scanning direction, 11.1% of pixels are scanned in each sub-frame. Two neighboring pixels in a scanning line are visited after one sub-frame; for a 512 $\times$ 512 pixels frame size and scanning at 6 μs dwell time, the time difference is approximately 0.17 s. This time interval, not available in raster scanning, may allow to reduce damage accumulation effects, which can be originated by thermal heating or electrostatic charging as discussed in chapter 3, for

instance. In addition, a recovery rate, for cases where a recovery process is present, could compete with a damage rate which would be reduced as no irradiation in the nearby pixels occurs during that interval, hence the latter would be driven mostly by the diffusion process coming from the previous visited pixel.

Most of the processes involved in ionization damage and subsequent atomic displacement take place for a period of time in the range of ps or shorter. Pulsed electron beams of fs pulse durations have shown to reduce beam damage effects in TEM [113, 114]. Within the standard dwell times in STEM, in μs, accumulation of damage from these processes is expected as there is no time between individual events for any possible relaxation. Nonetheless, in our experiments, damage reduction has been observed by changing the pixel scanning sequence, which allows periods of non-irradiation between neighboring pixels in the order of fraction of s. Hence, damage effects that persist in this order of magnitude are presumed to be alleviated with our approach. Delocalised inelastic interactions alone cannot explain this effect [59]. As indicated in chapter 3, in insulators, electrostatic charge can be stored for these periods of time or longer, for instance. In SEM, alternative scan methods [94] and pulsed electron beams (with pulse duration of a fraction of μs) [115] were successively employed to reduce electrostatic charging in insulators.

All of these observations hold clues for a more realistic damage model and the question arises whether other scan patterns or different scan parameters would allow for even lower beam damage while keeping the total dose constant. In order to answer this question, a numerical model is needed that mimics all of these features and would allow searching for an optimal experimental design. This model is discussed in the next chapter. Our experiments, with similar results in different samples, show a systematic study with a statistically significant conclusion which leads to the identification of the important ingredients for a model that might well be applicable outside the current material classes. After all, the model will build on the dissipation of deposited energy without going into the details on how this process takes place in a specific material.

5.4 Discussion

The above work can be summarised in the following statements which will serve as inputs to elaborate the simplest possible empirical model (described in the next chapter) to qualitatively describe all observations:

- Damage occurs in regions that were not visited by the probe.
- Damage depends on the order in which the scan points are visited.
- Damage is higher in central regions of the image as these places have more neighbours.

- When doing mutiple aquisitions, the damage is lower if more frames are recorded for the same total time and same total dose.
- Damage seems to occasionally 'heal' with time.
- In Figure 5.7, similar line profiles were obtained only for the lowest dose applied during the first acquisitions with both scanning methods, raster and interleaved. For the further acquisitions in Figure 5.7 or for the acquisitions in Figure 5.8, differences in the line profiles are more evident. This could be explained by a threshold effect. Although the same dose per frame is applied with both methods, the dose applied to a region of neighbouring pixels during time is different, in a 3×3 pixel region for instance. A more elaborated treshold effect can arise from the accumulated energy, even in one single pixel. As described before, the contribution to the energy in a region of the sample would not only have its origin on the actual scanned position but also on the neigbouring scanned regions. The interleaved method may allow part of this energy to dissipate and a threshold value could be reached at a later step than with the raster method.

Only smalll differences were observed by comparing the diffractograms of the first acquisitions with the lowest dose, see Figure 5.4. Extra spots at high frequency are only observed for the interleaved acquisitions. Negligible drift was estimated, see Figure 5.20. The extra spots are presumably mainly caused by early beam damage scanning with the interleaved method, which induces small periodic contrast variations in the acquired images, see Figures 5.9 and 5.10.

5.5 Conclusions

Here we have demonstrated that beam damage in a prototype commercial zeolite sample (additionally the results were replicated in a porous Cu-compound sample) shows an interesting dependence on the applied scan strategy. At the same total dose and the same sampling of the images, a significant reduction of beam damage is observed for an alternative interleaved scanning pattern as compared to the traditional raster scanning pattern. We reach this conclusion through the application of a programmable scan engine that allows us to repeat multiple experiments under well-controlled conditions, providing a statistically relevant observation.

When doing multiple acquisitions, the damage is lower if more frames are recorded for the same total time and same total dose. The largest gain in damage reduction was obtained from the combination of the interleaved scanning with fast multiple acquisitions. This links to dose fractionation experiments that were reported [82] and again requires a notion of a damage mechanism that spreads in time. It has to be noted however that in our

experiments the dose rate per pixel was always kept constant so the effects of these method are essentially different from the effects of dose fractionation, as well as from the dose rate effects highlighted in chapter 3.

These observations will serve as a basis to build an empirical model that contains all ingredients to simulate all aspects of the experiments presented here. Such model could then allow us to make predictions on how to further lower beam damage without necessarily lowering the electron dose. Our observations support the (often vague) notion in the community that electron dose and acceleration voltage are not the only parameters affecting beam damage in (S)TEM experiments and rethinking the pattern in which this dose is applied holds promise to further shift the possibilities of EM for beam sensitive samples.

Chapter 6

Diffusion model for the observed beam damage behaviour

In the previous chapter, it was shown that beam damage in certain classes of materials is reduced when changing the electron beam scan pattern. In particular, the interleaved scan, where the probe skips over two pixels, was shown to outperform the conventional raster scan. Furthermore, a damage reduction was observed when fractionating the dose in multiple acquisitions. A model based on diffusion is chosen since we observed time dependent characteristic of beam damage.

In this section an empirical model is proposed to replicate the experimental observations shown in the previous chapter regarding the role of the interleaved scan pattern on the beam damage in a specific zeolite sample, LTA zeolite. Without trying to describe the specific physical process damaging this sample, we make use of a 2D diffusion model that describes the dissipation of the deposited beam energy in the sequence of probe positions that are visited during the scan pattern. The model only provides qualitative comparison with respect to the experiments; however, it gives us a tool to further optimize the scan pattern and scanning conditions to try to outrun beam damage.

The simulation code was implemented by D. Jannis, the experimental findings regarding beam damage, shown in this work, served as inputs for its implementation. The code is available on Zenodo as an effort to stimulate further research on this topic [116]. The results given here validate the model; further discussions of the model and a more detailed comparison of the simulations with respect to the experimental results will be given in a future work by D. Jannis.

6.1 Definition of the model

A two dimensional (2D) model is used to investigate the influence of the scanning pattern. A diffusion phenomenon in the third dimension parallel to the incoming electrons is neglected. Although a diffusion in this dimension would be important to consider as its diffusion path would be shorter in thin TEM samples, STEM images are 2D projections

of the real objects and non-direct spatial information is provided in the third dimension. An isotropic 2D diffusion is assumed based on the circular symmetry of the holes created with the static probe, shown in Figure 5.14, chapter 5. The incoming electron beam will locally deposit energy in the sample via inelastic interaction which can create e.g. local electrostatic charging, rise in temperature, concentration of ionised species, etc. Any of these interactions will change the state of the sample. This altered state can be designated by a parameter z and is assumed to diffuse (e.g. charge spreads out, heat diffuses, ionised species diffuse, etc.). We model the evolution of this parameter where the electron beam hits the sample as a continuous source which stays stationary during the dwell time at each position of the probe.

We can start from a general 2D Fick's diffusion model of an instantaneous point source of finite quantity Q, released at a position $\bar{r_0}$ at t = 0, whose analytical diffusion behaviour can be described by the following profile spreading with time and space as [117]:

$$z(\bar{r}, t) = \frac{Q}{4\pi D t} \exp(-\frac{|\bar{r} - \bar{r_0}|^2}{4Dt}) \tag{6.1}$$

where D is the isotropic diffusion constant.

We can extend the model to a continuous source, as is the case of the electron probe in STEM experiments. For a constant rate I that represents the electron beam current irradiating from t = 0 to t = t_d, with t_d the dwell time, the diffusion profile is given by [117]:

$$z(\bar{r}, t) = \frac{I}{4\pi D} \int_0^{\min(t,t_d)} \exp(-\frac{\boldsymbol{r}^2}{4D(t-t')}) \frac{dt'}{t-t'} \tag{6.2}$$

where $\boldsymbol{r} = \bar{r} - \bar{r_0}$, and $\bar{r_0}$ the position of the electron probe.

The integral can be separated into the two time regimes, one where the diffusion profile is calculated before the end of the irradiation and the other one after the irradiation.

The solution of this integral is given by [118]:

$$z(\bar{r}, t) = \begin{cases} 0 & : t'' \leq 0 \\ -\frac{I}{4\pi D} Ei(-\frac{\boldsymbol{r}^2}{4Dt''}) & : 0 < t'' \leq t_d \\ \frac{I}{4\pi D} \left(Ei(-\frac{\boldsymbol{r}^2}{4D(t''-t_d)}) - Ei(-\frac{\boldsymbol{r}^2}{4Dt''}) \right) & : t'' > t_d \end{cases} \tag{6.3}$$

where $t'' = t - t_0$, t_0 the time when the electron probe arrives at the point r_0, and Ei the integral exponential function.

We scale $I = 1s^{-1}$ as we are interested in a relative damage comparison between different scan conditions rather than absolute numbers. Note that z at $\bar{r_0}$ goes to +∞ which can be corrected for acknowledging that the electron probe has a finite width where $\boldsymbol{r}^2 \rightarrow \boldsymbol{r}^2 + \sigma_P^2$ with σ_P the probe diameter estimated as approximately 70 pm for atomic resolution STEM experiments.

The full diffusion profile Z can be written as the superposition of the diffusion profiles originating from every scanned point, and is given by:

$$Z(\bar{r}, t) = \sum_{i=1}^{n} z(\bar{r}, t, \boldsymbol{r_i}, t_d, t_{0,i}) \tag{6.4}$$

With $\boldsymbol{r_i}$ the scan positions visited at time $t_{0,i}$.

By only using the diffusion as mediator of damage, no total decrease in damage can be expected as the total applied dose is all that matters after all time effects have decayed. Therefore, a threshold is introduced below which no damage is induced. This type of behaviour has been observed by others [71, 119]; however, without considering a diffusion damage mechanism.

A non-linear function is added to include a threshold effect and evaluate the accumulated damage in each part of the image as a function of scan pattern details. The aim is to qualitatively model the damage observed using a minimal amount of physical parameters, diffusion constant and threshold. A simple hard-cut threshold model[1] was assumed for simplicity. Physical reasons for such a threshold could be related to dielectric breakdown, phase changes, reaction rates, or many other depending on the specific meaning of the Z parameter. We now can calculate the induced sample damage $D_a(\bar{r})$ in a certain position in the sample, by applying the threshold T_h and integrating over a time duration t_f:

$$D_a(\bar{r}, t_f) = \int_0^{t_f} \max((Z(\bar{r}, t) - T_h), 0)\, dt \tag{6.5}$$

The damage induced at every time step is assumed to be linearly proportional to the thresholded intensity. This is a first order approximation where the damage function is expected to increase monotonically with the thresholded intensity. In order to know the exact relation between intensity and damage, the entire physical process should be known which is outside the scope of this work.

According to the proposed mechanism, damage could also occur during periods of non-irradiation. Which would be in accordance with the so called ‘dark progression’ observed in x-ray radiation damage experiments [63]. However, when making STEM image acquisitions, the only damage that matters is the damage that occurred during the irradiation/recording of a given probe position. Any damage that occurs in that position after its intensity has been recorded will not change its value and t_f will be different for each scanned position.

When consecutive images are recorded, the result may be different after the first acquisition. Damage occurring before the start of a new acquisition can be considered and t_f should be taken in the limit to infinity, assuming a long time passed between the scans.

[1]This model is based on a step function used to threshold an input between two values, binary classification.

These two cases can be classified as 'damage during scan' and 'damage after scan' and their effects will be compared next in a simplified one dimensional diffusion model.

In Figure 6.1, a one dimensional model is represented where fifty points in a line are scanned with two different patterns, the first being sequentially (raster scan) and the second skipping four pixels on every pass until all points are scanned (a variation of the interleaved scan presented in the previous chapter). The simulated scanning was done at 10 s dwell time. The diffusion constant is considered as 0.5 pixels/s. The diffusion profiles for both scans at every time step and at two different instants of time are shown, before and after applying a threshold $T_h = 0.4$ (arbitrary units). The intensity of the profiles is considered proportional to the induced damage. A clear dependence of the diffusion profiles with the scan pattern is observed.

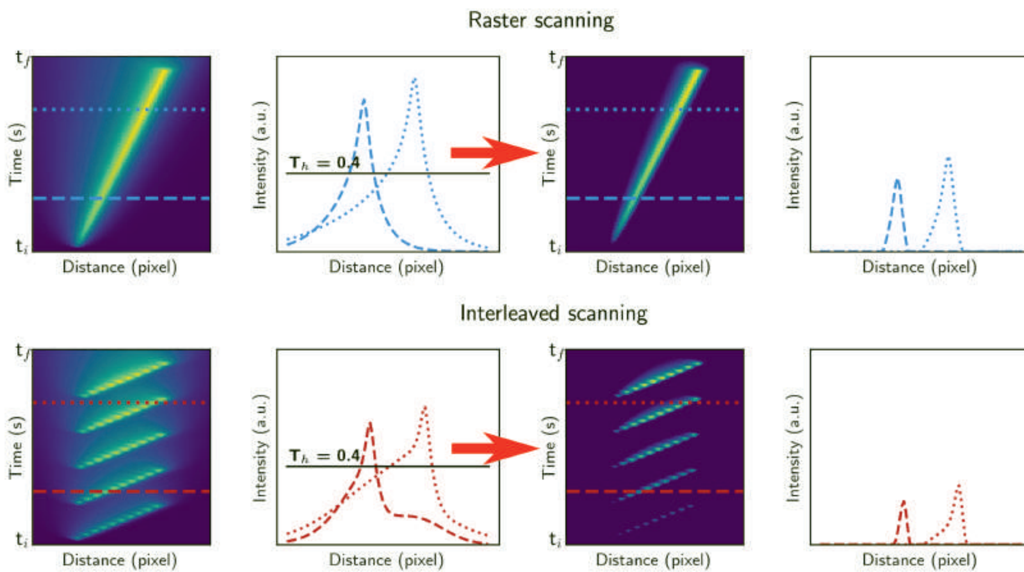

FIGURE 6.1: Simplified one dimensional diffusion model for a line scan. A diffusion constant 0.5 pixels/s and 50 scan points scanning at 10 s dwell time was considered. Upper part, results with the raster scanning. Bottom part, results with the interleaved scanning. From left to right, the diffusion profiles at different times frames and the profiles at two different instants of time (indicated by the dashed and dotted lines) before and after applying a threshold ($T_h = 0.4$) as in Equation 6.5. The shape of the profiles changes significantly after applying the threshold. The intensity of the profiles is related to the induced damage. The interleaved scan significantly reduces the simulated damage in this model.

Figure 6.2 shows the profiles considering 'damage during scan' and 'damage after scan', integrating the damage evolution at the instant of time when leaving a certain position and at the end when all scanning effects have subdued under the threshold level, respectively. In general, for both cases, the interleaved scan induces less damage than the raster scan. The damage profile between the two calculations is quite different, where the damage scanning with the raster method almost doubles when calculating the 'damage after scan', implying

that a significant amount of damage occurs in a point after it has been visited by the electron probe. This is not the case for the interleaved method, as most of the damage coming from the scan positions is dissipated during the scanning itself without much accumulation of damage.

In the rest of this chapter we only employ the 'damage during scan' calculations. Although the total damage calculated for the raster method may be underestimated in this case, we will show that this approach is able to reproduce the experimental findings.

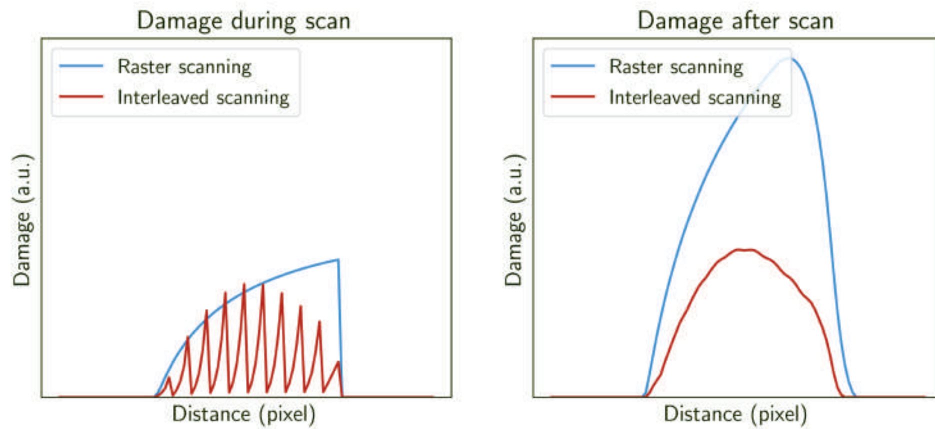

FIGURE 6.2: Damage profile of both scan patterns showing that the interleaved scan significantly reduces the simulated damage in the model from Figure 6.1. The 'damage during scan' integrates the damage evolution at the instant of time when leaving a certain position and the 'damage after scan' integrates the damage at the end when all scanning effects have subdued. For the interleaved scan the periodicity of the pattern gets imprinted on the 'damage during scan' profile. The damage profile almost doubles when calculating the 'damage after scan' for the raster scan.

Equation 6.5 is implemented numerically with a time step of $\Delta t = 1\ \mu$s and the simulations were performed for a square grid of 32×32 scan points to attain an acceptable calculation time while the results are still qualitatively comparable to the experimental damage behaviour. This approach will let us to evaluate the model and provide us a grasp of the essential parameters that play a role here.

6.2 Estimation of a diffusion constant

The results from the experiments performed on the zeolite sample, reported in the previous chapter, are used to estimate the diffusion constant and threshold for that particular sample. Those parameters can be obtained by qualitatively fitting the model to the damage profile of the following experiments:

- Hole drilling experiments, with the static probe on the sample.
- Scanning the sample three times with the raster method at 6 μs dwell time.

For a given diffusion constant, a static probe experiment can be simulated and a proper threshold can be determined to describe the damage observed when drilling holes. A multiple acquisition experiment is simulated afterwards to verify if this set of parameters (diffusion constant and threshold) is able to reproduce the experimental damage profile.

In chapter 5, a roughly estimation of the diffusion constant suggested a value in the order of units of nm^2/s. Simulations for a diffusion constant $D = 4.5\ nm^2/s$ and a threshold value of 3.33×10^{16} (in arbitrary units) have showed the best comparison with the experiments listed above.

Figure 6.3 shows three simulated damage profiles for the diffusion constant $D = 4.5\ nm^2/s$ where only the threshold is varied. The simulations are compared to the damage profile of the hole created with the static probe for an irradiation of 2 s.

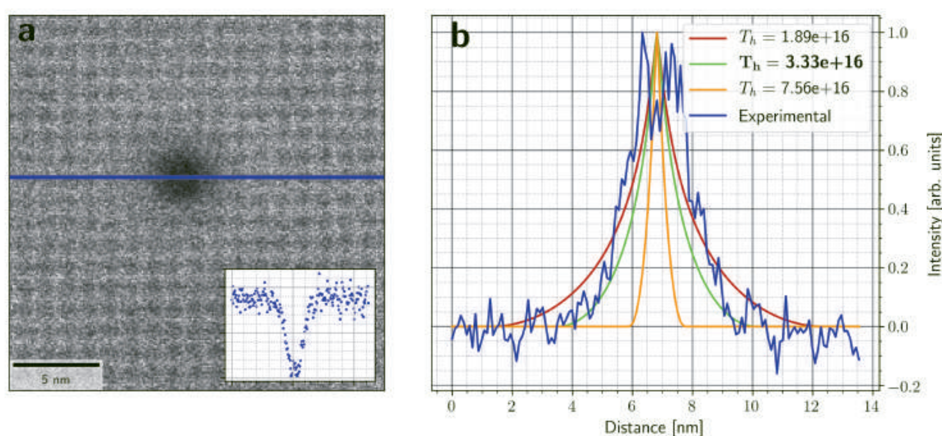

FIGURE 6.3: a. Hole created on the zeolite sample by placing a stationary beam for 2 s, cropped area of the image shown in Figure 5.14, chapter 5. b. In blue, the inverse signal shown in a, indicating the damage profile, the other colours indicate different thresholds for the simulated damage with a diffusion constant $4.5\ nm^2/s$. The simulation with threshold 3.33×10^{16} (in arbitrary units), green curve, seems to best fit the experimental damage profile.

In the previous chapter, a template matching procedure was employed to compare damage on the zeolite sample when scanning with the different methods. The sodalite cages were compared to an averaged version of these cells and the similarity with respect to this averaged version was quantified by the NCC coefficients. The coefficient values vary from -1 to 1, indicating a variation from a bad to a good similarity with respect to the template. To compare experiments and simulations, an experimental damage map is calculated from the NCC coefficients. As in the simulations high intensities are interpreted as increased damage, the value (1 – NCC) is calculated and assigned to each position of the cells and interpolated to obtain a damage experimental map, which is directly compared to the simulations.

Simulations of the raster scanning experiment scanning at 6 μs, 24.3 pm pixel size, three acquisitions, are performed, considering only a 32 × 32 scan points, and using the parameters found in the static probe simulation, shown in Figure 6.3. The results are depicted in Figure 6.4. These simulations resemble the experimental data where in the first scan almost no damage is induced. For the second scan, the damage is mostly centered. For the third scan, the damage slightly extends toward the scan direction, giving an indication that the chosen parameters for diffusion constant and threshold are qualitatively representing the experimental behaviour.

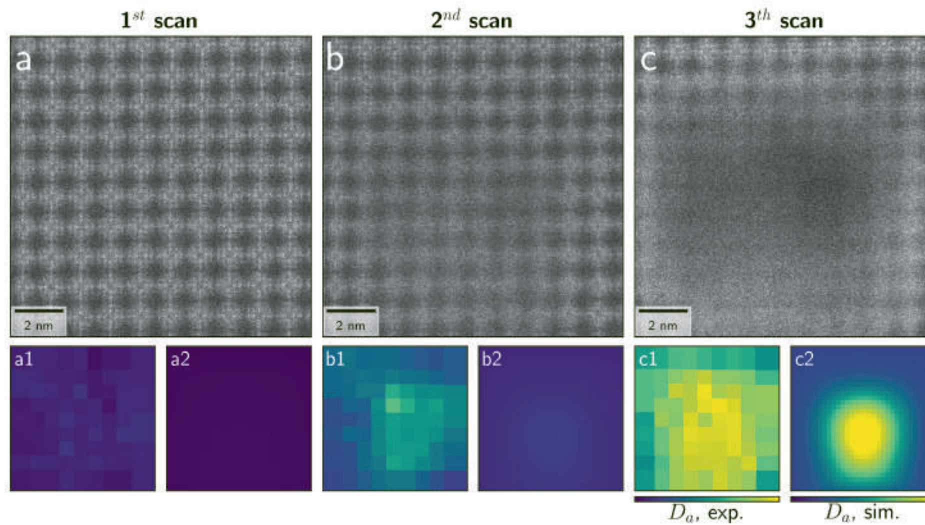

FIGURE 6.4: a, b and c correspond to the raster acquisitions of the experiment shown in Figure 5.5, chapter 5. Experimental damage maps (a1, b1 and c1) and simulated ones (a2, b2 and c2) are shown in the raw below. The experimental damage maps consist of interpolated maps with values (1 – NCC), with NCC the coefficients obtained by the template matching procedure described in the previous chapter. For both cases, higher intensities are interpreted as increased damage. Only qualitative comparison is given. The simulations resemble the experimental data where almost no damage is induced for the first scan. For the second scan, the damage is mostly centered. For the third scan, the damage slightly extends toward the y scan direction, giving an indication that the chosen parameters for diffusion constant and threshold are qualitatively representing the experimental behaviour.

Although the damage profile of the hole drilling experiment can be reproduced with other set of parameters (diffusion constant and threshold), this is not the case for the damage profile of the three acquisitions experiment scanning with the raster method. Considering diffusion constant values of 45 nm^2/s and 0.45 nm^2/s, the thresholds that better reproduce the hole drilling experiment profile were 6.67×10^{15} and 5.56×10^{16} (both in arbitrary units), respectively. For these new sets of parameters, simulations corresponding to the three acquisitions experiment were also performed. The results are shown in Figure 6.5. With a diffusion constant 45 nm^2/s, the main difference is observed in the damage

profile of the third scan where most of the damage in the simulation is mainly seen on the bottom, which is not observed in the experimental damage map. With a diffusion constant 0.45 nm^2/s, damage is more evenly distributed across the centre of the grid, which does not agree with the experimental damage map.

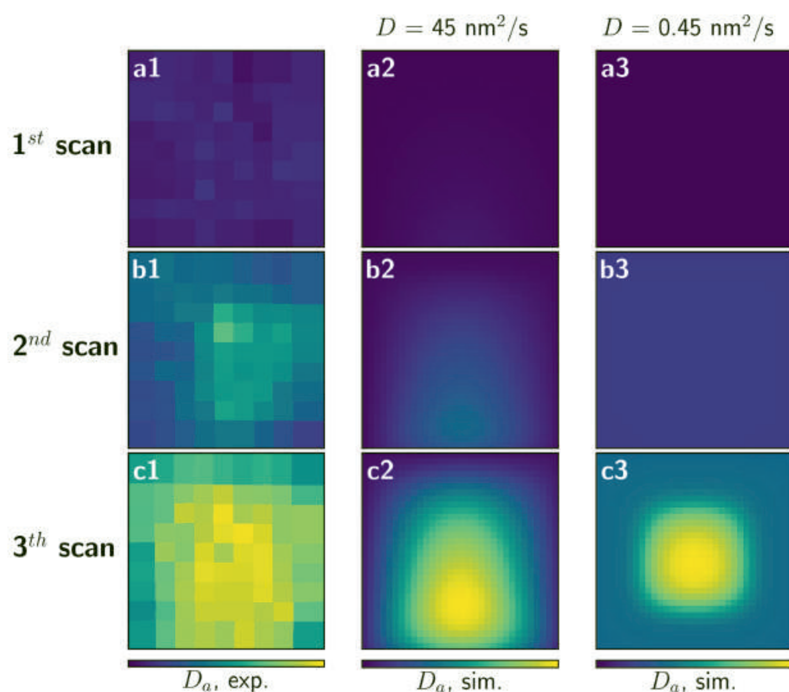

FIGURE 6.5: First column, experimental damage maps as shown in Figure 6.4, a1, b1 and c1, first, second and third scan, respectively. Second column, simulated damage maps for a diffusion constant 45 nm^2/s and a threshold 6.67×10^{15} (in arbitrary units). Most of the damage in the simulated profile is mainly seen on the bottom, which is not observed in the experiments. Third column, simulated damage maps for a diffusion constant 0.45 nm^2/s and a threshold 5.56×10^{16} (in arbitrary units). Damage in this profile is more evenly distributed across the centre of the grid, which does not agree with the experiments.

The diffusion constant estimated for this sample, 4.5 nm^2/s, can give an indication of the mechanism driving the action of damage. As indicated earlier in this work, radiolysis damage in zeolites dominates over knock-on damage. However, in certain type of these materials, both processes could be present as is the case reported by O. Ugurlu et al. [120]. Although knock-on damage can still be relevant and even induce the diffusion of atoms, it is a more localized effect that has been shown to cause structural changes at the atomic scale [121, 122]. The thermal diffusion constant of zeolites are reported to be in the order of 10^{11} nm^2/s [123], which is not comparable with the estimated value. Moreover, at the beam current used here, a rise in temperature is negligible as their thermal conductivity is in the range of 0.6 – 4 W/mK [124]. Our diffusion constant suggests a slower process. In addition, for the interleaved scanning to have some influence on damage reduction, the

time constant of this process should be at least comparable to the dwell time. For example, electron pulses with a time between pulses in the order of hundreds of fs have shown to reduce the amount of damage initiated by phonon excitations; the time between pulses longer than the life time of phonons allow to reduce the accumulation of this process and further damage [114]. Zeolites are classified as electrical insulators [125]; one possible mediator of damage is electrostatic charging, as the relaxation time calculated for insulators is in the order of magnitude of the irradiation time in STEM, and it could be reduced by the interleaved scanning.

6.3 Simulation model to reproduce experimental findings

Here the set of parameters ($D = 4.5\,\mathrm{nm}^2/\mathrm{s}$ and a threshold 3.33×10^{16}) found to reproduce the hole drilling experiment and the series acquisition with the raster method is employed to perform further simulations of the following experiments (done in the LTA zeolite):

- Scanning the sample three times with the interleaved method at 6 us dwell time.
- Scanning the sample two times with the raster and interleaved methods at 9 us dwell time.

As before, all the simulations were performed considering 24.3 pm pixel size and 32×32 scan points. The results are depicted in Figure 6.6, the first row of images correspond to the three acquisitions simulations, at 6 μs dwell time, and the second row to the two acquisitions simulations, at 9 μs dwell time. For both simulations, most of the damage is located in the central region scanning with the interleaved method, and the periodicity of the pattern is imprinted on the damage profile; resembling the alternating loss of mass shown in the line profiles of Figures 5.7 and 5.8, chapter 5.

The damage profiles are normalized with respect to the maximum intensity of the third scan of the three acquisitions simulation with the interleaved method. The maximum intensity as an indication of damage alone does not agree with the experimental findings. In both simulations, for the last acquisitions, this parameter would show more damage with the interleaved method. This effect could have its origin in the relation assumed between damage and the thresholded intensity (a non-linear dependency maybe needed to more realistically represent the effect of damage), the reduced number of scanning points compared to the experiments, etc. On the other hand, in general, beam damage in STEM imaging is not measured at the pixel scale, mainly due to the damage delocalization discussed in this thesis. In this work, beam damage was measured at the unit cell scale and as the averaged mass loss in each scanned area. For that reason, the sum of the intensities of each simulated profile was considered as a measure of damage instead of the maximum. We observed that this parameter resembles our experimental findings for all the simulations and for each of

the acquisitions. For both experiments and all the acquisitions, the interleaved scanning shows less damage. In addition, more damage is observed for the last scans of the two acquisitions simulations compared to the three acquisitions simulations.

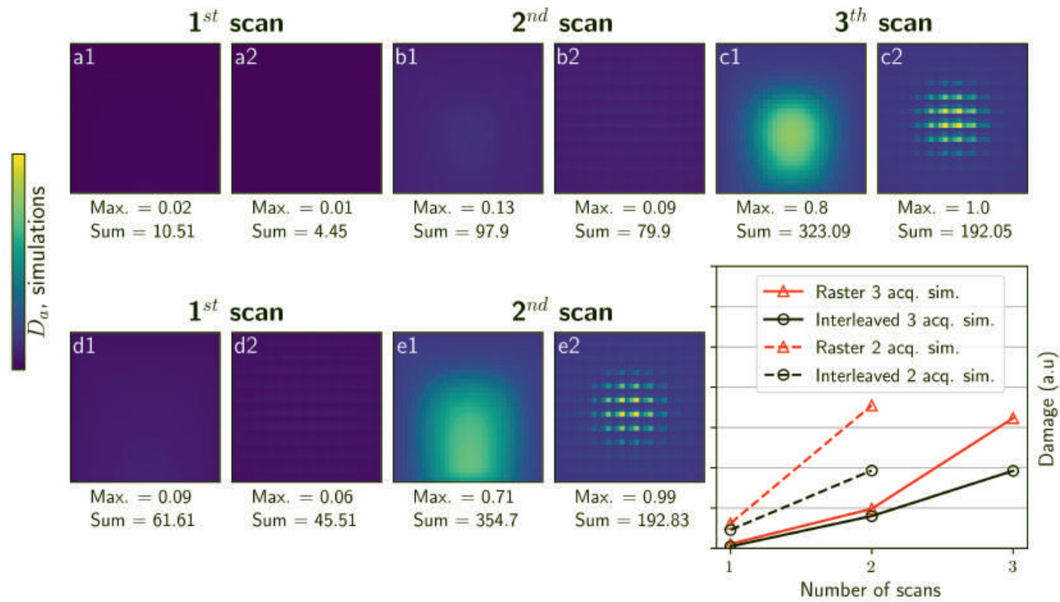

FIGURE 6.6: Simulations corresponding to the three acquisitions experiments scanning at 6 μs dwell time, top row, and two acquisitions experiments scanning at 9 μs dwell time, bottom row, with the raster (a1, b1, c1, d1 and e1) and interleaved methods (a2, b2, c2, d2, e2). The damage profiles are normalized with respect to the maximum intensity of c2. The maximum intensity as an indication of damage alone does not agree with the experimental findings. In both simulations, for the last acquisitions, this parameter would show more damage with the interleaved method. This effect could have its origin in the relation assumed between damage and the thresholded intensity (in this case a linear relation was considered, however a non-linear relation maybe be also present), the reduced number of scanning points compared to the experiments, etc. Instead, the sum of the intensities of each profile is considered as an indication of damage, similar to the quantification of damage from the experimental data. We observed that this parameter resembles our experimental findings for all the simulations and for each of the acquisitions, as shown also on the bottom right corner plot.

6.4 Estimation of parameters to further outperform beam damage

In this section, first, simulations varying the number of skipped pixels are performed to find the value that may improve the reduction of beam damage in this particular sample. Other diffusion coefficients are considered as well to elucidate the role of the scan pattern on samples with different beam damage responses.

The simulations were done scanning at 6 μs dwell time and 24.3 pm pixel size to stay close to our experiments. A grid with a scan size of 16×16 points was considered in order to have a reasonable calculation time. The threshold used in our previous calculations, 3.33×10^{16}, was applied to the simulations for different diffusions constants. The results are shown in Figure 6.7 (left). For all the diffusion constants the curves show a local minimum. For the coefficient we used in the previous simulations, 4.5 nm^2/s, the largest gain in damage reduction seems to correspond to 2 - 3 pixels skip. For the largest coefficient, 20 nm^2/s, the minimum is situated around 4 pixels skip. The gain in damage reduction increases with the diffusion constant. A higher diffusion constant allows for faster dissipation before neighbouring positions are scanned, which reduces damage accumulation. The increase in damage after a minimum is reached can be explained as follows: while the distance between consecutive positions increases when increasing the pixels to skip, the time difference between neighbouring positions is reduced which can be interpreted as less time for damage dissipation.

A second set of simulations were performed to explore the gain in damage reduction when doing multiple acquisitions while keeping the total dose constant. As shown in Figure 6.6, the diffusion model was also able to reproduce the experimental results of dose fractionation by multiple acquisitions. As before, the simulations were calculated for different diffusion constants.

We considered standard dwell times in STEM imaging, 2, 4, 8 and 16 μs. In order to keep the total dose constant, the numbers of scans were 8, 4, 2 and 1, respectively. A grid size of 16×16 scan points was considered scanning at 24.3 pm pixel size. Again, the threshold was 3.33×10^{16} and it was keep constant for all the diffusion constants. The results are shown in Figure 6.7 (right). It is shown that for every diffusion constant except for the 1.5 nm^2/s, the multiple scanning shows damage reduction compared to a single scan. In this case, the time interval to visit the same pixel with the probe during each of the acquisitions would allow for damage dissipation and hence damage reduction. Increasing the number of acquisitions, this means by scanning faster, enhances the reduction of damage. Here, the highest diffusion constant also shows the largest gain in damage reduction as a faster dissipation of damage would be expected. The effect is clearly different for the lowest diffusion constant, 1.5 nm^2/s, increasing the number of acquisitions only increase the amount of damage. This suggests that for some samples, the multiple scanning can be worse than a single scan. For a low diffusion constant, non-damage dissipation can be expected between acquisitions

and the accumulation of damage could be actually increased if multiple acquisitions are performed.

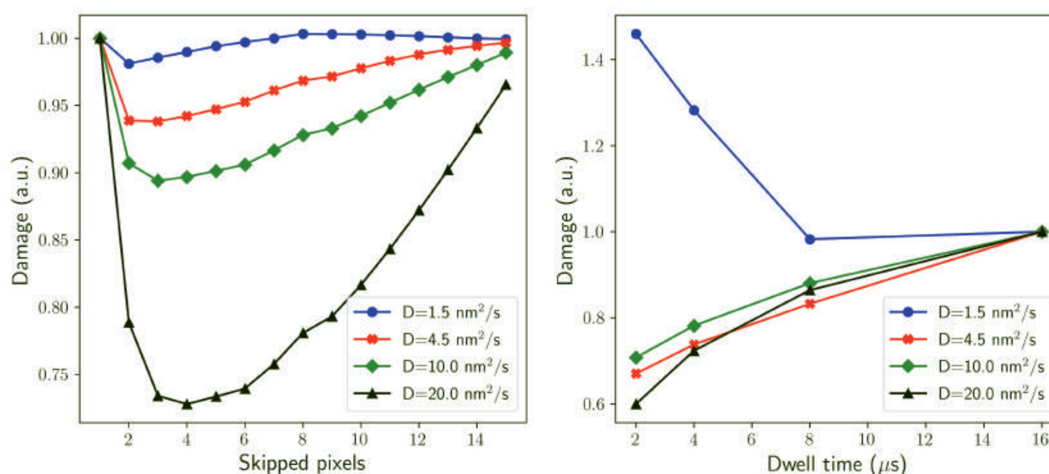

FIGURE 6.7: Damage for diffusion simulations on a grid of 16 × 16 points, scanning at 24.3 pm pixel size and considering the same threshold 3.33×10^{16} (arbitrary units) for different diffusion constants. Left, results varying the number of skipped pixels, scanning at 6 μs dwell time. A local minimum is observed when increasing the number of skipped pixels. A gain in damage reduction is reached presumably until the time interval to scan neighbouring pixels is too short to allow for damage dissipation. Right, results varying the dwell time and the number of acquisitions to maintain a constant electron dose. For dwell times 2, 4, 8 and 16 μs, the number of scans were 8, 4, 2, and 1, respectively. Increasing the number of acquisitions, by scanning at a higher speed, enhances damage reduction, except for the lowest diffusion constant 1.5 nm^2/s. Similar to the previous case, the time interval to visit the same pixel with the probe during each of the acquisitions would allow for damage dissipation. This trend is not always followed, for a slow diffusion no damage dissipation could be expected and the accumulation of damage would be actually incremented by scanning multiple times.

These results suggest that for the present sample (with parameters 4.5 nm^2/s and 3.33×10^{16}, diffusion constant and threshold, respectively) fractionating the dose in more scans would further reduce damage. While increasing the number of pixels to skip would have a contrary effect. Actually, the number of skipped pixels selected for our experiments, 2 pixels in each scan direction, seems to be an optimal value if we consider a trade-off between damage reduction and scanning distortions; at least for the range of diffusion constants evaluated here at the selected pixel size.

For the range of diffusion constants we tested here, it seems that beam damage cannot be completely avoided by the present scanning methodologies. However, the results indicate that the higher the diffusion constant, the more benefit in terms of damage reduction would be obtained. This could be the case for the porous Cu-compound sample, from which an image apparently free of damage was acquired with the interleaved scanning (see Figure 5.16 from previous chapter) compared to the raster one. Looking at the raster acquired

image, damage seems to be more severe at the bottom area, which resembles the simulated damage profile for a diffusion constant 45 nm^2/s, Figure 6.5.

Previously it was noted that, in some cases, working at cryogenic temperatures can reduce radiolysis damage effects even if heating is negligible. This is explained by a reduced mobility of the radiation-induced products that slows down the damage ratio. At this temperature condition a reduced diffusion constant would be expected as well [126], as in our model. From our previous analysis, this could either decrease the gain in damage reduction or even increase damage as suggested by the blue curves in Figure 6.7. Although at a first glance this could suggest contrasting results if applying the interleaved scanning at cryogenic temperatures, the reduced damage ratio at this condition may compensate this effect. Experiments are needed to clarify this point as previous investigations have reported a benefit of STEM over CTEM at this temperature. For example, soil bacterium and vitreous ice have shown more tolerance to the electron dose working in cryo-STEM rather than cryo-CTEM [127, 112], demonstrating that how the dose is distributed in time and space plays an important role.

Although different samples may show different thresholds, for simplicity, the same threshold value was considered here. More simulations need to be performed to elucidate the effect of this parameter on our results. A future work from D. Jannis would consider this parameter as well.

6.5 Conclusions

Here, a qualitative model to describe beam damage in STEM imaging experiments has been proposed. The model has two parameters, a diffusion constant and a threshold. From specific experiments on a commercial LTA zeolite, we were able to estimate these parameters for this material. The model was able to reproduce the damage behaviour on a series of experiments performed on this sample when changing the scan sequence and fractionating a given electron dose in multiple acquisitions. The simulations indicate that the largest gain in damage reduction is expected from the combination of the interleaved scanning with the fast multiple acquisitions.

The model is expected to describe the damage profile in other materials if the highlighted parameters can be estimated. Ideal scan parameters as dwell time and scan sequence can be estimated in order to reduce beam damage. The model agrees with evidence scattered in the literature that dose rate and dose fractionation can play a significant role in reducing beam damage, but give a more physical handle on why this would be the case.

Other scanning sequences remain to be explored with the aim to increase the gain in damage reduction. It is clear from the experimental findings and simulations that beam damage could be significantly mitigated in exchange for a minor upgrade in the scan engine of current instruments.

Chapter 7

Future perspectives and general conclusions

Although in this work we have evaluated the performance of the Hilbert and interleaved scanning in terms of image distortions and beam damage, respectively. We do believe that additional work can be done to demonstrate further applicabilities of these alternative methodologies and to elucidate some important questions.

7.1 Application of the current techniques in different beam sensitive materials

Hilbert scanning

The Hilbert scanning has shown to provide acquisitions with more isotropic scanning and drift distortions at a reduced dose compared to the raster scanning (scanning at the same pixel size, dwell time and the same number of pixels). Beam sensitive materials that can only withstand a low electron dose before deterioration of the sample occurs can benefit from this method. A large family of samples to try this method would be halide perovskites that are known for being sensitive under the electron beam [128, 129]; however Y. Yu et al. have shown atomic structural characterization combining low dose rate acquisitions and exit wave reconstruction in CTEM [130]. A cubic and an orthorhombic structure were found to coexist when non-structural damage is induced, with only a few pm difference in the lattice parameter of both structures. HAADF-STEM would be preferable as it offers a direct interpretation of the atomic columns from the image contrast. One single acquisition with the Hilbert scanning may be the only way in STEM to deliver the lowest dose that these samples can sustain before damage starts while at the same time to achieve similar precision in both scan directions to measure lattice parameters and unambiguously identify crystal structures. For similar reasons strain analysis on these materials, important for their optoelectronic properties, may benefit from this method as well. On the other hand, as the

distribution of the electron dose is different compared to line by line scanning, it may have a different influence on beam damage and needs to be investigated.

Interleaved scanning and dose fractionation methods

These methods can be applied to a large number of beam sensitive materials. For example, other commercially available zeolites can be tested to estimate the characteristic 'beam damage parameters', diffusion constant and damage threshold, using the methods described in the previous chapter. Note that these parameters are estimated by comparing the results from simple experiments (hole drilling and raster acquisitions) and diffusion simulations. These parameters can serve as inputs to perform simulations were optimal scanning conditions can be estimated specific of each sample. Knowing the ideal scanning conditions, experiments can be performed on similar non-commercial samples of interest in an attempt to optimize the design of experiments prior to microscope sessions. This approach also invites the community to share these parameters to investigate samples where electron beam damage has hindered its analysis.

Currently, scan distortions and the dynamic response of scan coils restrict the applicability of these scan patterns, for example at high speed acquisitions. These limitations can be overcome with new developments of the scan coil electronics. Moreover, a fast electostatic deflection [40, 131] can be combined. For instance, pulse modulation during dwell time irradiation can be applied or even scanning at ns dwell time.

7.2 Further experiments to determine the diffusion mechanism(s)

The damage mechanism(s) that is(are) mitigated with the interleaved scanning is an open question that remains unsolved. Identifying the exact damage mechanism in a highly beam sensitive material is a troublesome task because of the limited amount of information that can be extracted before the sample is damaged. Analytical techniques like EDX or EELS are prohibited because of the increased dose needed to achieve comparable SNR as in STEM imaging. As an effort to investigate this topic, some experiments where the damaging process is known or controlled can be performed.

7.2.1 Working at lower beam currents

The HR images acquired over the zeolite sample were obtained at standard conditions of beam current for HRSTEM imaging, i.e. 50 pA. A rise in temperature was assumed negligible. Working at low dose by reducing beam current would enforce more this assumption. A slower damage rate can still occur as in the case of the Cu-compound sample. A difference of the diffusion constant, if any, may give a grasp on the damage mechanism if for

example a different order of magnitude is obtained. To maximize the signal at low dose conditions, techniques such as Integrated Differential Phase Contrast (iDPC) or ptychography [104, 105, 132, 133, 134] can be employed and combined with the interleaved scanning. The combination of these techniques may be the route to acquire pristine images of this zeolite or from samples that exhibit more sensitivity under the electron beam such as organic molecules or bio-samples.

7.2.2 Applying the method to samples with known electrostatic charging effects

As it was mentioned in the previous chapter, the interleaved scanning can be tested at cryo-conditions to investigate any influence of the diffusion constant at this temperatures and to further explore the applicability of this technique to bio-samples, for instance. In addition, at some CTEM irradiation conditions, charging effects have been clearly identified on vitreous ice [135], showing good repeatability on the dynamic of charge build-up. Which is in the order of magnitude of standard acquisitions time in STEM imaging. This type of sample can serve as a test sample where the damage mechanism is known and where the interleaved scanning can be tested to aim for charge dissipation effects.

General conclusions

In this thesis we have proposed novel scan strategies in HRSTEM imaging with the aim to address scanning distortions, drift distortions, and electron beam damage.

The first two chapters are mainly introductory. The first chapter gives an overview of the current TEMs and the state-of-the-art technology that allow achieving atomic scale information, with a focus on the scanning operating mode. Due to imperfections on the instruments, scanning and drift distortions affect the serial acquisition in scanning mode; this topic is discussed in the second chapter.

The third chapter discusses the intriguing topic of electron beam damage, which is often aggravated at atomic resolution. The chapter also proposes a different point of view for damage effects that varies with time and space, e.g. heating effects, electrostatic charging, mobile radicals, etc., which can be examined as a diffusion process. The first results of this PhD work are given in that chapter. We provide an insight on the time and spatial dependency of beam damage by testing dose rate effects and applying compressed sensing (CS) in a beam sensitive Cu-compound sample. Although simulations comparing CS reconstructions and denoising (under the same amount of electron dose) do not show any benefit of this technique, CS reconstructions from experimental acquisitions are encouraging and show a damage reduction when the spatial distance between probe positions is larger compared to conventional scanning. The findings in this chapter were crucial to propose the alternative/interleaved scanning pattern to address beam damage.

In chapter 4 a more isotropic scanning method is proposed to overcome scanning and drift distortions. This pattern also called 'Hilbert' pattern is compared with the raster pattern in terms of image distortions. All the experimental work and data processing to evaluate this pattern are described there. Indeed, when performing strain analysis, the results show that the standard deviation is more evenly distributed along the scanning directions. A reduced standard deviation around localized features is also observed. An additional advantage of this method is the reduced dose and acquisition time compared with the raster method as only small steps are needed during the scanning and no flyback delays are applied.

In chapter 5 the interleaved pattern is tested on a commercial LTA zeolite. The experiments performed at HR show a clear damage reduction compared to the raster method at the same conditions of electron dose. A series of well controlled experiments show good repeatability in our results. The data processing and damage quantification is described in that chapter. Damage reduction was achieved only by changing the sequence of the scanning positions which support the idea of a diffusion process on the damage behaviour. Similar results were obtained in a different sample, Cu-compound.

The sixth chapter presents simulations that replicate the damage behaviour in the zeolite sample. The model is based on a diffusion constant and a threshold value that are estimated by comparing simulations and experimental profiles from simple experiments like drilling holes on the sample and raster acquisitions. We envision that this technique can be extended to other types of beam damage materials and that the proposed diffusion model can help to find optimal parameters (scanning sequence, dwell time, for instance) to further outperform beam damage.

In this thesis, the use of external hardware was essential to have full control of the scanning patterns and acquisitions. This shows a clear need for the upgrade of the microscope's scanning hardware as is the case for current electron detectors, for instance.

TEM microscopes would have a lot to gain from having a more flexible scan engine and improved scan system with combined magnetic and electrostatic deflection mechanisms. Having full access to these functionalities through a software interface is essential to make progress. It should be noted that this is also needed for 4D STEM techniques such as iDPC and ptychography where very fast scanning would be possible while a lot more information per probe position is obtaned compared to e.g. HAADF acquisitions.

List of scientific contributions

List of publications:

1. A. Velazco, A. Béché, D. Jannis, J. Verbeeck, Reducing electron beam damage through alternative STEM scanning strategies. Part I – experimental findings, submitted to Ultramicroscopy, 2021, arXiv: 2105.01617.

2. D. Jannis, A. Velazco, A. Béché, J. Verbeeck, Reducing electron beam damage through alternative STEM scanning strategies. Part II – attempt towards an empirical model describing the damage process, submitted to Ultramicroscopy, 2021, arXiv: 2104.14992.

3. A. Velazco, M. Nord, A. Béché and J. Verbeeck, Evaluation of different rectangular scan strategies for STEM imaging, Ultramicroscopy, 215 (2020) 113021, doi: 10.1016/j.ultramic.2020.113021.

4. W. Van den Broek, B. W. Reed, A. Béché, A. Velazco, et al., Various Compressed Sensing Setups Evaluated Against Shannon Sampling Under Constraint of Constant Illumination, IEEE Transactions on Computational Imaging, 5 (2019), 3, 502-514, doi: 10.1109/TCI.2019.2894950.

Conferences:

1. Virtual Early Career European Microscopy Congress (EMC).
   Oral presentation: Evaluation of different rectangular scan strategies for HRSTEM imaging. A. Velazco, M. Nord, A. Béché and J. Verbeeck. November, 2020.

2. EMAT virtual poster session, Physics department, University of Antwerp.
   Poster presentation: Evaluation of different rectangular scan strategies for HRSTEM imaging, A. Velazco, M. Nord, A. Béché and J. Verbeeck. October, 2020.

3. Lecture at the EMAT group, Physics department, University of Antwerp.
   Oral presentation: Evaluation of alternative scan strategies for high resolution STEM imaging, A. Velazco, A. Béché and J. Verbeeck. Antwerp, Belgium, February, 2020.

4. Faculty research day, faculty of science, University of Antwerp.
   Poster presentation: Temporal re-distribution of dose to reduce beam damage in (S)TEM, A. Velazco, A. Béché and J. Verbeeck. Antwerp, Belgium, January, 2020.

5. SINAPSIS 2019, IV Peruvian Scientific Meeting in Europe.
   Oral presentation: Temporal re-distribution of electron dose to reduce beam damage in STEM. A. Velazco, A. Béché and J. Verbeeck. Ghent, Belgium, September, 2019.

6. FWO meeting on Image Reconstruction.
   Poster presentation: Temporal re-distribution of dose to reduce beam damage in (S)TEM. A. Velazco, A. Béché and J. Verbeeck. Ghent, Belgium, September, 2019.

7. Royal Belgium Society for Microscopy (RBSM) meeting.
   Poster presentation: Temporal re-distribution of dose to reduce beam damage in (S)TEM. A. Velazco, A. Béché and J. Verbeeck. Louvain-la-Neuve, Belgium, September, 2019.

8. Microscopy Characterization of Organic-Inorganic Interfaces 2019 (MCOII-2019).
   Invited talk presented by Prof. Dr. Johan Verbeeck: Experimental strategies for beam damage reduction in the TEM. A. Velazco, A. Béché, D. Jannis, J. Verbeeck. Berlin, Germany, March, 2019.

9. 19th International Microscopy Congress (IMC19).
   Oral presentation: Compressed sensing and other beam strategies to reduce electron dose in (S)TEM. A. Béché, A. Velazco, D. Jannis, I. Lobato, S. Van Aert and J. Verbeeck. Sydney, Australia, September, 2018.

10. Lecture at the EMAT group, Physics department, University of Antwerp.
    Oral presentation: Compressed sensing approaches to reduce beam damage on Transmission Electron Microscopy. A. Velazco, A. Béché and J. Verbeeck. Antwerp, Belgium, April, 2018.

Bibliography

[1] E. Abbe. “A contribution to the Theory of the Microscope, and the nature of Microscopic Vision”. In: *Proceedings of the Bristal Naturalists's Society* 1 (1874), pp. 200–261.

[2] D. B. Williams and C. B. Carter. *Transmission electron microscopy: a textbook for materials science*. 2nd ed. Springer, 2008. ISBN: 978-0-387-76502-0.

[3] R. F. Egerton. *Physical principles of electron microscopy: an introduction to TEM, SEM, and AEM*. Springer, 2005. ISBN: 978-0-387-25800-3.

[4] P. W. Hawkes and J. C. H. Spence. *Science of microscopy*. Springer, 2007. ISBN: 978-0-387-25296-4.

[5] B. Fultz and J. Howe. *Transmission Electron Microscopy and Diffractometry of Materials*. Springer, 2013. ISBN: 978-3-642-29761-8. DOI: 10.1007/978-3-642-29761-8.

[6] M. De Graef. *Introduction to Conventional Transmission Electron Microscopy*. Cambridge University Press, 2003. DOI: 10.1017/CBO9780511615092.

[7] A. Muller and J. Grazul. “Optimizing the environment for sub-0.2 nm scanning transmission electron microscopy”. In: *Microscopy* 50.3 (2001), pp. 219–226. DOI: 10.1093/jmicro/50.3.219.

[8] R. Erni et al. “Atomic-Resolution Imaging with a Sub-50-pm Electron Probe”. In: *Physical Review Letters* 102.9 (2009), p. 096101. DOI: 10.1103/PhysRevLett.102.096101.

[9] H. Sawada et al. “STEM imaging of 47-pm-separated atomic columns by a spherical aberration-corrected electron microscope with a 300-kV cold field emission gun”. In: *Journal of Electron Microscopy* 58.6 (Dec. 2009), pp. 357–361. DOI: 10.1093/jmicro/dfp030.

[10] O. L. Krivanek, N. Dellby, and A. R. Lupini. “Towards sub-Å electron beams”. In: *Ultramicroscopy* 78 (1999), p. 11. DOI: 10.1016/S0304-3991(99)00013-3.

[11] O.L. Krivanek et al. “Towards sub-0.5 Å electron beams”. In: *Ultramicroscopy* 96.3-4 (2003), pp. 229–237. DOI: 10.1016/S0304-3991(03)00090-1.

[12] O. L. Krivanek et al. “Vibrational spectroscopy in the electron microscope”. In: *Nature* 514.7521 (2014), pp. 209–212. DOI: 10.1038/nature13870.

[13] S. J. Pennycook. "The impact of STEM aberration correction on materials science". In: *Ultramicroscopy* 180 (2017), pp. 22–33. DOI: 10.1016/j.ultramic.2017.03.020.

[14] E. J. Kirkland and M. G. Thomas. "A high efficiency annular dark field detector for STEM". In: *Ultramicroscopy* 62.1-2 (1996), pp. 79–88. DOI: 10.1016/0304-3991(95)00092-5.

[15] J. M. Zuo and J. C.H. Spence. *Advanced Transmission Electron Microscopy*. Springer, 2017. ISBN: 978-1-4939-6607-3. DOI: 10.1007/978-1-4939-6607-3.

[16] F. F. Krause et al. "Effects of instrument imperfections on quantitative scanning transmission electron microscopy". In: *Ultramicroscopy* 161 (2016), pp. 146–160. DOI: 10.1016/j.ultramic.2015.10.026.

[17] X. Sang and J. M. LeBeau. "Characterizing the response of a scintillator-based detector to single electrons". In: *Ultramicroscopy* 161 (2016), pp. 3–9. DOI: 10.1016/j.ultramic.2015.11.008.

[18] T. Mullarkey, C. Downing, and L. Jones. "Development of a Practicable Digital Pulse Read-Out for Dark-Field STEM". In: *Microscopy and Microanalysis* 27 (2020), pp. 99–108. DOI: 10.1017/S1431927620024721.

[19] J. P. Buban et al. "High-resolution low-dose scanning transmission electron microscopy". In: *Journal of Electron Microscopy* 59.2 (2010), pp. 103–112. DOI: 10.1093/jmicro/dfp052.

[20] A. Mittelberger, C. Kramberger, and J. C. Meyer. "Software electron counting for low-dose scanning transmission electron microscopy". In: *Ultramicroscopy* 188 (2018), pp. 1–7. DOI: 10.1016/j.ultramic.2018.02.005.

[21] R. F. Klie, C. Johnson, and Y. Zhu. "Atomic-Resolution STEM in the Aberration-Corrected JEOL JEM2200FS". In: *Microscopy and Microanalysis* 14.1 (2008), pp. 104–112. DOI: 10.1017/S1431927608080136.

[22] K. Kimoto et al. "Local crystal structure analysis with several picometer precision using scanning transmission electron microscopy". In: *Ultramicroscopy* 110.7 (2010), pp. 778–782. DOI: 10.1016/j.ultramic.2009.11.014.

[23] A. B. Yankovich et al. "High-precision scanning transmission electron microscopy at coarse pixel sampling for reduced electron dose". In: *Advanced Structural and Chemical Imaging* 1.1 (2015), p. 2. DOI: 10.1186/s40679-015-0003-9.

[24] J. H. Turner and R. O'Keefe M. A. Mueller. "Design and Implementation of a Site for a One-Ångstrom TEM". In: *Microscopy and Microanalysis* 3.S2 (1997), pp. 1177–1178. DOI: 10.1017/S1431927600012770.

[25] David A. Muller et al. "Room design for high-performance electron microscopy". In: *Ultramicroscopy* 106.11-12 (2006), pp. 1033–1040. DOI: 10.1016/j.ultramic.2006.04.017.

[26] J. K. Farrer et al. "Design and Construction of an Underground TEM Lab at Brigham Young University". In: *Microscopy and Microanalysis* 11.S2 (2005), pp. 892–893. DOI: 10.1017/S1431927605509061.

[27] J. C. H Spence. *High-resolution electron microscopy*. Oxford University Press, 2009. ISBN: 978-0-19-955275-7.

[28] H.S. von Harrach. "Instrumental factors in high-resolution FEG STEM". In: *Ultramicroscopy* 58.1 (1995), pp. 1–5. DOI: 10.1016/0304-3991(94)00172-J.

[29] J. Li et al. "The effect of scanning jitter on geometric phase analysis in STEM images". In: *Ultramicroscopy* 194 (2018), pp. 167–174. DOI: 10.1016/j.ultramic.2018.07.011.

[30] D. Cooper et al. "Strain mapping of semiconductor specimens with nm-scale resolution in a transmission electron microscope". In: *Micron* 80 (2016), pp. 145–165. DOI: 10.1016/j.micron.2015.09.001.

[31] L. Jones et al. "Optimising multi-frame ADF-STEM for high-precision atomic-resolution strain mapping". In: *Ultramicroscopy* 179 (2017), pp. 57–62. DOI: 10.1016/j.ultramic.2017.04.007.

[32] X. Sang and J. M. LeBeau. "Revolving scanning transmission electron microscopy: Correcting sample drift distortion without prior knowledge". In: *Ultramicroscopy* 138 (2014), pp. 28–35. DOI: 10.1016/j.ultramic.2013.12.004.

[33] C. Ophus, J. Ciston, and C. T. Nelson. "Correcting nonlinear drift distortion of scanning probe and scanning transmission electron microscopies from image pairs with orthogonal scan directions". In: *Ultramicroscopy* 162 (2016), pp. 1–9. DOI: 10.1016/j.ultramic.2015.12.002.

[34] L. Jones and P. D. Nellist. "Identifying and Correcting Scan Noise and Drift in the Scanning Transmission Electron Microscope". In: *Microscopy and Microanalysis* 19.4 (2013), pp. 1050–1060. DOI: 10.1017/S1431927613001402.

[35] K. W. Lee and J. T. L. Thong. "Improving the speed of scanning electron microscope deflection systems". In: *Measurement Science and Technology* 10.11 (1999), pp. 1070–1074. DOI: 10.1088/0957-0233/10/11/316.

[36] J. T. L. Thong and F. Li. "High-speed operation of scanning electron microscope lenses: High-speed operation of SEM lenses". In: *Scanning* 19.4 (1997), pp. 275–280. DOI: 10.1002/sca.4950190405.

[37] L. Kovarik et al. “Implementing an accurate and rapid sparse sampling approach for low-dose atomic resolution STEM imaging”. In: *Applied Physics Letters* 109.16 (2016), p. 164102. DOI: 10.1063/1.4965720.

[38] S. Ning et al. “Scanning distortion correction in STEM images”. In: *Ultramicroscopy* 184 (2018), pp. 274–283. DOI: 10.1016/j.ultramic.2017.09.003.

[39] L. Jones et al. “Smart Align—a new tool for robust non-rigid registration of scanning microscope data”. In: *Advanced Structural and Chemical Imaging* 1.1 (2015), p. 8. DOI: 10.1186/s40679-015-0008-4.

[40] W. C. Lenthe et al. “Advanced detector signal acquisition and electron beam scanning for high resolution SEM imaging”. In: *Ultramicroscopy* 195 (2018), pp. 93–100. DOI: 10.1016/j.ultramic.2018.08.025.

[41] I. MacLaren et al. “Detectors—The ongoing revolution in scanning transmission electron microscopy and why this important to material characterization”. In: *APL Materials* 8.11 (2020), p. 110901. DOI: 10.1063/5.0026992.

[42] J. Chung, G. Lian, and L. Rabenberg. “Practical and Reproducible Mapping of Strains in Si Devices Using Geometric Phase Analysis of Annular Dark-Field Images From Scanning Transmission Electron Microscopy”. In: *IEEE Electron Device Letters* 31.8 (2010), pp. 854–856. DOI: 10.1109/LED.2010.2049562.

[43] M. Gutiérrez et al. “Analysis by HR-STEM of the Strain Generation in InP after SiNx Deposition and ICP Etching”. In: *Journal of Electronic Materials* 49.9 (2020), pp. 5226–5231. DOI: 10.1007/s11664-020-08312-6.

[44] X. Sang et al. “Precision controlled atomic resolution scanning transmission electron microscopy using spiral scan pathways”. In: *Scientific Reports* 7.1 (2017), p. 43585. DOI: 10.1038/srep43585.

[45] X. Sang et al. “Dynamic scan control in STEM: spiral scans”. In: *Advanced Structural and Chemical Imaging* 2.1 (2016), p. 6. DOI: 10.1186/s40679-016-0020-3.

[46] R. F. Egerton. “Control of radiation damage in the TEM”. In: *Ultramicroscopy* 127 (2013), pp. 100–108. DOI: 10.1016/j.ultramic.2012.07.006.

[47] R. F. Egerton, P. Li, and M. Malac. “Radiation damage in the TEM and SEM”. In: *Micron* 35.6 (2004), pp. 399–409. DOI: 10.1016/j.micron.2004.02.003.

[48] R. F. Egerton et al. “Basic questions related to electron-induced sputtering in the TEM”. In: *Ultramicroscopy* 110.8 (2010), pp. 991–997. DOI: 10.1016/j.ultramic.2009.11.003.

[49] J. C. Meyer et al. “Accurate Measurement of Electron Beam Induced Displacement Cross Sections for Single-Layer Graphene”. In: *Physical Review Letters* 108.19 (2012), p. 196102. DOI: 10.1103/PhysRevLett.108.196102.

[50] G. Algara-Siller et al. “The pristine atomic structure of MoS_2 monolayer protected from electron radiation damage by graphene”. In: *Applied Physics Letters* 103.20 (2013), p. 203107. DOI: 10.1063/1.4830036.

[51] H. Chen et al. “Effect of electron beam irradiation in TEM on the microstructure and composition of nanoprecipitates in Al-Mg-Si alloys”. In: *Micron* 116 (2019), pp. 116–123. DOI: 10.1016/j.micron.2018.10.003.

[52] L.W. Hobbs. “Radiation damage in electron microscopy of inorganic solids”. In: *Ultramicroscopy* 3 (1978), pp. 381–386. DOI: 10.1016/S0304-3991(78)80058-8.

[53] R. F. Egerton. “Understanding Radiation Damage in Beam-Sensitive TEM Specimens”. In: *Microscopy and Microanalysis* 26.S2 (2020), pp. 84–86. DOI: 10.1017/S143192762001333

[54] B. Wu and A. R. Neureuther. “Energy deposition and transfer in electron-beam lithography”. In: *Journal of Vacuum Science & Technology B: Microelectronics and Nanometer Structures* 19.6 (2001), p. 2508. DOI: 10.1116/1.1421548.

[55] R. F. Egerton. “Radiation damage to organic and inorganic specimens in the TEM”. In: *Micron* 119 (2019), pp. 72–87. DOI: 10.1016/j.micron.2019.01.005.

[56] N. Jiang et al. “Nanoscale modification of optical properties in Ge-doped SiO2 glass by electron-beam irradiation”. In: *Applied Physics Letters* 80.11 (2002), pp. 2005–2007. DOI: 10.1063/1.1454211.

[57] N. Jiang. “On the spatial resolution limit of direct-write electron beam lithography”. In: *Microelectronic Engineering* 168 (2017), pp. 41–44. DOI: 10.1016/j.mee.2016.10.016.

[58] M. I. Lutwyche. “The resolution of electron beam lithography”. In: *Microelectronic Engineering* 17.1-4 (1992), pp. 17–20. DOI: 10.1016/0167-9317(92)90006-D.

[59] R. F. Egerton, S. Lazar, and M. Libera. “Delocalized radiation damage in polymers”. In: *Micron* 43.1 (2012), pp. 2–7. DOI: 10.1016/j.micron.2011.05.007.

[60] Á. Lakatos and F. Kalmár. “Investigation of thickness and density dependence of thermal conductivity of expanded polystyrene insulation materials”. In: *Materials and Structures* 46.7 (2013), pp. 1101–1105. DOI: 10.1617/s11527-012-9956-5.

[61] Z. Wang et al. “Measurement and Evaluation of Local Surface Temperature Induced by Irradiation of Nanoscaled or Microscaled Electron Beams”. In: *Nanoscale Research Letters* 14.1 (2019), p. 31. DOI: 10.1186/s11671-018-2821-x.

[62] E. Tyukalova and M. Duchamp. “Atomic resolution enabled STEM imaging of nanocrystals at cryogenic temperature”. In: *Journal of Physics: Materials* 3.3 (2020), p. 034006. DOI: 10.1088/2515-7639/ab8a95.

[63] M. Warkentin et al. "Global radiation damage: temperature dependence, time dependence and how to outrun it". In: *Journal of Synchrotron Radiation* 20.1 (2013), pp. 7–13. DOI: 10.1107/S0909049512048303.

[64] J. Cazaux. "Some considerations on the electric field induced in insulators by electron bombardment". In: *Journal of Applied Physics* 59.5 (1986), pp. 1418–1430. DOI: 10.1063/1.336493.

[65] N. Jiang. "Damage mechanisms in electron microscopy of insulating materials". In: *Journal of Physics D: Applied Physics* 46.30 (2013), p. 305502. DOI: 10.1088/0022-3727/46/30/305502.

[66] K. A. Mkhoyan et al. "Full Recovery of Electron Damage in Glass at Ambient Temperatures". In: *Physical Review Letters* 96.20 (2006), p. 205506. DOI: 10.1103/PhysRevLett.96.205506.

[67] N. Jiang and J. C. H. Spence. "On the dose-rate threshold of beam damage in TEM". In: *Ultramicroscopy* 113 (2012), pp. 77–82. DOI: 10.1016/j.ultramic.2011.11.016.

[68] T. Ohno, M. Sengoku, and T. Arii. "Measurements of electron beam damage for organic crystals in a high voltage electron microscope with image plates". In: *Micron* 33.4 (2002), pp. 403–406. DOI: 10.1016/S0968-4328(01)00023-3.

[69] Z. J. W. A. Leijten et al. "Quantitative Analysis of Electron Beam Damage in Organic Thin Films". In: *The Journal of Physical Chemistry C* 121.19 (2017), pp. 10552–10561. DOI: 10.1021/acs.jpcc.7b01749.

[70] M. G. Dobb and R. Murray. "Towards higher resolution in electron beam sensitive specimens of biological origin". In: *Journal of Microscopy* 101.3 (1974), pp. 299–309. DOI: 10.1111/j.1365-2818.1974.tb03955.x.

[71] A. C. Johnston-Peck et al. "Dose-rate-dependent damage of cerium dioxide in the scanning transmission electron microscope". In: *Ultramicroscopy* 170 (2016), pp. 1–9. DOI: 10.1016/j.ultramic.2016.07.002.

[72] D. L. Donoho. "Compressed sensing". In: *IEEE Transactions on Information Theory* 52.4 (2006), pp. 1289–1306. DOI: 10.1109/TIT.2006.871582.

[73] E. J. Candes, J. Romberg, and T. Tao. "Robust uncertainty principles: exact signal reconstruction from highly incomplete frequency information". In: *IEEE Transactions on Information Theory* 52.2 (2006), pp. 489–509. DOI: 10.1109/TIT.2005.862083.

[74] Y. Luo and S. B Andersson. "A comparison of reconstruction methods for undersampled atomic force microscopy images". In: *Nanotechnology* 26.50 (2015), p. 505703. DOI: 10.1088/0957-4484/26/50/505703.

[75] J. M. Ede and R. Beanland. "Partial Scanning Transmission Electron Microscopy with Deep Learning". In: *Scientific Reports* 10.1 (2020), p. 8332. DOI: 10.1038/s41598-020-65261-0.

[76] A. Béché et al. "Development of a fast electromagnetic beam blanker for compressed sensing in scanning transmission electron microscopy". In: *Applied Physics Letters* 108.9 (2016), p. 093103. DOI: 10.1063/1.4943086.

[77] X. Li et al. "Compressed Sensing of Scanning Transmission Electron Microscopy (STEM) With Nonrectangular Scans". In: *Microscopy and Microanalysis* 24.6 (2018), pp. 623–633. DOI: 10.1017/S143192761801543X.

[78] W. Van den Broek et al. "Various Compressed Sensing Setups Evaluated Against Shannon Sampling Under Constraint of Constant Illumination". In: *IEEE Transactions on Computational Imaging* 5.3 (2019), pp. 502–514. DOI: 10.1109/TCI.2019.2894950.

[79] T. Sanders and C. Dwyer. "Inpainting Versus Denoising for Dose Reduction in Scanning-Beam Microscopies". In: *IEEE Transactions on Image Processing* 29 (2020), pp. 351–359. DOI: 10.1109/TIP.2019.2928133.

[80] H. Vanrompay et al. "Experimental Evaluation of Undersampling Schemes for Electron Tomography of Nanoparticles". In: *Particle & Particle Systems Characterization* 36.7 (2019), p. 1900096. DOI: 10.1002/ppsc.201900096.

[81] E. van den Berg and M. P. Friedlander. "Probing the Pareto Frontier for Basis Pursuit Solutions". In: *SIAM Journal on Scientific Computing* 31.2 (2009), pp. 890–912. DOI: 10.1137/080714488.

[82] L. Jones et al. "Managing dose-, damage- and data-rates in multi-frame spectrum-imaging". In: *Microscopy* 67.suppl1 (2018), pp. i98–i113. DOI: 10.1093/jmicro/dfx125.

[83] D. Hilbert. "Ueber die stetige Abbildung einer Linie auf ein Flähenstück. (On Continuous Mapping of a Line onto a Planar Surface)". In: *Mathematische Annalen* 38.suppl1 (1891), pp. 459–460. DOI: 10.1093/jmicro/dfx125.

[84] A. Zobelli et al. "Spatial and spectral dynamics in STEM hyperspectral imaging using random scan patterns". In: *Ultramicroscopy* 212 (2020), p. 112912. DOI: 10.1016/j.ultramic.2019.112912.

[85] *The scan engine was designed by M. Tencé and M. Kociak from Université Paris Sud, France. The device is currently being commercialised by Attolight. More information can be obtained on https://attolight.com.*

[86] A. Sasov. "Non-raster isotropic scanning for analytical instruments". In: *Journal of Microscopy* 165.2 (1992), pp. 289–300. DOI: 10.1111/j.1365-2818.1992.tb01487.x.

[87] P. Klapetek et al. "Gwyscan: a library to support non-equidistant scanning probe microscope measurements". In: *Measurement Science and Technology* 28.3 (2017), p. 034015. DOI: 10.1088/1361-6501/28/3/034015.

[88] M. Nord et al. "Atomap: a new software tool for the automated analysis of atomic resolution images using two-dimensional Gaussian fitting". In: *Advanced Structural and Chemical Imaging* 3.9 (2017). DOI: 10.1186/s40679-017-0042-5.

[89] V. Prabhakara et al. "Strain measurement in semiconductor FinFET devices using a novel moiré demodulation technique". In: *Semiconductor Science and Technology* 35.3 (2020), p. 034002. DOI: 10.1088/1361-6641/ab5da2.

[90] A. M. Sanchez et al. "An approach to the systematic distortion correction in aberration-corrected HAADF images". In: *Journal of Microscopy* 221.1 (2006), pp. 1–7. DOI: 10.1111/j.1365-2818.2006.01533.x.

[91] G. Bárcena-González et al. "Strain mapping accuracy improvement using super-resolution techniques". In: *Journal of Microscopy* 262.1 (2016), pp. 50–58. DOI: 10.1111/jmi.12341.

[92] L. Ma and H. Bin. "Temperature and stress analysis and simulation in fractal scanning-based laser sintering". In: *The International Journal of Advanced Manufacturing Technology* 34.9-10 (2007), pp. 898–903. DOI: 10.1007/s00170-006-0665-5.

[93] D. Nicholls et al. "Minimising damage in high resolution scanning transmission electron microscope images of nanoscale structures and processes". In: *Nanoscale* 12.41 (2020), pp. 21248–21254. DOI: 10.1039/D0NR04589F.

[94] J. T. L. Thong, K. W. Lee, and W. K. Wong. "Reduction of charging effects using vector scanning in the scanning electron microscope". In: *Scanning* 23.6 (2006), pp. 395–402. DOI: 10.1002/sca.4950230606.

[95] Lau Kien Mun et al. "The Impact of Charging on Low-Energy Electron Beam Lithography". In: *Microscopy and Microanalysis* 10.6 (2004), pp. 804–809. DOI: 10.1017/S1431927604040711.

[96] J. Rouquerol et al. *Recommendations for the Characterization of Porous Solids*. Tech. rep. De Gruyter. DOI: 10.1515/iupac.66.0925. URL: http://www.degruyter.com/view/IUPAC/iupac.66.0925.

[97] M. E. Davis. "Ordered porous materials for emerging applications". In: *Nature* 417.6891 (2002), pp. 813–821. DOI: 10.1038/nature00785.

[98] J. M. Newsam. "The Zeolite Cage Structure". In: *Science* 231.4742 (1986), pp. 1093–1099. DOI: 10.1126/science.231.4742.1093.

[99] M. M. J. Treacy and I. M. Newsam. "ELECTRON BEAM SENSITIVITY OF ZEOLITE L". In: 23.3-4 (1987), pp. 411–419. DOI: 10.1016/0304-3991(87)90252-X.

[100] I. Diaz and A. Mayoral. "TEM studies of zeolites and ordered mesoporous materials". In: *Micron* 42.5 (2011), pp. 512–527. DOI: 10.1016/j.micron.2010.12.005.

[101] V. Ortalan et al. "Direct imaging of single metal atoms and clusters in the pores of dealuminated HY zeolite". In: *Nature Nanotechnology* 5.7 (2010), pp. 506–510. DOI: 10.1038/nnano.2010.92.

[102] R. Csencsits and R. Gronsky. "Damage of zeolite Y in the TEM and its effects on TEM images". In: *Ultramicroscopy* 23.3-4 (1987), pp. 421–431. DOI: 10.1016/0304-3991(87)90253-1.

[103] L. A. Bursill, E. A. Lodge, and J. M. Thomas. "Zeolitic structures as revealed by high-resolution electron microscopy". In: *Nature* 286 (1980), pp. 111–113. DOI: 10.1038/286111a0.

[104] I. Lazić, E. G.T. Bosch, and S. Lazar. "Phase contrast STEM for thin samples: Integrated differential phase contrast". In: *Ultramicroscopy* 160 (2016), pp. 265–280. DOI: 10.1016/j.ultramic.2015.10.011.

[105] E. Yücelen, I. Lazić, and E. G. T. Bosch. "Phase contrast scanning transmission electron microscopy imaging of light and heavy atoms at the limit of contrast and resolution". In: *Scientific Reports* 8.1 (2018), p. 2676. DOI: 10.1038/s41598-018-20377-2.

[106] A. Mayoral et al. "Atomic Resolution Analysis of Silver Ion-Exchanged Zeolite A". In: *Angewandte Chemie International Edition* 50.47 (2011), pp. 11230–11233. DOI: 10.1002/anie.201105450.

[107] B. Shen et al. "Atomic Spatial and Temporal Imaging of Local Structures and Light Elements inside Zeolite Frameworks". In: *Advanced Materials* 32.4 (2020), p. 1906103. DOI: 10.1002/adma.201906103.

[108] H. Robson (Ed.) and K. P. Lillerud (Ed.) *Verified Syntheses of Zeolitic Materials*. Elsevier, 2001. ISBN: 978-0-444-50703-7.

[109] X. Qu and Q. Deng. "Damage and recovery induced by a high energy e-beam in a silicon nanofilm". In: *RSC Advances* 7.59 (2017), pp. 37032–37038. DOI: 10.1039/C7RA04997H.

[110] S. Paciornik et al. "A pattern recognition technique for the analysis of grain boundary structure by HREM". In: *Ultramicroscopy* 62.1-2 (1996), pp. 15–27. DOI: 10.1016/0304-3991(95)00084-4.

[111] R. F. Egerton. "Scattering delocalization and radiation damage in STEM-EELS". In: *Ultramicroscopy* 180 (2017), pp. 115–124. DOI: 10.1016/j.ultramic.2017.02.007.

[112] M. Ilett et al. "Cryo-analytical STEM of frozen, aqueous dispersions of nanoparticles". In: *Micron* 120 (2019), pp. 35–42. DOI: 10.1016/j.micron.2019.01.013.

[113] E. J. VandenBussche and D. J. Flannigan. "Reducing Radiation Damage in Soft Matter with Femtosecond-Timed Single-Electron Packets". In: *Nano Letters* 19.9 (2019), pp. 6687–6694. DOI: 10.1021/acs.nanolett.9b03074.

[114] C. Kisielowski et al. "Discovering Hidden Material Properties of $MgCl_2$ at Atomic Resolution with Structured Temporal Electron Illumination of Picosecond Time Resolution". In: *Advanced Functional Materials* 29.11 (2019), p. 1807818. DOI: 10.1002/adfm.201807818.

[115] W. K. Wong, J. C. H. Phang, and J. T. L. Thong. "Charging control using pulsed scanning electron microscopy". In: *Scanning* 17.5 (2006), pp. 312–315. DOI: 10.1002/sca.4950170508.

[116] J. Daen et al. *Reducing electron beam damage through alternative STEM scanning strategies. part II – attempt towards an empirical model describing the damage process.* Zenodo. DOI: 10.5281/zenodo.4707594.

[117] J. Crank. *The mathematics of diffusion*. 2d ed. Clarendon Press, 1975. ISBN: 978-0-19-853344-3.

[118] E. Antonian. *Solving the diffusion equation for a continuous point source*. URL: https://nickelnine37.github.io/the-diffusion-equation.html.

[119] N. Jiang. "Electron beam damage in oxides: a review". In: *Reports on Progress in Physics* 79.1 (2016), p. 016501. DOI: 10.1088/0034-4885/79/1/016501.

[120] O. Ugurlu et al. "Radiolysis to knock-on damage transition in zeolites under electron beam irradiation". In: *Physical Review B* 83.11 (2011), p. 113408. DOI: 10.1103/PhysRevB.83.113408.

[121] T. Susi et al. "Silicon–Carbon Bond Inversions Driven by 60-keV Electrons in Graphene". In: *Physical Review Letters* 113.11 (2011), p. 115501. DOI: 10.1103/PhysRevLett.113.115501.

[122] A. V. Krasheninnikov and F. Banhart. "Engineering of nanostructured carbon materials with electron or ion beams". In: *Nature Materials* 6.10 (2007), pp. 723–733. DOI: 10.1038/nmat1996.

[123] T. Shimonosono et al. "Thermal Properties of Zeolite-Containing Composites". In: *Materials* 11.3 (2018), p. 420. DOI: 10.3390/ma11030420.

[124] S. K. Schnell and T. J. H. Vlugt. "Thermal Conductivity in Zeolites Studied by Non-equilibrium Molecular Dynamics Simulations". In: *International Journal of Thermophysics* 34.7 (2013), pp. 1197–1213. DOI: 10.1007/s10765-013-1467-2.

[125] M. Álvaro et al. "Electrical Conductivity of Zeolite Films: Influence of Charge Balancing Cations and Crystal Structure". In: *Chemistry of Materials* 18.1 (2006), pp. 26–33. DOI: 10.1021/cm050467e.

[126] R.F Egerton and I Rauf. "Dose-rate dependence of electron-induced mass loss from organic specimens". In: *Ultramicroscopy* 80.4 (1999), pp. 247–254. DOI: 10.1016/S0304-3991(99)00114-X.

[127] S. G. Wolf, L. Houben, and M. Elbaum. "Cryo-scanning transmission electron tomography of vitrified cells". In: *Nature Methods* 11.4 (2014), pp. 423–428. DOI: 10.1038/nmeth.2842.

[128] Z. Dang et al. "*In Situ* Transmission Electron Microscopy Study of Electron Beam-Induced Transformations in Colloidal Cesium Lead Halide Perovskite Nanocrystals". In: *ACS Nano* 11.2 (2017), pp. 2124–2132. DOI: 10.1021/acsnano.6b08324.

[129] M. U. Rothmann et al. "Atomic-scale microstructure of metal halide perovskite". In: *Science* 370.6516 (2020), eabb5940. DOI: 10.1126/science.abb5940.

[130] Y. Yu et al. "Atomic Resolution Imaging of Halide Perovskites". In: *Nano Letters* 16.12 (2016), pp. 7530–7535. DOI: 10.1021/acs.nanolett.6b03331.

[131] I. G. C. Weppelman et al. "Concept and design of a beam blanker with integrated photoconductive switch for ultrafast electron microscopy". In: *Ultramicroscopy* 184 (2018), pp. 8–17. DOI: 10.1016/j.ultramic.2017.10.002.

[132] M. J. Humphry et al. "Ptychographic electron microscopy using high-angle dark-field scattering for sub-nanometre resolution imaging". In: *Nature Communications* 3.1 (2012), p. 730. DOI: 10.1038/ncomms1733. (Visited on 05/23/2021).

[133] T. J. Pennycook et al. "Efficient phase contrast imaging in STEM using a pixelated detector. Part 1: Experimental demonstration at atomic resolution". In: *Ultramicroscopy* 151 (2015), pp. 160–167. DOI: 10.1016/j.ultramic.2014.09.013.

[134] H. Yang, T. J. Pennycook, and P. D. Nellist. "Efficient phase contrast imaging in STEM using a pixelated detector. Part II: Optimisation of imaging conditions". In: *Ultramicroscopy* 151 (2015), pp. 232–239. DOI: 10.1016/j.ultramic.2014.10.013.

[135] C. J. Russo and R. Henderson. "Charge accumulation in electron cryomicroscopy". In: *Ultramicroscopy* 187 (2018), pp. 43–49. DOI: 10.1016/j.ultramic.2018.01.009.

Acknowledgements

I would like to start by expressing my gratitute to my supervisor Johan Verbeeck, who gave me the opportunity to explore the fascinating field of tranmission electron microscopy. I am very grateful for what I have learned working in his group, the critical thinking and showing your results in a professional way, for example, are skills that will serve me well in my future career. At the same time, I appreciate the freedom I had to propose and apply my own ideas.

I want to thank Armand Béché for the multiple discussions we had to clarify concepts and to refine some of my ideas, and for his support during the microscope sessions.

I would also like to thank the members of my doctoral committee and the jury, Prof. Dr. Jan Sijbers, Prof. Dr. Joris Dirckx, Dr. Colin Ophus and Dr. Wouter Van de Broek, for their valuable time and for all the comments that helped me to improve this thesis.

Thanks to all the friends I made at the EMAT group, especially Iván Lobato, Thomas Altantzis, Andrey Orekhov, Adrián Pedrazo, Vivek Prabhakara, Alexander Skorikov; this work would have not been as fun as it was without their friendship.

Huge thanks to my wife Elizabeth for her invaluable support during these years and for backing me up in the decision to live far from our home, which is not over yet! I dedicate this work to my parents, I know how happy they are for our achievements.